

1                   **Jet-Track Correlation Studies of the Quark Gluon Plasma**

2                   BY

3                   HALLIE CAUSEY TRAUGER

4                   M.Ed. University of Illinois at Chicago, 2015

5                   M.S. University of Illinois at Chicago, 2014

6                   B.A. University of Chicago, 2010

7                   THESIS

8                   Submitted in partial fulfilment of the requirements

9                   for the degree of Doctor of Philosophy in Physics

10                  in the Graduate College of the University of Illinois at Chicago, 2017

11                  Chicago, IL

12                  DEFENSE COMMITTEE:

13                  Olga Evdokimov, Chair and Advisor

14                  David Hofman

15                  Zhenyu Ye

16                  Misha Stephanov

17                  Julia Velkovska, Vanderbilt University

18

## ACKNOWLEDGEMENTS

19 Thanks go here...

20

HCT

21

## CONTRIBUTION OF AUTHORS

- 22 - Note previous publications (HIN-14-016, HIN-15-011, HIN-16-020)
- 23 - Describe CMS authorship policy
- 24 - Outline general CMS inputs (reconstruction etc.) that contributed to work
- 25 - Outline aspects that are my own work (and others' contributions to these as well, esp. Run 2)

## CONTENTS

27	<b>1 Introduction</b>	<b>1</b>
28	<b>2 The quark gluon plasma</b>	<b>2</b>
29	2.1 Predictions and early evidence for the quark gluon plasma . . . . .	2
30	2.2 Properties of the quark gluon plasma . . . . .	4
31	2.3 Characterizing collision centrality . . . . .	4
32	2.4 Collective behavior in the QGP . . . . .	4
33	<b>3 Jets as probes of the quark gluon plasma</b>	<b>5</b>
34	3.1 Measuring suppression of high- $p_T$ particles and jets . . . . .	6
35	3.2 Jet fragmentation function and jet shape measurements . . . . .	10
36	3.3 Dijet asymmetry and momentum balance studies . . . . .	12
37	<b>4 Models of jet energy loss in the quark gluon plasma</b>	<b>16</b>
38	4.1 Survey of theoretical models of jet quenching mechanisms . . . . .	16
39	4.2 Quenching model comparisons to high- $p_T$ particle and jet observables . . . . .	18
40	4.3 Theoretical motivations for detailed jet-track correlation studies . . . . .	18
41	<b>5 The Large Hadron Collider and the CMS detector</b>	<b>19</b>
42	5.1 The Large Hadron Collider . . . . .	19
43	5.2 The CMS detector . . . . .	20
44	5.3 Trackers in the CMS detector . . . . .	20
45	5.4 Calorimeters in the CMS detector . . . . .	22
46	5.5 The CMS trigger system . . . . .	23
47	<b>6 Track reconstruction and correction</b>	<b>25</b>
48	6.1 Track reconstruction in pp collisions . . . . .	25
49	6.2 Track reconstruction in PbPb collisions . . . . .	26
50	6.3 High purity tracks . . . . .	27
51	6.4 Tracking efficiency and fake rate evaluation and correction . . . . .	28
52	<b>7 Jet reconstruction and correction</b>	<b>30</b>
53	7.1 Jet reconstruction with the anti- $k_t$ algorithm . . . . .	30
54	7.2 Underlying event subtraction in PbPb data . . . . .	32
55	7.3 Jet energy corrections . . . . .	33
56	<b>8 Data and Monte Carlo samples</b>	<b>35</b>
57	8.1 Data samples and event selection . . . . .	35
58	8.2 Collision centrality determination and classes . . . . .	36
59	8.3 Monte Carlo simulation . . . . .	37
60	8.4 Jet selection and dijet asymmetry classes . . . . .	41
61	8.5 Track selection and classes . . . . .	41
62	8.6 Summary of analysis bins . . . . .	43

63	<b>9 Jet-track correlation measurements</b>	<b>44</b>
64	9.1 Analysis procedure . . . . .	44
65	9.2 Jet-track correlation pair-acceptance correction . . . . .	45
66	9.3 Separation of correlations into long range and short-range components . . . . .	45
67	9.4 Residual Jet Fragmentation Function correction . . . . .	49
68	9.5 Background fluctuation bias correction . . . . .	53
69	9.6 Evaluation of systematic uncertainties . . . . .	60
70	<b>10 Discussion of results</b>	<b>64</b>
71	10.1 Inclusive jet particle density correlation results . . . . .	64
72	10.2 Dijet correlation results . . . . .	75
73	10.3 Jet shapes . . . . .	84
74	10.4 Decomposition of hemisphere momentum balance in dijet events . . . . .	88
75	10.5 Theory implications of these results . . . . .	100
76	<b>11 Conclusion</b>	<b>101</b>
77	<b>References</b>	<b>102</b>
78	<b>Appendices</b>	<b>106</b>
79	A Jet kinematics . . . . .	106
80	B Background fitting details . . . . .	120
81	C Pair acceptance and event decomposition systematic uncertainties . . . . .	124
82	D Correlation widths and related uncertainty . . . . .	126
83	<b>Vita</b>	<b>130</b>

**LIST OF TABLES**

85      I	Summary of data samples and number of selected events . . . . .	35
86      II	Summary of Monte Carlo samples and generated events at 2.76 TeV . . . . .	39
87      III	Summary of Monte Carlo samples and generated events at 5.02 TeV . . . . .	40
88      IV	Summary of data selections and analysis bins . . . . .	43
89      V	Systematic uncertainties for particle density correlation studies at 2.76 TeV . . . . .	62
90      VI	Systematic uncertainties for particle density correlation studies at 5.02 TeV . . . . .	62
91      VII	Systematic uncertainties for balanced and unbalanced dijets in transverse momentum distribution studies at 2.76 TeV . . . . .	63
92		

## LIST OF FIGURES

94	1	QCD coupling constant $\alpha_s$ . . . . .	3
95	2	Charged particle $R_{AA}$ at 200 GeV and 2.76 TeV . . . . .	7
96	3	Charged particle $R_{AA}$ at 2.76 and 5.02 TeV . . . . .	8
97	4	Jet $R_{AA}$ at 2.76 TeV . . . . .	9
98	5	Jet fragmentation function in 2.76 TeV PbPb and pp data . . . . .	10
99	6	Jet shape measurement in 2.76 TeV PbPb and pp data . . . . .	11
100	7	Dijet asymmetry and in 2.76 TeV PbPb and pp data . . . . .	13
101	8	Hemisphere $p_T$ momentum balance in dijet events as a function of $A_J$ . . . . .	14
102	10	Model comparisons to charged particle $R_{AA}$ at 5.02 TeV . . . . .	17
103	11	CMS detector perspective drawing . . . . .	21
104	12	Diagram of CMS trackers . . . . .	22
105	13	Diagram of the HCAL . . . . .	23
106	14	Tracking efficiency correction example . . . . .	29
107	15	Closure with and without JFF-JEC for quark and gluon jets. . . . .	34
108	16	Centrality distribution for PYTHIA+HYDJET reweighted to match centrality distribution of PbPb data. . . . .	38
109	17	Vertex z distribution for PYTHIA+HYDJET reweighted to match centrality distribution of PbPb data. . . . .	38
110	18	Vertex z distribution for PYTHIA reweighted to match centrality distribution of pp data. . . . .	39
111	19	Illustration of the pair-acceptance correction procedure . . . . .	46
112	20	Illustration of the event decomposition procedure without $\Delta\phi$ fitting . . . . .	46
113	21	Illustration of the event decomposition procedure with $\Delta\phi$ fitting . . . . .	47
114	22	Jet fragmentation function bias corrections for particles with $1 < p_T^{\text{trk}} < 2$ GeV . . . . .	50
115	23	Jet fragmentation function bias corrections for particles with $2 < p_T^{\text{trk}} < 3$ GeV . . . . .	50
116	24	Jet fragmentation function bias corrections for particles with $3 < p_T^{\text{trk}} < 4$ GeV . . . . .	51
117	25	Jet fragmentation function bias corrections for particles with $4 < p_T^{\text{trk}} < 8$ GeV . . . . .	51
118	26	Integrated yield attributed to jet fragmentation function bias as a function of $p_T^{\text{trk}}$ . . . . .	52
119	27	Integrated yield attributed to jet fragmentation function bias as a function of centrality . . . . .	52
120	28	Background fluctuation bias corrections for particles with $1 < p_T^{\text{trk}} < 2$ GeV . . . . .	54
121	29	Background fluctuation bias corrections for particles with $2 < p_T^{\text{trk}} < 3$ GeV . . . . .	54
122	30	Background fluctuation bias corrections for particles with $3 < p_T^{\text{trk}} < 4$ GeV . . . . .	55
123	31	Background fluctuation bias corrections for particles with $4 < p_T^{\text{trk}} < 8$ GeV . . . . .	55
124	32	Integrated yield attributed to background fluctuation bias as a function of $p_T^{\text{trk}}$ . . . . .	56
125	33	Data-driven check of integrated yields attributed to background fluctuation bias . . . . .	57
126	34	Data-driven check of correlated $\Delta\eta$ yields attributed to background fluctuation bias . . . . .	58
127	35	Comparison of background selection bias effect for quark verus gluon jets . . . . .	59
128	36	Inclusive jet $\Delta\eta$ correlations for tracks with $1 < p_T^{\text{trk}} < 2$ GeV at 2.76 TeV . . . . .	65
129	37	Inclusive jet $\Delta\phi$ correlations for tracks with $1 < p_T^{\text{trk}} < 2$ GeV at 2.76 TeV . . . . .	66
130	38	Inclusive jet $\Delta\eta$ correlations for tracks with $2 < p_T^{\text{trk}} < 3$ GeV at 2.76 TeV . . . . .	67
131	39	Inclusive jet $\Delta\phi$ correlations for tracks with $2 < p_T^{\text{trk}} < 3$ GeV at 2.76 TeV . . . . .	68
132	40	Inclusive jet $\Delta\eta$ correlations for tracks with $3 < p_T^{\text{trk}} < 4$ GeV at 2.76 TeV . . . . .	69
133	41	Inclusive jet $\Delta\phi$ correlations for tracks with $3 < p_T^{\text{trk}} < 4$ GeV at 2.76 TeV . . . . .	70
134	42	Inclusive jet $\Delta\eta$ correlations for tracks with $4 < p_T^{\text{trk}} < 8$ GeV at 2.76 TeV . . . . .	71
135	43	Inclusive jet $\Delta\phi$ correlations for tracks with $4 < p_T^{\text{trk}} < 8$ GeV at 2.76 TeV . . . . .	72
136	44	Inclusive jet $\Delta\eta$ correlations at 5.02 TeV . . . . .	72

140	45	Inclusive jet $\Delta\phi$ correlations at 5.02 TeV . . . . .	73
141	46	Inclusive jet distribution of charged particles as a function of $\Delta r$ at 5.02 TeV . . . . .	73
142	47	Integrated inclusive jet charged particle yields at 2.76 and 5.02 TeV . . . . .	74
143	48	Dijet $\Delta\eta$ correlations for tracks with $1 < p_T^{\text{trk}} < 2$ GeV at 2.76 TeV . . . . .	76
144	49	Dijet $\Delta\phi$ correlations for tracks with $1 < p_T^{\text{trk}} < 2$ GeV at 2.76 TeV . . . . .	77
145	50	Integrated charged particle yields for inclusive, leading, and subleading jets . . . . .	78
146	51	Leading jet $\Delta\eta$ correlation widths as a function of $p_T^{\text{trk}}$ at 2.76 TeV . . . . .	80
147	52	Leading jet $\Delta\phi$ correlation widths as a function of $p_T^{\text{trk}}$ at 2.76 TeV . . . . .	81
148	53	Subleading jet $\Delta\eta$ correlation widths as a function of $p_T^{\text{trk}}$ at 2.76 TeV . . . . .	82
149	54	Subleading jet $\Delta\phi$ correlation widths as a function of $p_T^{\text{trk}}$ at 2.76 TeV . . . . .	83
150	55	Inclusive jet shape at 5.02 TeV, shown differentially in $p_T^{\text{trk}}$ . . . . .	85
151	56	Leading jet shape at 2.76 TeV, shown differentially in $p_T^{\text{trk}}$ . . . . .	86
152	57	Subleading jet shape at 2.76 TeV, shown differentially in $p_T^{\text{trk}}$ . . . . .	87
153	58	Dijet subleading-to-leading hemisphere momentum balance for balanced dijets . . . . .	90
154	59	Dijet subleading-to-leading hemisphere momentum balance for unbalanced dijets . . . . .	91
155	60	Jet peak subleading-to-leading momentum balance for balanced dijets . . . . .	92
156	61	Jet peak subleading-to-leading momentum balance for unbalanced dijets . . . . .	93
157	62	long-range subleading-to-leading momentum balance for balanced dijets . . . . .	95
158	63	long-range subleading-to-leading momentum balance for unbalanced dijets . . . . .	96
159	64	Integrated transverse momentum in the long-range $\Delta\phi$ -correlated distribution as a function of track- $p_T$ . . . . .	97
160	65	Relative contributions from jet peaks and long-range asymmetry to the double difference PbPb–pp, subleading–leading in total hemisphere transverse momentum for central collisions . . . . .	98
161	66	Relative contributions from jet peaks and long-range asymmetry to the double difference PbPb–pp, subleading–leading in total hemisphere transverse momentum for peripheral collisions . . . . .	99
162	67	Distribution of transverse momentum, pseudorapidity, and azimuthal distribution of all jet selections for Pythia data compared to PYTHIA simulation . . . . .	106
163	68	Transverse momentum distribution of all jet selections for PbPb data at 2.76 TeV compared to PYTHIA+HYDJET simulation . . . . .	107
164	69	Pseudorapidity distribution of all jet selections for PbPb data at 2.76 TeV compared to PYTHIA+HYDJET simulation . . . . .	108
165	70	Azimuthal angle distribution of all jet selections for PbPb data at 2.76 TeV compared to PYTHIA+HYDJET simulation for each collision centrality bin . . . . .	109
166	71	Distribution of pseudorapidity distribution of all jet selections for PbPb data compared to PYTHIA+HYDJET simulation for each collision centrality bin . . . . .	110
167	72	Transverse momentum distribution for PbPb data compared to PYTHIA+HYDJET simulation for each collision centrality bin . . . . .	110
168	73	Jet $\eta$ distribution for PbPb data compared to PYTHIA+HYDJET simulation for each collision centrality bin . . . . .	110
169	74	Jet $\phi$ distribution for PbPb data compared to PYTHIA+HYDJET simulation for each collision centrality bin . . . . .	111
170	75	Jet $p_T$ , $\eta$ , and $\phi$ for all pp dijets and for pp dijets with $A_J: 0 < A_J < 0.11$ . . . . .	112
171	76	Jet $p_T$ , $\eta$ , and $\phi$ for all pp dijets and for pp dijets with $A_J: 0.11 < A_J < 0.22$ . . . . .	113
172	77	Jet $p_T$ , $\eta$ , and $\phi$ for all pp dijets and for pp dijets with $A_J: 0.22 < A_J < 0.33$ . . . . .	114
173	78	Jet $p_T$ , $\eta$ , and $\phi$ for all pp dijets and for pp dijets with $A_J: A_J > 0.33$ . . . . .	115
174	79	Jet $p_T$ , $\eta$ , and $\phi$ for all PbPb dijets and for PbPb dijets with $0 < A_J < 0.11$ . . . . .	116

188	80	Jet $p_T$ , $\eta$ , and $\phi$ for all PbPb dijets and for PbPb dijets with $0.11 < A_J < 0.22$ . . .	117
189	81	Jet $p_T$ , $\eta$ , and $\phi$ for all PbPb dijets and for PbPb dijets with $0.22 < A_J < 0.33$ . . .	118
190	82	Jet $p_T$ , $\eta$ , and $\phi$ for all PbPb dijets and for PbPb dijets with $A_J > 0.33$ . . . . .	119
191	83	Dijet background fits (preliminary step) . . . . .	120
192	84	Leading jet background fits . . . . .	121
193	85	Subleading jet background fits . . . . .	122
194	86	Inclusive jet background fits . . . . .	123
195	87	Pair acceptance uncertainty determination . . . . .	124
196	88	Background subtraction uncertainty determination . . . . .	125
197	89	Width determination for PbPb leading jets . . . . .	126
198	90	Width determination for pp leading jets . . . . .	127
199	91	Width determination for PbPb subleading jets . . . . .	128
200	92	Width determination for pp subleading jets . . . . .	129

**LIST OF ABBREVIATIONS**

BNL	Brookhaven National Laboratory
CERN	Conseil Européen pour la Recherche Nucléaire
CMS	Compact Muon Solenoid
ECAL	Electromagnetic Calorimeter
$E_T$	Transverse Energy
HCAL	Hadronic Calorimeter
HF	Hadronic Forward
HLT	High Level Trigger
JEC	Jet Energy Correction
JES	Jet Energy Scale
JFF	Jet Fragmentation Function
LHC	Large Hadron Collider
MC	Monte Carlo
PbPb	Lead-lead (collision data)
PDF	Parton Distribution Function
pPb	Proton-lead (collision data)
pp	Proton-proton (collision data)
pQCD	Perturbative Quantum Chromodynamics
$p_T$	Transverse Momentum
QCD	Quantum Chromodynamics
QGP	Quark Gluon Plasma
RHIC	Relativistic Heavy Ion Collider
UE	Underlying Event

**SUMMARY**

## 1 INTRODUCTION

## 2 THE QUARK GLUON PLASMA

### 205 2.1 Predictions and early evidence for the quark gluon plasma

206 Quantum chromodynamics (QCD) describes the interactions of the quarks and gluons (together  
 207 known as partons) via the strong nuclear force. The strength of the QCD interactions, described  
 208 by the QCD coupling constant  $\alpha_s(Q)$  decreases as distances between strongly interacting partons  
 209 decreases and their exchanged momentum  $Q$ :

$$\alpha_s(Q) \propto \frac{1}{\ln(\frac{Q^2}{\Lambda_{QCD}})}, \quad (1)$$

210 where  $\Lambda_{QCD} \approx 0.2$  GeV gives the QCD scale. Figure 1 shows the dependence of  $\alpha_s$  on momentum  
 211 scale  $Q$ . In the regime where separations between partons are relatively large (small  $Q$ ),  $\alpha_s$  is large,  
 212 leading to the observed confinement of quarks and gluons in composite particles called hadrons, most  
 213 commonly baryons (comprised of 3 quarks, including protons and neutrons) and mesons (comprised  
 214 of 2 quarks). In the large  $Q$  regime, however—accessed via large baryon chemical potential  $\mu_B$  or  
 215 large temperature  $T$ —the strength of the coupling constant  $\alpha_s$  decreases, in a phenomenon known as  
 216 asymptotic freedom. Asymptotic freedom both permits the accurate approximation of high-energy  
 217 hadron interactions using perturbation theory (pQCD), and implies the deconfinement of quarks  
 218 and gluons. This phase of deconfined quarks and gluons, known as the quark gluon plasma (QGP),  
 219 was originally conceived as a gas of color-charged quarks and gluons, analogous to the plasma of  
 220 photons and electrons previously studied in quantum electrodynamics. In collider studies, this  
 221 suggests the possibility of a phase transition anticipated between the hadron gas phase present  
 222 under ordinary matter conditions, and the QGP phase present at sufficiently great  $\mu_B$  or  $T$  [1, 2].

223 In the early 1980s, relativistic nuclear collisions were suggested as a means of producing  
 224 sufficient temperatures and densities to induce a quark-gluon plasma and probe the transition  
 225 between the QGP and ordinary matter. Efforts were also made to anticipate key experimental  
 226 signatures of the short-lived possible QGP, relying in many cases on the anticipation that the QGP  
 227 would behave according to a hydrodynamic description of a system in at least partial thermal  
 228 equilibrium. Proposed signatures included enhancements of strange (heavy) quarks, unusual event  
 229 structures, greater rates of direct dilepton and photon production [4]. The first heavy ion collisions

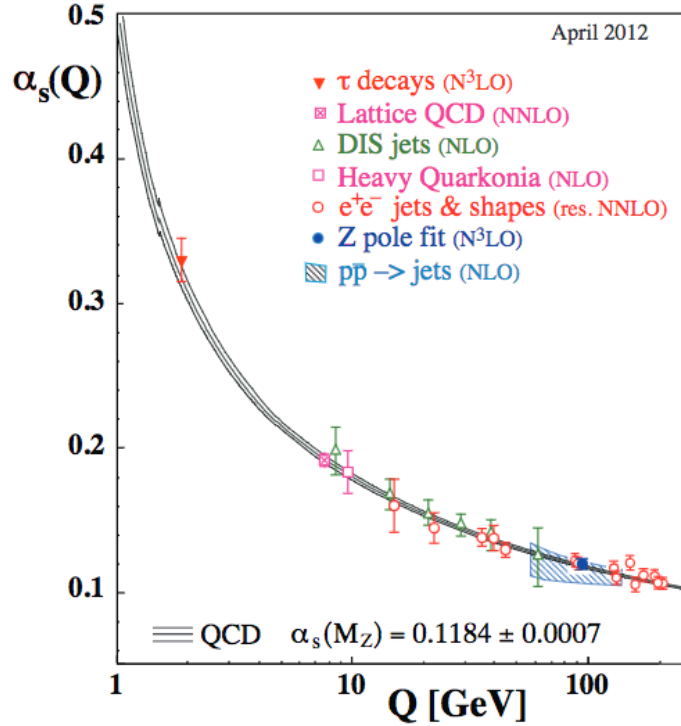


Figure 1. Momentum scale dependence of QCD coupling constant  $\alpha_s$ , from Ref. [3].

began with fixed-target experiments at the Super Proton Synchrotron (SPS) at CERN in the mid-1980s, colliding nuclei including gold and lead at energies from 40 GeV to 160 GeV through the 1990s. Analysis of the hadron yields in these collisions showed an apparent chemical equilibrium of quarks and gluons at about 170 MeV and enhancement (as anticipated) both of strangeness (via kaon/pion ratios, and  $J/\psi$  production rates). In the early 2000, a CERN press release cited these results in declaring that “a common assessment of the collected data leads us to believe that a new state of matter has indeed been created...[that] features many of the characteristics of the theoretically predicted quark-gluon plasma” [5].

Shortly after the SPS announcement, the first gold-gold collisions began at the Relativistic Heavy Ion Collider (RHIC) at Brookhaven National Laboratory, beginning an era of high-energy heavy ion collisions that would later be complimented by a parallel program at the Large Hadron Collider at CERN. Through data collection and analysis by experiments at each of these colliders over the ensuing nearly two decades, the field has gradually shifted from searches for signatures of QGP formation in heavy ion collisions, to detailed characterizations of its properties and evolution.

244 In 2005, the four experimental collaborations at RHIC (BRAHAMS, PHENIX, PHOBOS, and  
245 STAR) published coordinated white papers [6, 7, 8, 9] summarizing the assembled evidence that  
246 results from gold-gold collisions could not be explained by models of ordinary hadronic matter—  
247 most notably in signatures of collective behavior (see Sec. 2.4) and in suppression of particles with  
248 relatively high transverse momentum (see Sec. 3). Beginning in 2010, heavy ion studies at the LHC  
249 by the ALICE, ATLAS, and CMS Collaborations (and more recently by the LHCb Collaboration)  
250 have complimented the RHIC access to a wide range of center-of-mass-energies in the 7.7 GeV to  
251 200 GeV range with measurements at 2.76 TeV and 5.02 TeV.

252 **2.2 Properties of the quark gluon plasma**

- 253 – Temperature and energy density at RHIC and LHC energies  
254 – Time-evolution (initial conditions, hydrodynamic expansion of the QGP, hadronization)  
255 – QCD phase diagram characterization

256 **2.3 Characterizing collision centrality**

- 257 – Glauber model  
258 \*\*\*\*\* GLAUBER DIAGRAM \*\*\*\*\*  
259 – TAA  
260 – Glauber limitations  
261 – Experimental definitions of centrality

262 **2.4 Collective behavior in the QGP**

- 263 – Flow and interpretations (including harmonic decomp. examples)  
264 – Hydro  
265 – IS fluctuations  
266 \*\*\*\*\* DIAGRAM OF IS CONFIGURATIONS AND CONNECTION TO HARMONICS\*\*\*\*\*

### 3 JETS AS PROBES OF THE QUARK GLUON PLASMA

268 Hard scatterings in heavy ion collisions can provide powerful *insitu* probes of the quark gluon  
 269 plasma. Because of asymptotic freedom, high-energy parton-parton processes can be accurately  
 270 characterized via pQCD, and have been thoroughly studied experimentally in hadron-hadron col-  
 271 lisions. In heavy ion collisions, the initial parton-parton interaction should by causality behave  
 272 the same as a parton-parton interaction in hadron-hadron collisions. After the collision, however,  
 273 outgoing partons traverse the quark gluon plasma, providing the opportunity to study medium  
 274 properties by comparing heavy ion results to expectations inferred from hadron-hadron “vacuum”  
 275 reference data. These studies are facilitated by the “factorization theorem” in pQCD, which states  
 276 that the cross section  $\sigma_{AB \rightarrow h}^{\text{hard}}$  of hadron  $h$  produced in the hard process  $A + B \rightarrow h$ ) can be  
 277 decomposed into contributions from:

- 278 • The perturbative cross section of the parton hard scattering  $\sigma_{ab \rightarrow c}^{\text{hard}}$
- 279 • The initial parton distribution functions (PDFs) of partons in the colliding nuclei A and B  
 280 ( $f_{a/A}$  and  $f_{b/B}$  for partons of flavor  $a$  and  $b$ )
- 281 • The fragmentation function  $\mathcal{D}_{c \rightarrow h}$  describing the probability that parton  $c$  fragments into  
 282 hadron  $h$  with momentum fraction  $z = p_h/p_c$

283 The total cross section may be represented, schematically, as:

$$d\sigma_{AB \rightarrow h}^{\text{hard}} = f_{a/A}(x_a, Q^2) f_{b/B}(x_b, Q^2) \times d\sigma_{ab \rightarrow c}^{\text{hard}}(x_a, x_b, Q^2) \times \mathcal{D}_{c \rightarrow h}(z, Q^2), \quad (2)$$

284 Each contribution to  $d\sigma_{AB \rightarrow h}$  can be experimentally determined, and in hadron-hadron collisions  
 285  $\sigma_{ab \rightarrow c}^{\text{hard}}$ , fragmentation functions, and PDFs should each be universal. The partonic cross section  
 286  $\sigma_{ab \rightarrow c}^{\text{hard}}$  furthermore should not, by causality, depend on the presence or absence of the QGP. Medium  
 287 modifications may enter at two phases in this process: first, via energy loss by parton  $c$  passing  
 288 through the medium, and second via possible medium-induced changes to fragmentation func-  
 289 tions  $\mathcal{D}_{c \rightarrow h}$ . Parton energy loss is attributed to two primary mechanisms: collisional energy loss  
 290 from scatterings with partons in the medium, and medium induced radiation roughly analogous to  
 291 electromagnetic ionization in a medium [10, 11].

292 \*\*\*\* DIAGRAM OF FACTORIZATION WITH QGP MODIFICATIONS NOTED \*\*\*\*

293 This medium-induced parton energy loss implies an observable reduction of Medium prop-  
294 erties can also be further probed by comparing measurements of jet substructure in heavy ion  
295 collisions compared to pp reference data (Sec. 3.2), and by studying modifications to  $p_T$  balance in  
296 back-to-back dijet events (Sec. 3.3).

297 **3.1 Measuring suppression of high- $p_T$  particles and jets**

298 One observable to probe parton energy loss in the medium is to compare yields of both particles  
299 with relatively high transverse momentum ( $p_T$ ), and of reconstructed jets (collections of particles  
300 clustered in an effort to reconstruct the original parton energy – see Sec. 7). This reduction in jet  
301 yields compared to expectations from “vacuum” reference or scaled binary collisions can be studied  
302 as both a signature of the presence of the QGP, and an observable to distinguish between models  
303 of interactions within the QGP (see Sec. 3.1).

304 Since by pQCD factorization the partonic cross-section  $\sigma_{ab \rightarrow c}$  should be independent, in the  
305 absence of the quark gluon plasma, the nuclear inclusive cross section would be expected to scale  
306 with the number of participating nucleons, i.e.

$$d\sigma_{AB \rightarrow h}^{\text{hard}}(b) = \langle T_{AB}(b) \rangle \sigma_{pp}^{\text{hard}} \quad (3)$$

307 where  $T_{AB}(b)$  parameterizes the probability of nucleon-nucleon interactions for a given impact  
308 parameter for nuclei A and B colliding with impact parameter  $b$  as discussed in Sec. 2.3. A com-  
309 parison of actual hadron (or jet) yields compared to this expectation can therefore give information  
310 about parton interactions with the medium, as characterized by the nuclear modification factor  
311  $R_{AA}$  defined as the ratio of the observed yield in heavy ion data to the expectation from binary  
312 scaled pp data:

$$R_{AA}(p_T, \eta) = \frac{d^2\sigma_{AA}/dp_T d\eta}{\langle T_{AB}(b) \rangle d^2\sigma_{pp}/dp_T d\eta}, \quad (4)$$

313 Consistent with quenching expectations, RHIC measurements of  $R_{AA}$  in gold-gold collisions  
314 showed substantial suppression of a factor of 70-80% for  $p_T > 4$  GeV [6, 7, 8, 9]. Comparisons of  
315 RHIC measurements to early LHC results showed similar qualitative features, but greater suppres-

s<sub>16</sub> sion at low- $p_T$  at the LHC, despite the more slowly falling pp spectrum at the LHC, as shown in  
 s<sub>17</sub> Fig. 2. Measurements at the LHC have also found that  $R_{AA}$  rises with  $p_T$  for charged particles with  
 s<sub>18</sub>  $p_T > 7$  GeV, and have shown no significant center-of-mass energy differences when comparing  $R_{AA}$   
 s<sub>19</sub> at 2.76 TeV and 5.02 TeV, as shown in Fig. 3. The  $p_T$  dependence of  $R_{AA}$  is generally driven by  
 s<sub>20</sub> three factors: the kinematic constraints on jet energy loss (model-specific details will be discussed  
 s<sub>21</sub> in Sec. 4), the fact that  $R_{AA}$  takes the ratio of two steeply falling spectra the scattered partons, one  
 s<sub>22</sub> shifted by energy loss and one un-shifted, and the effects of nuclear shadowing and anti-shadowing  
 s<sub>23</sub> in the nuclear PDFs. [11, 12]

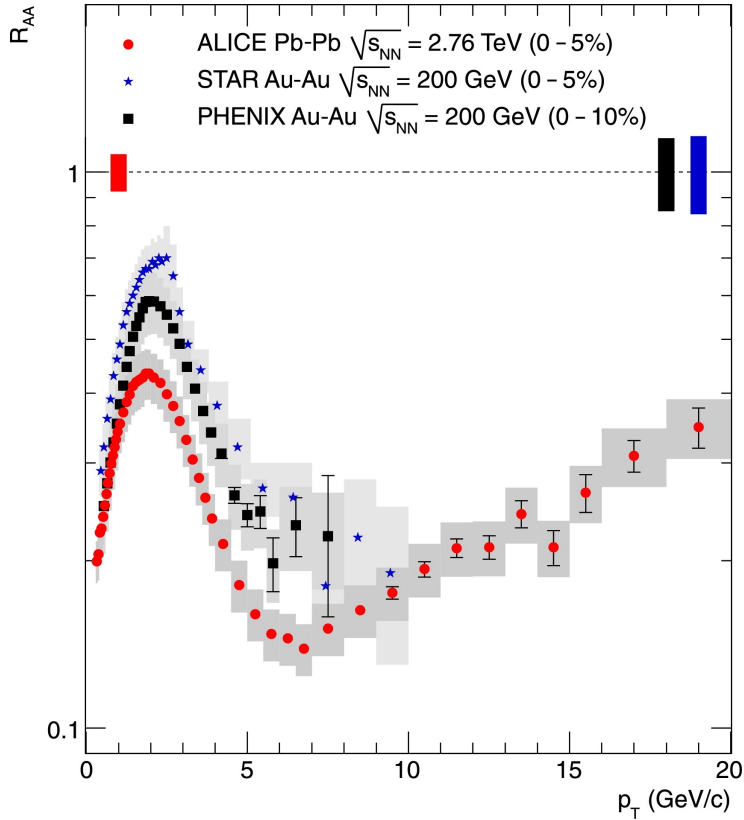


Figure 2. Measurements of charged particle  $R_{AA}$  from the STAR and PHENIX Collaborations at 200 GeV at RHIC, compared to ALICE results from the LHC at 2.76 TeV from Ref. [13].

s<sub>324</sub> Studies of high- $p_T$  tracks make use of the fact that such tracks are likely to originate from  
 s<sub>325</sub> outgoing partons in hard-scattering interactions, providing an indirect look at energy loss by the  
 s<sub>326</sub> parton used as a probe of the QGP. To more directly reconstruct parton energy, we may instead

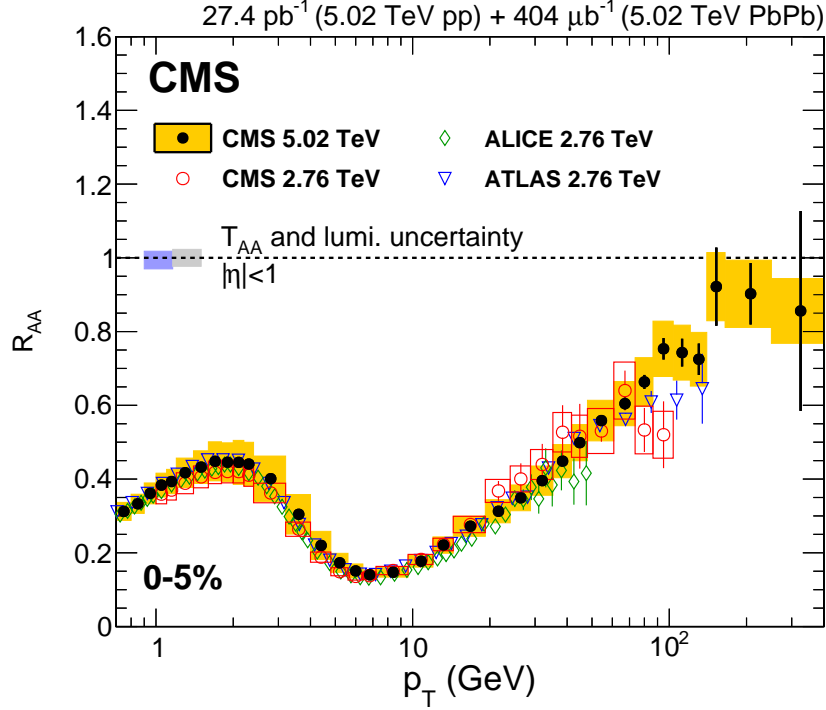


Figure 3. Measurements of charged particle  $R_{AA}$  at LHC energies 2.76 TeV and 5.02 TeV from Ref. [14].

327 consider reconstructed jets, defined as the collection of (spatially grouped) particles resulting from  
 328 the fragmentation of a high- $p_T$  quark or gluon. Jet reconstruction, described in detail in Sec. 7,  
 329 groups detector deposits to reconstruct a jet energy, and uses Monte Carlo simulation to reconstruct  
 330 a “true” jet energy of the original parton.

331 \*\*\*\*\* DIAGRAM OF WHAT IS A JET \*\*\*\*\*

332 Quenching studies with reconstructed jets therefore can offer a more direct look at energy  
 333 loss in the medium by comparing measured energy in jets in heavy ion collisions to those in proton-  
 334 proton collisions. Measurements of jet  $R_{AA}$  at the LHC reported in Refs. [15, 16] show suppression  
 335 by a factor of approximately 40-60% in most central PbPb collisions, with weak dependence on jet  
 336  $p_T$  as shown in Fig. 4.

337 Jet  $R_{AA}$  measurements capture parton energy loss by measuring the reduction in yields in  
 338 the presence of the QGP. To connect jet  $R_{AA}$  to charged particle  $R_{AA}$  measurements, it is necessary  
 339 to also consider trends in jet fragmentation patterns with jet- $p_T$ . High- $p_T$  jets are more likely to  
 340 originate from quarks than from gluons, and therefore exhibit “harder” fragmentation patterns—

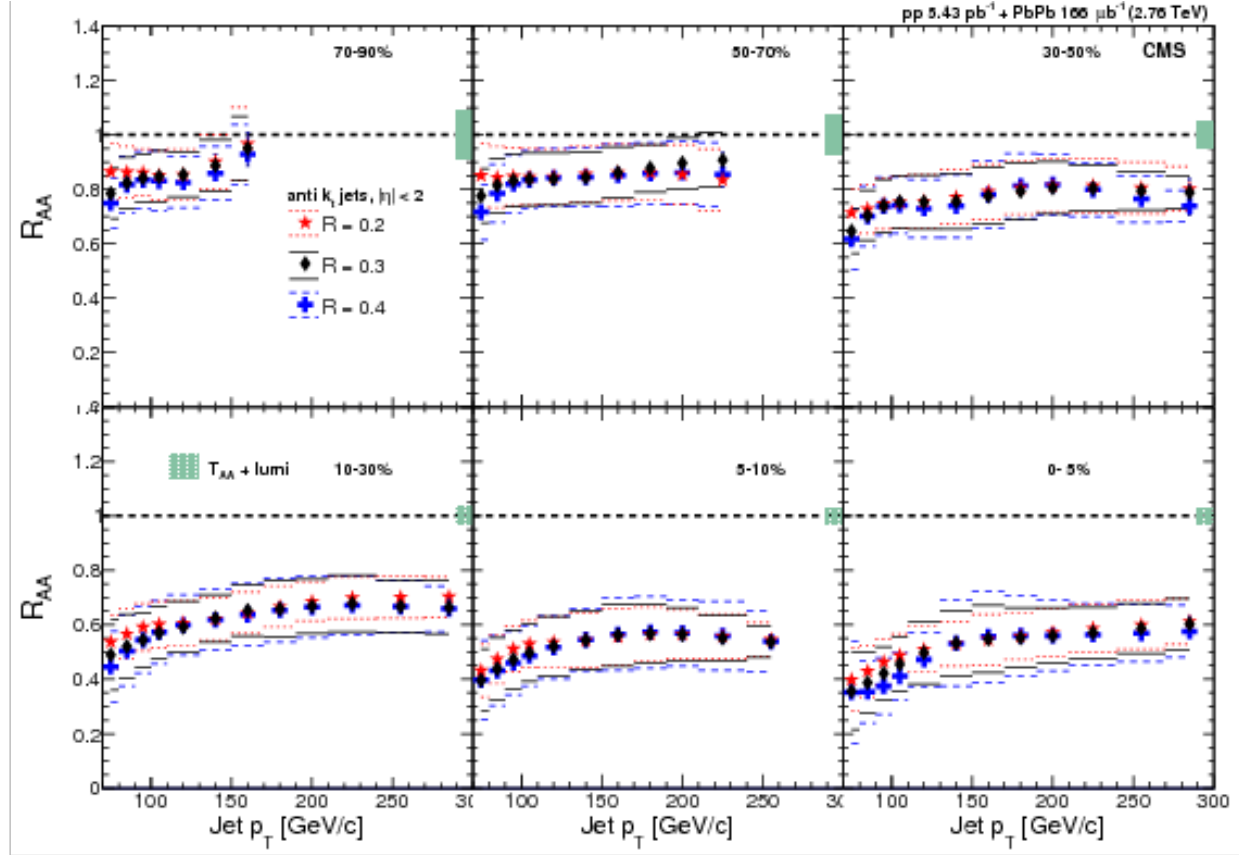


Figure 4. Jet  $R_{AA}$  at 2.76 TeV from Ref. [16].

i.e. higher- $p_T$  jets fragment into relatively fewer particles each with more  $p_T$  compared to jets at lower- $p_T$ . Jets with softer fragmentation are also expected to exhibit greater modification in the QGP, as low- $p_T$  fragmentation products rescatter in the medium. The highest- $p_T$  tracks, for which  $R_{AA}$  is the smallest, are associated with those jets that have not only the highest- $p_T$ , but also the hardest fragmentation. The high- $p_T$  sector of jet  $R_{AA}$  measurements at LHC energies, however, still includes significant contributions from jets reconstructed from softer particles that exhibit significant suppression.

### 348 3.2 Jet fragmentation function and jet shape measurements

349 Measurements of jet  $R_{AA}$  quantify the overall reduction in numbers of high- $p_T$  jets passing a certain  
 350 momentum threshold, providing an indication of the magnitude of jet energy loss in different  $p_T$   
 351 regions. As discussed above, this measurement can constrain the possible mechanisms of jet energy  
 352 loss. To further constrain models of jet energy loss, additional observables aim to capture the details  
 353 of jet fragmentation and its modification in the quark gluon plasma. One such measurement is the  
 354 jet fragmentation function, which captures the  $p_T$  distribution of tracks carrying jet momentum,  
 355 parameterized via the variables  $z$  and  $\zeta$ :

$$z = \frac{p_{||}^{\text{track}}}{p_{||}^{\text{jet}}}, \zeta = \frac{1}{\ln(z)}, \quad (5)$$

356 where  $p_{||}^{\text{track}}$  refers to the component of the track  $p_T$  along the jet axis. Jet fragmentation function  
 357 measurements from CMS shown in Fig. 5 show a centrality-dependent modification to fragmenta-  
 358 tion function in PbPb relative to pp data, with a depletion in the mid- $\zeta$  range, balanced by an  
 359 enhancement at large  $\zeta$ , in the region corresponding to low- $p_T$  tracks. This shows a redistribution  
 360 of energy within the jet cone toward softer particle production in the presence of the medium, con-  
 361 sistent with predictions of parton energy loss corresponding to a suppression of high- $p_T$  particles  
 362 (model details will be discussed in Sec. 4).

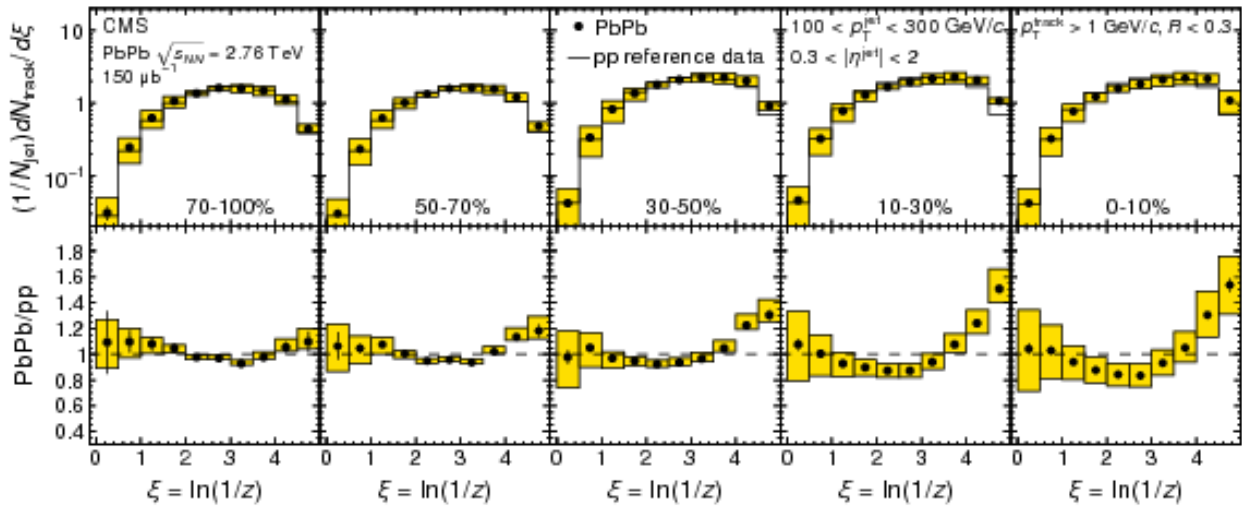


Figure 5. Jet fragmentation function for jets with  $100 < p_T < 300$  GeV in 2.76 TeV PbPb and pp data from Ref. [17].

363 In addition to characterizing the  $p_T$  spectrum of jet constituents, the distribution of  $p_T$   
 364 with respect to the jet axis can also help to constrain fragmentation scenarios. This distribution,  
 365 known as the jet shape, is defined within the jet cone as:

$$\rho(\Delta r) = \frac{1}{\delta r} \frac{1}{N_{\text{jet}}} \sum_{\text{jets}} \frac{\sum_{\text{tracks} \in [r_a, r_b]} p_T^{\text{track}}}{p_T^{\text{jet}}}, \quad (6)$$

366 where  $r_a$  and  $r_b$  correspond to the inner and outer radii, respectively, of an annulus of width  $\delta r = 0.5$   
 367 around the jet axis. The first jet shape measurement from CMS, shown in Fig. 6 (measured with  
 368 particles with  $p_T > 1$  GeV), shows a spatial redistribution of energy from small radii ( $\Delta r \approx 0.1$ )  
 369 to larger radii ( $\Delta r > 0.2$ ) from the jet axis. This is qualitatively consistent with predictions of  
 370 energy redistribution into particles that are both relatively soft ( $p_T < 3$  GeV, as observed in jet  
 371 fragmentation function measurements), and recovered at relatively large angles from the jet axis.  
 372 In this way, the study of jet shape modifications *within* the jet cone motivate extension of these  
 373 measurements to larger angles from the jet axis to quantify the distribution and  $p_T$  composition of  
 374 particles at angles larger than  $\Delta r = 0.3$ .

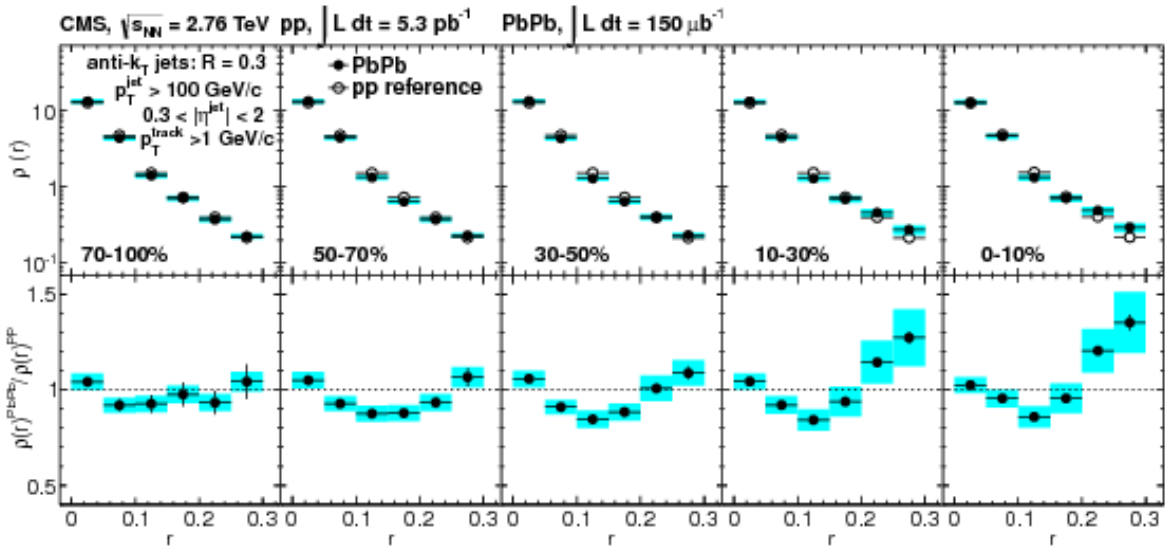


Figure 6. Jet shape measurement in 2.76 TeV PbPb and pp data from Ref. [18].

375 **3.3 Dijet asymmetry and momentum balance studies**

376 Additional possibilities for exploration of medium properties follow from the consideration of “di-  
377 jets,” jets that are back-to-back in azimuthal angle ( $\Delta\phi_{\text{jets}} \approx \pi$ ). As the incoming collision par-  
378 ticipants each begin with  $p_T \approx 0$  GeV, the total  $p_T$  of outgoing partons immediately after the  
379 collision must also be 0. If both partons experience either no energy loss (as in the vacuum)  
380 or approximately equal energy loss (i.e. by experiencing roughly equal path-lengths through the  
381 medium), the measured  $p_T$  of each jet in the dijet pair would be approximately equal. If, how-  
382 ever, the hard-scattering occurs toward the surface of the QGP, the jet with a longer path-length  
383 through the medium might be expected to experience substantially more energy loss, leading to a  
384  $p_T$  asymmetry in the dijet pair. This expectation was probed via studies of di-hadron correlations  
385 with high- $p_T$  particle triggers (4 <  $p_T$  < 6 GeV by STAR at RHIC, 8 <  $p_T$  < 15 GeV by ALICE  
386 at the LHC) showed results consistent with the expectation. These studies showed the substantial  
387 suppression (even disappearance, in the STAR studies) of yields of particles with  $p_T > 2$  GeV in  
388 the region opposite the trigger hadron in azimuth [19, 20], consistent with path-length dependent  
389 jet quenching and a surface bias in trigger particles.

390 \*\*\*\*\* DIAGRAM OF UNBALANCED DIJETS \*\*\*\*\*

391 The large kinematic reach of hard probes at the LHC allows for dijet studies at much higher  
392  $p_T$ . The first of these studies measured the “dijet imbalance” between the highest- $p_T$  (“leading  
393 jet,” with  $p_{T,1}$ ) and second-highest- $p_T$  jets (“subleading jet,” with  $p_{T,2}$  in the event, parameterized  
394 as:

$$A_J = \frac{p_{T,1} - p_{T,2}}{p_{T,1} + p_{T,2}} \quad (7)$$

395 These studies, by the ATLAS and CMS Collaborations [21, 22] showed a centrality-dependent shift  
396 in the  $A_J$  in PbPb collisions, with greater dijet asymmetry in central PbPb data than in pp or in  
397 peripheral PbPb collisions. In pp and peripheral PbPb collisions, asymmetric dijet events are those  
398 in which some  $p_T$  is carried by a third jet, and the  $A_J$  distribution is steeply falling. In central PbPb  
399 collisions, however, there are expected to be two contributions to the sample of asymmetric dijet  
400 events: not only three-jet events, but also dijet events in which the subleading jet is substantially

quenched. As shown Fig. 7, this effect is evident in the shift toward larger values of  $A_J$  in central PbPb collisions.

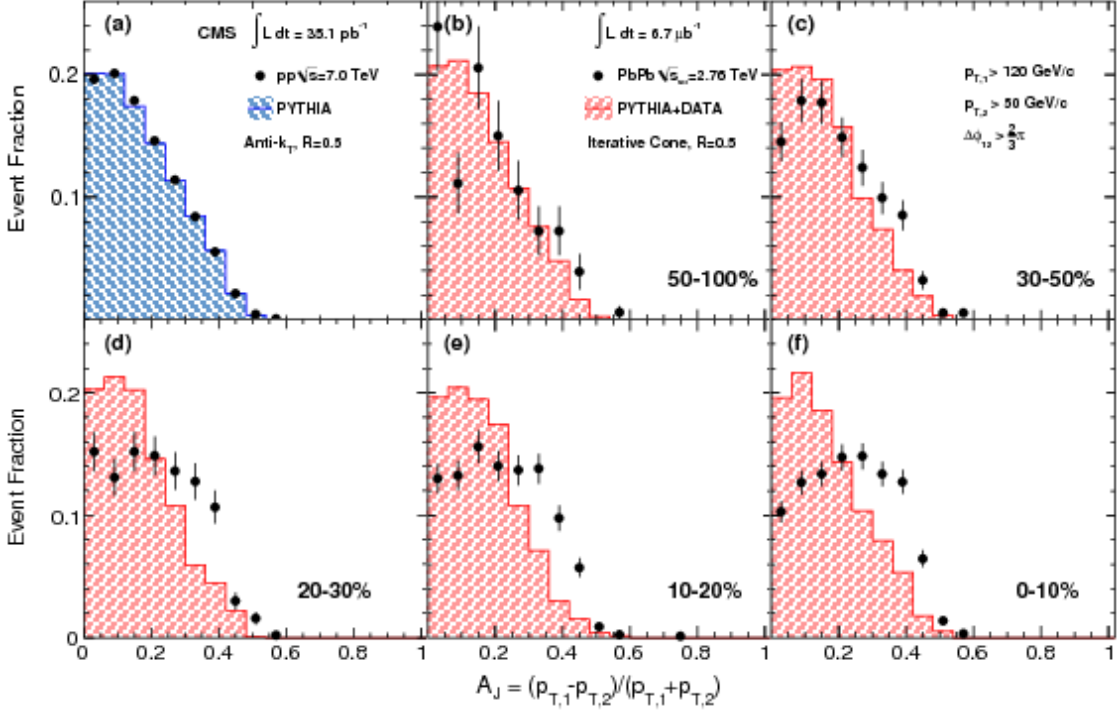


Figure 7. Dijet asymmetry in 2.76 TeV PbPb and pp data for jet selection  $p_{T,1} > 120$  GeV,  $p_{T,2} > 50$  GeV, and  $\Delta\phi_{1,2} > 2\pi/3$  from Ref. [22].

The transverse momentum difference between the leading and subleading jets may be conceptualized as “missing- $p_T$ ” from the subleading jet, which must by momentum conservation be recovered somewhere in the hemisphere of the event surrounding the subleading jet axis. One way to capture this momentum balance is by comparing the total  $p_T$  carried by tracks in different  $p_T$  classes in the subleading relative to the leading hemisphere. This balance is shown in the top row Fig. 8, for  $\vec{p}_T^{\parallel}$  defined as the projection of each track’s  $p_T$  projected in  $\phi$  onto the dijet axis (i.e. the average of the leading and subleading jet axes) ???. In pp and peripheral PbPb data, this balance shows the depletion of tracks with  $p_T > 8$  GeV in the subleading relative to the leading hemisphere balanced primarily by tracks with  $2 < p_T < 8$  GeV, consistent with the localization of these tracks in additional jets for unbalanced dijets in this scenario. The magnitude of the “missing- $p_T$ ” balancing distribution increases with growing  $A_J$  by construction. Comparing PbPb to pp distributions (differences shown in the bottom row of Fig. 8), the balancing distribution in unbalanced (large  $A_J$ )

415 events in central PbPb data shows larger contributions from soft particles with  $p_T < 2$  GeV and  
 416 smaller contributions from particles with  $p_T > 4$  GeV, indicating that the more of the balancing  
 417  $p_T$  distribution in the subleading side is carried by soft quenching products rather than additional  
 418 jets.

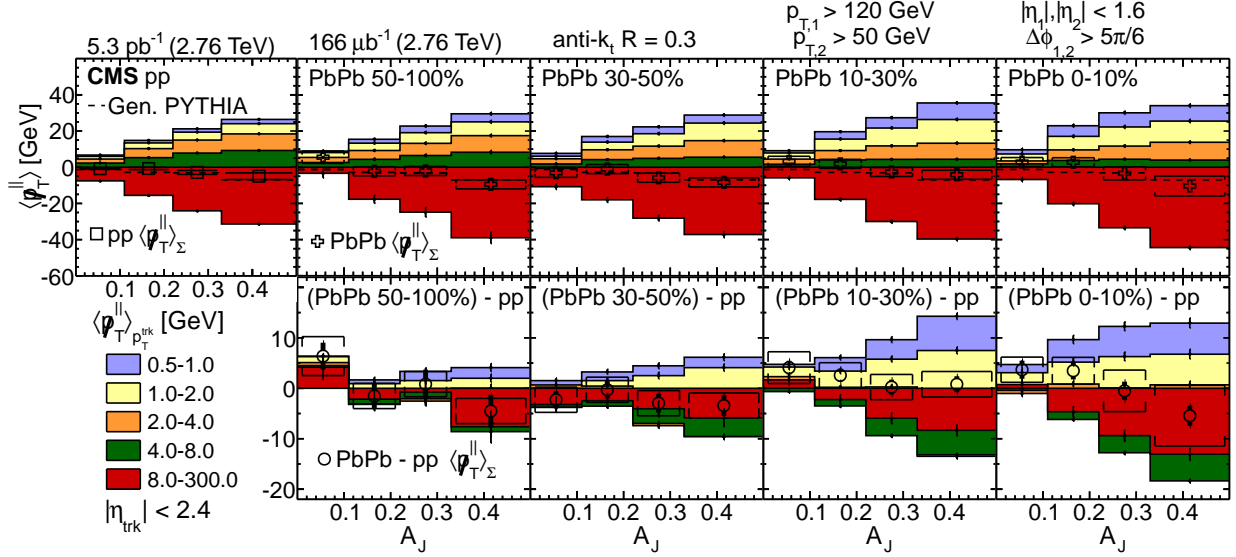


Figure 8. Top row: hemisphere  $p_T$  momentum balance in dijet events as a function of  $A_J$ , taking the total difference  $\langle p_T \rangle_{\Sigma}^{\parallel}$  in the subleading hemisphere minus that in the leading hemisphere from Ref. ?? in pp and PbPb data. Bottom row: Differences PbPb - pp.

419 Dijet momentum balance studies therefore show evidence of redistribution of jet energy  
 420 from harder to softer particles via jet quenching, and greater quenching of the subleading than  
 421 leading jets. As discussed above, the angular distribution of quenching products relative to the jet  
 422 axis is also highly relevant for constraining models of interactions between the jet and the medium.  
 423 This measurement is shown in Fig. 9 for unbalanced dijets with  $A_J > 0.22$ . Comparing the radial  
 424 distribution with respect to the dijet axis shows that in this unbalanced dijet sample in central  
 425 PbPb events, more  $p_T$  is recovered in lower- $p_T$  particles extending to large angles from the jet axis.  
 426 It is important to note that this measurement shows overall hemisphere differences in the radial  $p_T$   
 427 distribution, combining the effects of quenching to the subleading jet, quenching to the leading jet,  
 428 and also any azimuthal asymmetry in the underlying event (as would arise if the direction of the  
 429 dijet axis coupled to odd underlying event flow terms such as  $v_3$ ). Isolating and further studying  
 430 each of these contributions will be a major goal of this analysis, as discussed in Sec. 4.3.4.

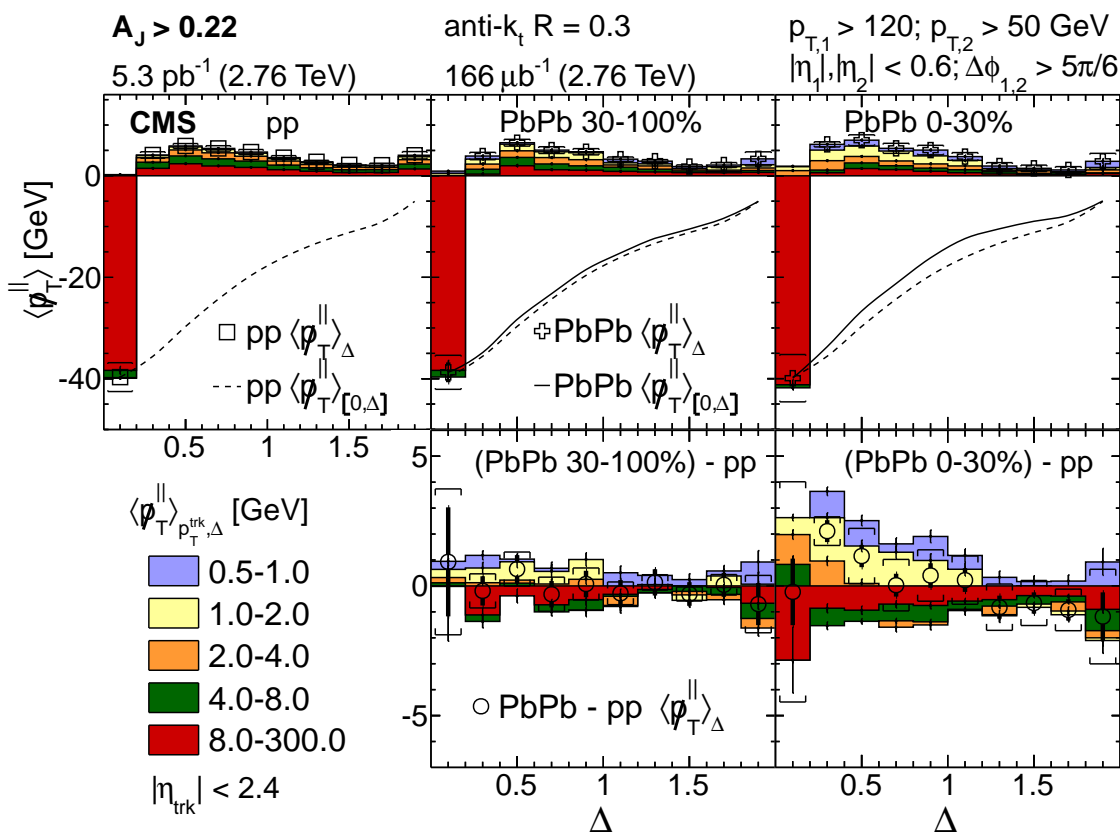


Figure 9

431        **4 MODELS OF JET ENERGY LOSS IN THE QUARK GLUON PLASMA**

432        A range of theoretical models of jet quenching have been developed to specifically account for the  
433        energy loss of a propagating probe through the quark gluon plasma. In general, models characterize  
434        collisional energy loss mechanisms (i.e. jet energy loss via elastic interactions with the medium),  
435        radiative energy loss by the propagating parton, and in some cases a medium response in the form  
436        of a “plasma wave” or back reaction. Some prominent examples of specific quenching models are  
437        surveyed briefly in Sec. 4.1. Some relevant comparisons to data are shown in Sec. 4.2, and then  
438        Sec. 4.3 summarizes goals of the present analysis in the context of the current state of jet quenching  
439        models.

440        **4.1 Survey of theoretical models of jet quenching mechanisms**

441        pQCD works down to 1 GeV...

442            • DGLV (and CUJET implementation)

443            • BDMPS-Z/ASW (and JEWEL implementation)

444            • Higher-Twist

445            • AMY (McGill and MARTINI implementations)

446            • Soft collinear effective theory with glauber gluons arxiv:1509.07257 <https://arxiv.org/pdf/1601.04695.pdf>

447            • Linear Boltzman Transport model <https://arxiv.org/pdf/1703.00822.pdf>

448            • Strong/weak hybrid model from AdS/CFT arXiv:1101.0618v2 arXiv:1609.05842

449            • Coupled jet-fluid model arXiv:1701.07951

450        Nice summary of these <https://arxiv.org/pdf/1312.5003.pdf>

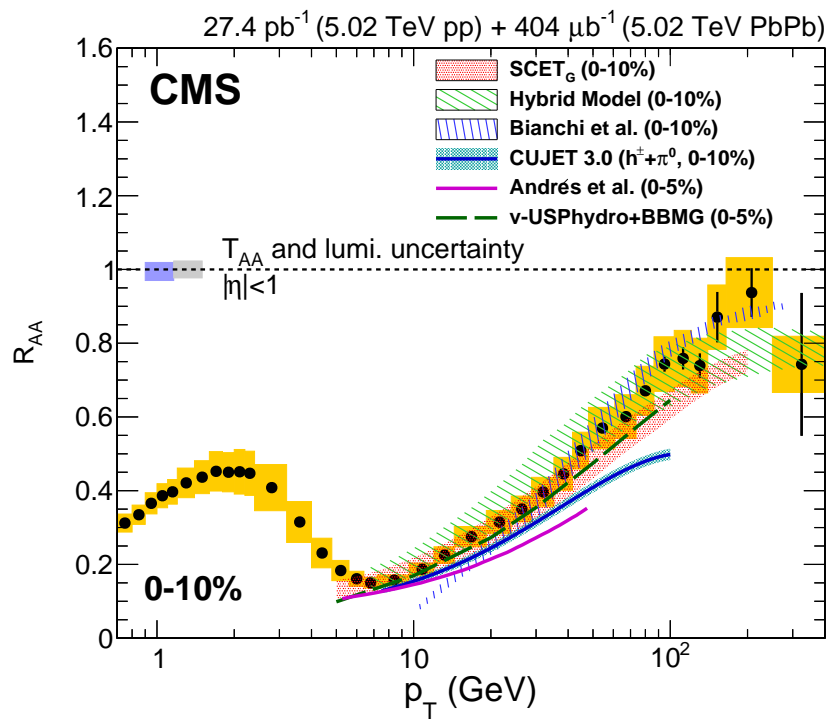


Figure 10. Model comparisons to charged particle  $R_{AA}$  in 0-10% central PbPb data at 5.02 TeV from Ref. [14].

- 451 4.2 Quenching model comparisons to high- $p_T$  particle and jet observables
- 452 4.2.1 Quenching model comparisons:  $R_{AA}$
- 453 4.2.2 Quenching model comparisons: jet fragmentation functions
- 454 4.2.3 Quenching model comparisons: jet shapes
- 455 4.2.4 Quenching model comparisons: dijet asymmetry
- 456 4.3 Theoretical motivations for detailed jet-track correlation studies
- 457 4.3.1 Extension of jet shape measurements to large angles
- 458 4.3.2 Detailed characterization of jet peak in separate dimensions  $\Delta\eta$  and  $\Delta\phi$
- 459 4.3.3 Detailed characterization of leading and subleading jet peaks in dijet events
- 460 4.3.4 Decomposition of contributions to momentum balance studies in dijet events

461        **5 THE LARGE HADRON COLLIDER AND THE CMS DETECTOR**

462        **5.1 The Large Hadron Collider**

463        The Large Hadron Collider (LHC), located at CERN near Geneva, is the largest and highest-  
464        energy particle accelerator in the world. It consists of two counter-rotating particle beam line in  
465        a tunnel 26.7 km in circumference, located between 45 m and 170 m underground [23]. During  
466        standard operation, the LHC collides beams of protons accelerated and focused using a series  
467        of superconducting magnets, cooled to below 2 K using supercritical helium. Particle beams are  
468        brought together for collisions at in experimental detectors at four points in the accelerator ring: the  
469        ATLAS, CMS, ALICE, and LHCb detectors. In addition to the proton-proton (pp) data collected  
470        at center-of-mass energies  $\sqrt{S_{NN}} = 7 \text{ TeV}$ ,  $8 \text{ TeV}$ , and  $13 \text{ TeV}$ , the LHC has also been operated  
471        for heavy ion physics by colliding with fully-stripped lead nuclei ( $^{182}\text{Pb}^{82+}$ ) in lead-lead (PbPb)  
472        and proton-lead (pPb) collisions. Heavy ion runs at the LHC have included PbPb data and pp  
473        “reference” runs at  $\sqrt{S_{NN}} = 2.76 \text{ TeV}$  (2011 and 2013, respectively) and  $5.02 \text{ TeV}$  (2015) and pPb  
474        data at  $\sqrt{S_{NN}} = 5.02 \text{ TeV}$  (2013 and 2016) and  $8.16 \text{ TeV}$  (2016). This analysis relies on PbPb  
475        data at  $2.76 \text{ TeV}$  and  $5.02 \text{ TeV}$ , and corresponding pp reference data at the same center-of-mass  
476        energies.

477        In peak proton-proton operation, the LHC collides 2,808 bunches each containing approx-  
478        imately  $10^{11}$  protons with a minimum bunch spacing of 25 ns, for a maximum luminosity of  
479         $10^{34} \text{ cm}^{-2} \text{ s}^{-1}$  delivered to the high-luminosity detectors (ATLAS and CMS). The lead-lead per-  
480        formance target of  $10^{27} \text{ cm}^{-2} \text{ s}^{-1}$  delivered via 592 bunches of  $10^7$  lead ions was slightly exceeded  
481        during the 2015 PbPb run. At this high-intensity frontier, it is common during nominal pp data  
482        collection and possible in PbPb data collection that multiple distinct proton-proton collisions may  
483        occur within a recorded event in a phenomenon known as “pile-up.” However, pile-up is relatively  
484        rare in PbPb collisions due to the lower luminosities, and in the present analysis only one primary  
485        vertex will be considered (with products of any other possible interactions removed via background  
486        subtraction procedures).

487    **5.2 The CMS detector**

488    The CMS detector is named for the Compact Muon Solenoid at its heart: a superconducting magnet  
489    with magnetic field of 3.8 T, length of 13 m, diameter of 6 m, and weight 14,000 tons. Inside  
490    of this solenoid, the detector includes silicon pixel and strip detectors for particle tracking (see  
491    Sec. 5.3 for a detailed explanation), and electromagnetic and hadronic calorimeters (see Sec. 5.4).  
492    Calorimeters within the solenoid volume are complemented by additional calorimetry outside of the  
493    solenoid that provides coverage in the very forward direction close to the beam line, including the  
494    hadronic forward (HF) calorimeter in the region  $3.0 < |\eta| < 5.2$  used in this analysis for centrality  
495    determination, and the Zero Degree and CASTOR calorimeters in the even more forward region.  
496    The CMS detector also includes an extensive muon system outside of the solenoid volume, consisting  
497    of aluminum drift tubes in the barrel region, cathode strip chambers in the forward region, and a  
498    complementary system of resistive plate chambers (not discussed in detail here as muons are not of  
499    primary relevance to this analysis). Full details about the CMS detector may be found in Ref. [24],  
500    and a perspective drawing of the CMS detector from this report is shown in Fig. 11.

501       In the CMS detector, the  $+z$  axis is defined to be horizontal, pointing to the West along  
502    the beam line direction. The  $x$  axis is horizontal, pointing to the South toward the center of the  
503    LHC. The  $+y$  axis is vertical, pointing upward. The azimuthal angle  $\phi = \tan^{-1}(\frac{y}{x})$  is defined in  
504    the  $x$ - $y$  plane such that  $\phi = 0$  is the  $+x$  axis. Pseudorapidity  $\eta = -\ln(\tan(\frac{\theta}{2}))$  is defined to have the  
505    same sign as the  $+z$  axis. Pseudorapidity coverage in the CMS detector ranges from  $\eta = 0$  at the  
506     $y$ -axis, to  $|\eta| > 8.3$  in Zero Degree Calorimeter approaching the  $+/z$  axis.

507    **5.3 Trackers in the CMS detector**

508    The CMS tracking system consists of a small silicon pixel detector for precise measurement near  
509    the interaction point (with three layers with radii 4.4 cm to 10.2 cm), surrounded by a large silicon  
510    strip detector with layers to a radius of 110 cm. In both detectors, a cylindrical tracker “barrel” is  
511    complemented by “endcap” disks that together provide full azimuthal coverage and pseudorapidity  
512    coverage in the range  $|\eta| < 2.5$ . The pixel detector consists of 66 million pixels in 1440 modules.  
513    It provides three-dimensional measurements of “hits,” or interactions of particles with tracker  
514    materials, with a transverse resolution  $10\mu\text{m}$  and longitudinal resolution  $20 - 40\mu\text{m}$  (and a third

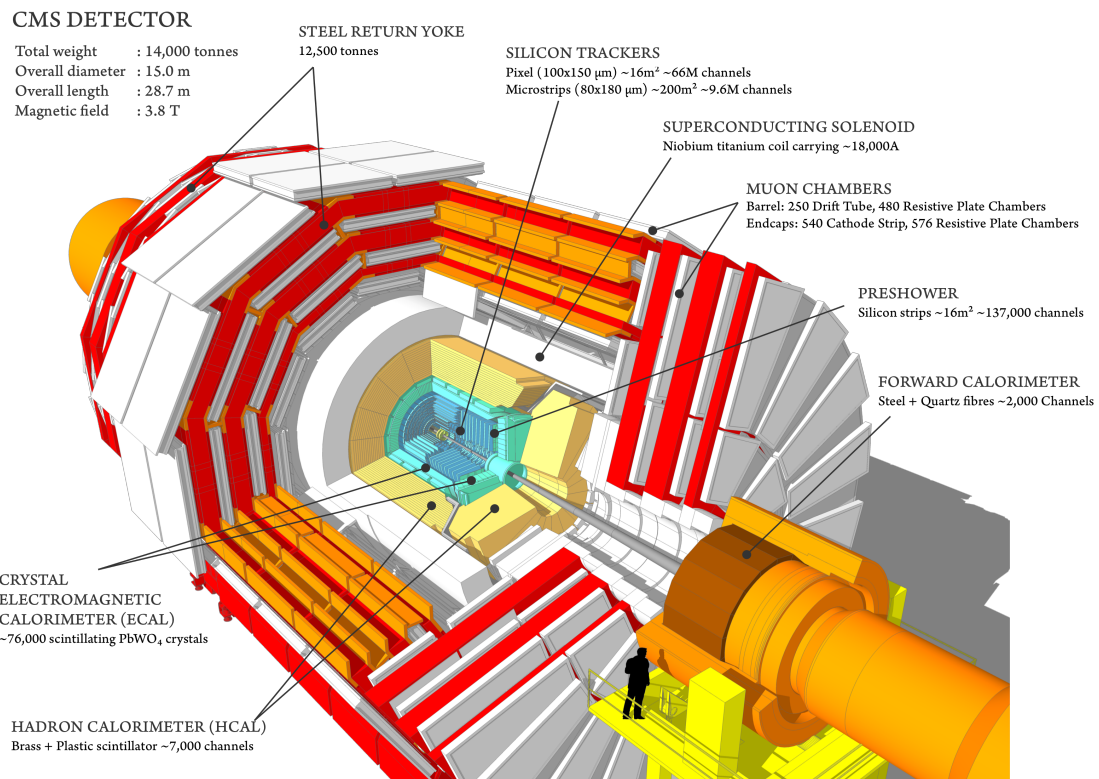


Figure 11. Perspective rendering of the CMS detector, showing component sub-detectors with a human included for scale perspective [25].

coordinate provided by the pixel plane). The silicon strip detector consists of 9.3 million strips in 15,148 modules, organized in four components: Tracker Inner Barrel (TIB) and Disks (TID), Tracker Outer Barrel (TOB, covering the region  $r > 55$  cm), and Tracker End Caps (TEC, covering the region  $124 < |z| < 282$  cm). Figure 12 shows a diagram of the pixel and strip detectors, which have total length 5.8 m and diameter 2.5 m [26]. Track reconstruction and tracking efficiency will be discussed in detail in Sec. 6.

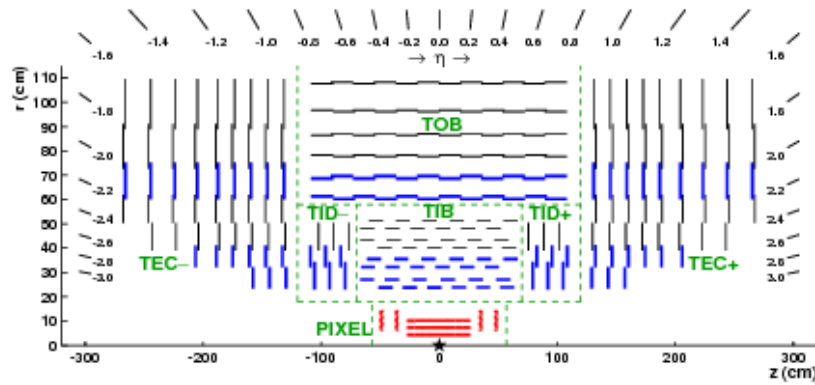


Figure 12. Diagram of CMS pixel and silicon strip detectors in the  $r - z$  plane [26].

#### 521 5.4 Calorimeters in the CMS detector

522 This analysis relies on electromagnetic and hadronic calorimeters for the energy measurements used  
 523 as inputs for the reconstruction of high- $p_T$  jets. The ECAL, which measures the energy of charged  
 524 particles, consists of 75 848 lead tungstate ( $\text{PbWO}_4$ ) crystal scintillators, organized in 5 arrays,  
 525 covering  $|\eta| < 1.48$  in a barrel region and  $1.48 < |\eta| < 3.0$  in the endcap region. Light from the  
 526 scintillators is captured with avalanche photodiodes in the barrel region, and vacuum phototriodes  
 527 in the endcap region. A preshower detector system in front of the ECAL is used to assist in the  
 528 identification of neutral pions and electrons [24]. ECAL energy resolution ranges from about 1-  
 529 2.5% (depending  $|\eta|$  and photon conversion) in the barrel region, and from 2.5-4% in the endcap  
 530 region. [27].

531 Hadrons pass through the ECAL and are stopped by the HCAL, a hermetic detector which  
 532 records their energy using a system of scintillator tiles embedded with wavelength-shifting fibers.

533 The HCAL has three regions, as shown in Fig. 13: barrel (HB), endcap (HE), and an outer region  
 534 (HO) outside of the solenoid, necessitated by the fact that the HB is volume-limited by the solenoid  
 535 diameter. In the barrel region  $|\eta| < 1.74$ , the HCAL cells have widths of 0.087 in pseudorapidity  
 536 and 0.087 in  $\phi$ , while for  $|\eta| > 1.74$  the coverage of the towers increases progressively to a maximum  
 537 of 0.174 in  $\Delta\eta$  and  $\Delta\phi$ . HCAL towers are mapped onto ECAL towers within the barrel region, and  
 538 their summed energies are used to determine the location, energy, and axis of jets, as described  
 539 below in Sec. 7. The HCAL is complimented in the forward region by the HF calorimeters, which  
 540 each consist quartz fibers in the  $\pm z$  directions organized in 432 readout towers in the region  $3.0 <$   
 541  $|\eta| < 5.2$  [24]. In this analysis, only jets from the barrel region of the calorimeters will be included,  
 542 while the HF detector is used for the determination of PbPb event centrality as described in Sec. 8.2.

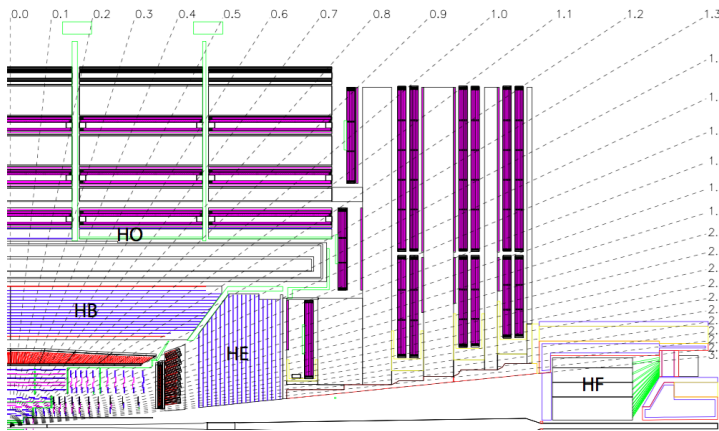


Figure 13. Diagram of the HCAL [24].

## 543 5.5 The CMS trigger system

544 The collision rate at the LHC is so high that it is impossible to store and process every event  
 545 that occurs in the CMS detector. A two-level online trigger system is therefore used to select events  
 546 of interest. Furthermore, data selected with loose trigger requirements (for example “zero bias”  
 547 data with no selection criteria and “minimum bias” criteria consisting of minimal requirements to  
 548 demonstrate the presence of a collision event) may also need to be further “prescaled” to limit  
 549 the rate of recorded events by a specified factor. The trigger system consists of a first (L1) trigger  
 550 consisting of programmable electronics that use information from the calorimeter and muon systems

551 of the detector to select events to record. The L1 trigger operates with an interval of approximately  
552  $4\mu$  s, with a maximum rate of 100 kHz. The next trigger level, the High Level Trigger (HLT), consists  
553 of a processor farm that allows for more sophisticated event selection based on the reconstruction of  
554 physics objects. Reconstruction is performed in a series of steps, or a “HLT path,” chosen to apply  
555 selection in order of increasing reconstruction complexity, so as to minimize processing time [28].  
556 This analysis will rely primarily on two kinds of triggers: minimum bias data, and jet-triggered  
557 data samples selected by requiring the presence of an online reconstructed jet with  $p_T > 80$  GeV  
558 ( $p_T > 100$  GeV for 5.02 TeV PbPb data). No prescale is applied for the jet-triggered data samples  
559 used in this analysis.

## 6 TRACK RECONSTRUCTION AND CORRECTION

### 561 6.1 Track reconstruction in pp collisions

562 Standard track reconstruction in CMS occurs in the following steps, summarized here and described  
 563 in detail in Ref. [26]:

- 564     • **Hit reconstruction** – In the pixel tracker, zero-suppression is performed by setting an ad-  
       565       justable threshold, equivalent charge to 3200 for each pixel. Pixel hits are reconstructed as  
       566       clusters of adjacent pixels, requiring a minimum charge equivalent of 4000 electrons (compared  
       567       to at least 21,000 electrons deposited by a typical ionizing particle). In the strip detector,  
       568       zero-suppression is performed by subtracting the baseline pedestal and noise from the signal,  
       569       and clusters are seeded with channels which contain charge at least three times that of the  
       570       pedestal. Adjacent strips are added to the cluster if their charge is more than twice that of  
       571       the pedestal, and the cluster is kept if its total charge is at least five times larger than the  
       572       combined strip noise. Cluster position in the strip detector is determined from the charge-  
       573       weighted average of strip positions, corrected for Lorentz drift. The average efficiency for hit  
       574       reconstruction in both the pixel and strip detectors (excluding 2.4% of pixel modules and  
       575       2.3% of strip modules known to be defective) is > 99 %.

- 576     • **Track seed generation** – Track reconstruction begins by first running a fast track and  
       577       vertex reconstruction using the pixel tracker only to reconstruct the beamspot position and  
       578       the location of primary vertices in the event. After this, track reconstruction is carried out in  
       579       six iterations, each of which begins with “seeds” that define the trajectories and uncertainties  
       580       of potential tracks. The first set of seeds are pixel triplets, produced from corresponding sets  
       581       of three pixel hits (on a helical track trajectory) with weak constraints on compatibility with  
       582       the beam spot to require that the tracks correspond to promptly produced particles. In later  
       583       iterations, additional information from vertex reconstruction and the silicon strip detector is  
       584       incorporated in seed generation.

- 585     • **Track finding** – The seeds generated in the step above are used as starting points for  
       586       track-finding based on the Kalman filter method, implemented in four steps for each tracker  
       587       layer. First, track parameters at the starting level are extrapolated, assuming a perfectly

588 helical track trajectory (neglecting multiple scatterings, energy loss, and non-uniformity in  
589 the magnetic field), to determine the locations of interception in other pixel layers. The second  
590 step is a search for tracker modules consistent with the interception locations determined in  
591 the previous step. In the third step, hits from mutually exclusive module groups (i.e. groups  
592 of modules for which it is not possible that one track could pass through more than one of  
593 the grouped modules) are used to update and refine hit locations (including the possibility of  
594 adding “ghost” hits where a particle failed to produce a hit due to module inefficiency) and to  
595 calculate the Lorentz drift in the silicon bulk. Finally, in the fourth and last step, new track  
596 candidates are formed by adding one compatible hit from each of the module groupings, and  
597 trajectories are updated combining this added hit with the original track path extrapolation.  
598 All track candidates at a given level are then extrapolated to the next compatible layer and  
599 the procedure repeated through five iterations.

- 600 • **Track fitting** – Finally, the track trajectory is refitted to reduce possible biases (due, for  
601 example, to the beam spot constraint introduced in initial seed finding), and to remove  
602 outlying hits falsely associated to a track.

603 After tracks are reconstructed according to this procedure, the track sample both includes a contri-  
604 bution from “fake” tracks (that do not correspond to the trajectory of an ionizing particle), which  
605 is reduced by requiring certain selection criteria as discussed in Sec. 6.3. The collection also suffers  
606 from detector and reconstruction inefficiencies, which are corrected in this analysis according to  
607 the procedure described in Sec. 6.4.

## 608 6.2 Track reconstruction in PbPb collisions

609 In PbPb collision data, dedicated track reconstruction is necessary due to the dramatically greater  
610 multiplicity in PbPb compared to pp collisions. This heavy ion tracking occurs in the following  
611 steps, and is detailed in Refs. [29] and [30]:

- 612 • **Hit reconstruction** – Tracker hits are reconstructed following the same basic procedure  
613 applied in pp collisions.
- 614 • **Track seed generation** – First, primary vertex positions are reconstructed using only a  
615 collection of pixel hits, extrapolated to the region near the beam spot. In PbPb data pileup

616       is negligible, so there is generally only one primary vertex reconstructed in each event. Initial  
617       track seeds are then constructed from pixel triplets only. To reduce combinatorial back-  
618       grounds, seeds are restricted to those pointing to a region within 2 mm of the primary vertex,  
619       and further selections are applied on track  $p_T$ , goodness-of-fit ( $\chi^2$ ), and compatibility between  
620       the seed trajectory and the primary vertex.

621       • **Track finding** – Track trajectories are propagated through the tracker following a procedure  
622       similar to that outlined above for pp data. The track seeding and finding procedure is repeated  
623       through three iterations. In the second and third iterations, hits belonging unambiguously to  
624       a previously identified tracks are first removed, and then reconstruction is repeated using pixel  
625       triplet and pixel pair seeds (in the 2nd and 3rd iterations, respectively). Tracks identified in  
626       these later iterations are merged into first-iteration tracks, with duplicates removed based on  
627       hit matching.

### 628       6.3 High purity tracks

629       The track reconstruction procedures described above for pp and PbPb collision data give track  
630       collections with significant “fake rates,” or fraction of reconstructed tracks that cannot be associated  
631       with a particle. This fake rate is reduced with a series of quality selections, defined in three levels:  
632       “loose” criteria define the minimum to keep tracks in track collections, “tight” criteria are somewhat  
633       more stringent (sacrificing some lost efficiency for a lower fake rate), and finally “high purity”  
634       criteria are most strict and are those applied for most CMS analyses, including those reported  
635       here. Track quality in each case is set with flags for each track, and criteria in each case are  
636       applied separately at each iterative tracking step. The precise criteria for high purity tracks at  
637       each iterative pass are defined in Refs. [26, 29, 30], and include the following types of selections,  
638       imposed as a function of  $p_T$  and  $\eta$ :

- 639       • Requirements on the number of hits on the track trajectory ( $N_{\text{hit}}$ )
- 640       • Requirements on the minimum layers in which the track has an associated hit ( $N_{\text{layers}}$ , and  
641       on the maximum intercepted layers in which the track has no assigned hits)
- 642       • A minimum imposed on the goodness-of-fit of the track ( $\chi^2/\text{Ndof}/N_{\text{layers}}$  or  $\chi^2/N_{\text{hit}}$ )

- 643     • A maximum on relative track- $p_T$  uncertainty
- 644     • Maxima on longitudinal and transverse impact parameters ( $d_z$  and  $d_{xy}$ ) with respect to the  
645       primary vertex position and beam spot
- 646     In pp data, criteria are optimized by the quality metric  $Q(\rho) = s/\sqrt{s + \rho b}$ , where  $s$  = selected  
647       ("real") tracks,  $b$  = selected fake tracks, and parameter  $\rho \approx 10$  weights the metric toward min-  
648       imizing the fake rate. In PbPb data from Run 2, optimization is performed via the output of a  
649       multivariate analysis tool (MVA), as detailed in Ref. [30].
- 650     **6.4 Tracking efficiency and fake rate evaluation and correction**
- 651     Tracking efficiency for charged particles in pp collisions ranges from approximately 80% at  $p_T \approx 0.5$  GeV  
652     to 90% or better at  $p_T \approx 10$  GeV and higher. Track reconstruction is more difficult in the heavy-ion  
653     environment due to the high track multiplicity, and tracking efficiency for PbPb collisions ranges  
654     from approximately 30% at 0.5 GeV to about 70% at 10 GeV. Tracking efficiencies are evaluated  
655     using PYTHIA and PYTHIA+HYDJET Monte Carlo simulation, by comparing track distributions as  
656     generated to those after MC samples are passed through GEANT detector simulation and recon-  
657     structed with the algorithms used to reconstruct data. Corrections are derived as a function of  
658     centrality,  $p_T$ ,  $\eta$ ,  $\phi$ , and local charged particle density. Tracking efficiency closure and systematic  
659     uncertainty is evaluated in pythia and pythia+hydjet, comparing generated track  $p_T$ ,  $\eta$ , and  $\phi$  dis-  
660     tributions to reconstructed distributions before and after correction. For illustration, examples of  
661     these closure checks for 5.02 TeV PYTHIA simulation are shown in Fig. 14. Additional 5% residual  
662     systematic uncertainty is conservatively assigned for possible differences between MC and data that  
663     might affect tracking performance.

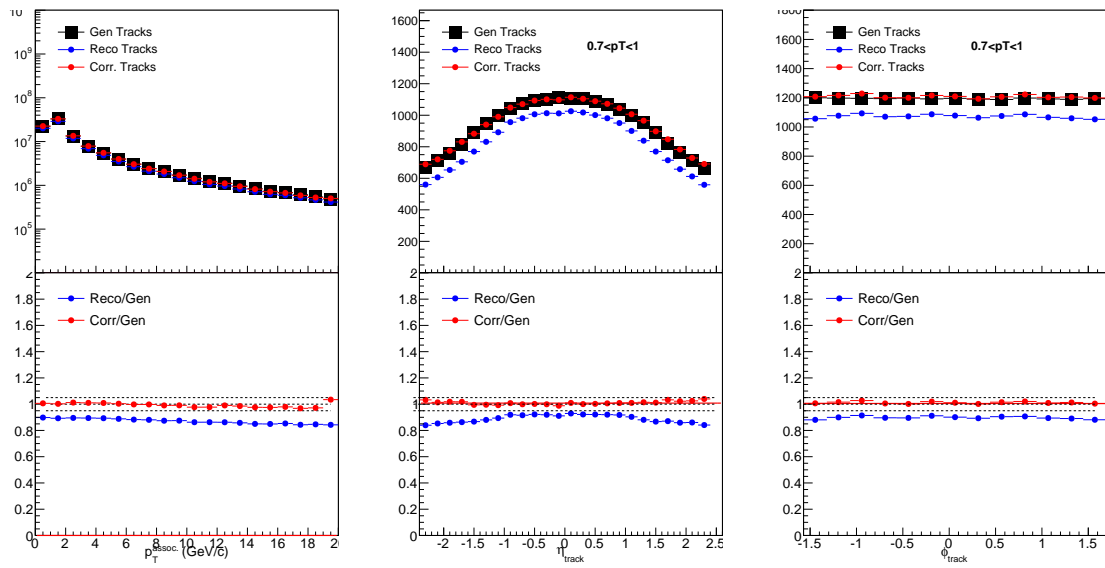


Figure 14. Tracking efficiency correction closure for PYTHIA simulation at 5.02 TeV, comparing tracking generated tracks to uncorrected and corrected reconstructed tracks, as a function of track  $p_T$  and of pseudorapidity, and azimuth for the lowest  $p_T^{\text{trk}}$  bin.

## 7 JET RECONSTRUCTION AND CORRECTION

### 665 7.1 Jet reconstruction with the anti- $k_t$ algorithm

666 The goal in jet reconstruction is to identify clusters of hadrons originating from a fragmenting high-  
 667 energy parton. In high- $p_T$  jet studies in pp collisions, the general locations of jets in an event may  
 668 be qualitatively obvious via large energy deposits in calorimeters; however, there is no clear single  
 669 standard of how jet boundaries should be drawn. In practice, jets are defined by the algorithms  
 670 used to find and determine their direction. These algorithms fall in two primary categories: “cone  
 671 algorithms,” which define jets within specific conical regions (based on the fact that hadronization  
 672 has little effect total momentum flow), and “sequential recombination algorithms,” which iteratively  
 673 identify and cluster pairs of closest particles to form jets that are not necessarily conical. [31, 32, 33].  
 674 Several properties are desireable, from theoretical and experimental perspectives, in jet finding:

- 675     • Straightforward implementation for both theoretical calculations and jet-finding and recon-  
 676         struction in experimental measurements
- 677     • Cross-sections that are finite in perturbation theory
- 678     • Infrared and collinear (IRC) safety – the property that a soft collinear emission in a parton  
 679         splitting should not modify the overall collection of hard (high- $p_T$ ) jets in the event, in  
 680         particular avoiding the possibility of non-cancelling divergences in perturbation calculations
- 681     • Soft resilience – clustering jets that are reasonably regular and not overly sensitive to soft  
 682         particles, a property motivated by the finite resolution of experimental detectors.

683 Heavy ion jet studies in CMS use the anti- $k_t$  algorithm, a soft-resilient, IRC safe, and straightforward  
 684 sequential recombination algorithm [32], implemented in the FastJet framework [33]. The anti- $k_t$   
 685 algorithm clusters entities (calorimeter towers, particles, or partially clustered pseudo-jets)  $i$  and  
 686  $j$  based on the distance measures  $d_{ij}$  between the two particles and  $d_{iB}$  between the particle and  
 687 beam, with the measures defined as:

$$d_{ij} = \min(k_{ti}^{-2}, k_{tj}^{-2}) \frac{(\Delta R_{ij})^2}{R^2}, \quad (8)$$

$$d_{iB} = k_{ti}^{-2}, \quad (9)$$

688 where  $k_{ti}$  refers to the transverse momentum of particle  $i$ ,  $\Delta R_{ij}$  refers to the spatial distance  
 689 (in rapidity and azimuth) between the two particles, and radius parameter  $R$  is a reconstruction  
 690 parameter. The name anti- $k_t$  derives from the negative exponent for  $k_t$  (in contrast to other  
 691 sequential recombination algorithms), which enables IRC safety and soft resilience by making jet  
 692 shape sensitivity to a particle inversely correlated to the particle's transverse momentum. With  
 693 this low sensitivity to soft particles, the anti- $k_t$  algorithm results in a collection of mostly circular  
 694 jets (except in the case of jets separated by less than  $2R$ , in which each jet has a radius of  $\pi R^2$ ).  
 695 The choice of parameter  $R$  is a trade-off between capturing more fragmentation products (as can  
 696 extend as far as  $\Delta R_{ij} = 0.8$  in pp collisions), and limiting the influence of background particles  
 697 in jet reconstruction. In heavy ion experimental studies, where background levels are very high,  
 698 typical choices of  $R$  range from 0.2 to 0.5.

699 With the CMS detector, jets may be clustered from ECAL and HCAL information only  
 700 (“calorimeter jets”) or from information from the full detector, using the particle flow (PF) algo-  
 701 rithm. The PF algorithm improves jet energy resolution (JER) substantially at low- $p_T$  (at 10 GeV  
 702 JER is 15% for PF jets versus 40% for calorimeter jets) with improvements decreasing for higher- $p_T$   
 703 jets (at 100 GeV PF jet JER is 8% versus 12% for calorimeter jets, falling to a difference of 4%  
 704 versus 5% at 1 TeV). For jet-track correlation studies, however, the resolution improvements that  
 705 the particle flow algorithm offers come at the cost of enhancing sensitivity to tracking biases in the  
 706 jet-track correlation signal, since low- $p_T$  tracks are included in jet reconstruction. In this analysis,  
 707 calorimeter jets are used to avoid these auto-correlation effects, and because we will consider jets  
 708 with  $p_T > 120$  GeV for which calorimeter jet energy resolution is adequate. Jets are reconstructed  
 709 with anti- $k_t$  radius  $R = 0.3$  for 2.76 TeV data (“ak3Calo” jets), and with radius  $R = 0.4$  for 5.02  
 710 TeV data (“ak4Calo” jets). In pp data at 2.76 TeV and 5.02 TeV the contribution to the jet energy  
 711 from the underlying event (UE) is negligible (less than 1 GeV), so no underlying event subtraction  
 712 is employed.

713 **7.2 Underlying event subtraction in PbPb data**

714 In PbPb collisions it is necessary to subtract contributions from the large underlying event in order  
715 to recover the true jet energy. There are a variety of methods used for underlying event subtraction,  
716 of which the following two are relevant for this analysis.

717 **7.2.1 Noise/pedestal subtraction**

718 In most CMS high- $p_T$  jet analyses, including 5.02 TeV PbPb data studies here, underlying event  
719 subtraction is performed using a variant of an iterative noise/pedestal subtraction technique [34].  
720 This algorithm occurs in the following steps:

- 721 • First, the mean “pedestal” energy in calorimeter cells as a function of energy  $\eta$  ( $P(\eta)$ ) is  
722 calculated along with its dispersion.
- 723 • The pedestal function  $P(\eta)$  is subtracted from all cells.
- 724 • Cells with non-physical negative energy entries are then set to zero.
- 725 •  $\langle E_{\text{cell}} \rangle + \langle \sigma(E_{\text{cell}}) \rangle$  is subtracted from each cell to compensate for the elimination of negative  
726 energy cells.
- 727 • Jets are clustered from the pedestal-subtracted cells using the anti- $k_t$  algorithm.
- 728 • The pedestal function  $P(\eta)$  is then re-derived using only cells that are not a part of clustered  
729 jets, and the algorithm is repeated.

730 After this underlying event subtraction is applied, the anti- $k_t$  algorithm with radius parameter  
731  $R = 0.4$  is then employed for jet reconstruction (“akPu4Calo jets”).

732 **7.2.2 HF/Voronoi subtraction**

733 For 2.76 TeV PbPb data a different algorithm, designed to eliminate the threshold and possible  
734 resulting bias from the noise/pedestal technique, is employed [29]. This algorithm uses information  
735 from the HF detector to model and subtract the underlying event using Voronoi decomposition  
736 (“HF/Voronoi” algorithm) in the following steps:

- 737     • The distribution of underlying  $E_T$  as a function of  $\eta$  and  $\phi$  is modeled using singular value  
 738       decomposition (SVD) training ( $dE_T/d\eta/\phi$  with Voronoi parameters  $v_1 \dots v_4$ ) to extrapolate the  
 739       UE distribution from the HF calorimeter at large  $\eta$  to the central analysis region ( $|\eta| < 1.6$ ).  
 740     • The modeled UE distribution is subtracted from all calorimeter cells.  
 741     • Each calorimeter cell is associated with its nearest neighbors, and energy is redistributed  
 742       between neighboring in an “equalization” procedure used to eliminate non-physical negative  
 743        $E_T$  entries (optimized to minimize energy transfers).
- 744   After Voronoi subtraction and equalization, the anti- $k_t$  algorithm is employed with radius parameter  
 745    $R = 0.3$  to cluster (“akVs3Calo”) jets.

746   **7.3 Jet energy corrections**

747   Jet reconstruction as described above gives spatial coordinates and  $p_T$  for each jet as measured by  
 748   the detector. Our goal in jet studies, however, is to reconstruct the true total parton or particle  
 749   energy. This is achieved through jet energy corrections (JEC) that establish a mapping between  
 750   measured energy (which does not, for example, include neutrinos produced in jet fragmentation)  
 751   and “true” jet energies. This mapping is complicated by nonlinearity in detector response. Ini-  
 752   tial corrections are derived as a function of  $p_T$  and  $\eta$  using dijet QCD samples of PYTHIA and  
 753   PYTHIA+HYDJET Monte Carlo, spatially matching reconstructed jets to generated particles, and  
 754   comparing generated versus reconstructed jet energy for these matched jets. These “MC truth”  
 755   corrections are applied to measured jet energies to return a collection of jets that, on average,  
 756   capture the kinematic distribution of the partons before fragmentation.

757   These corrections do not, however, fully account for the non-linearity of calorimeter re-  
 758   sponse. In particular, in an effect particularly relevant for jet-track correlation studies, the jet  
 759   energy scale depends on jet fragmentation. Given two jets with identical parton energy, the jet  
 760   with softer fragmentation (i.e. jets with a higher fraction low- $p_T$  particles) will be on average re-  
 761   constructed with lower energy than the jet with harder fragmentation. When combined with a jet  
 762   selection threshold, this non-linearity results in a bias that systematically underestimates the jets  
 763   with soft fragmentation in the analysis sample. An additional fragmentation-function dependent  
 764   jet energy correction (JFF-JEC) is therefore applied after initial jet energy corrections in order to

765 reduce this bias (detailed in Ref. [29]). These JFF-JEC are derived using the number of particle flow  
 766 candidates ( $N_{\text{PF}}$ ) in the jet with  $p_T > 2$  GeV, with this threshold chosen to reduce the influence  
 767 of soft fluctuations in the underlying event. Correction tables are derived as a function of  $N_{\text{PF}}$ , jet  
 768  $p_T$ , and PbPb event centrality in PYTHIA and PYTHIA+HYDJET simulation, and are applied to jets  
 769 after the JECs described above. Finally, iterative residual corrections are applied as a function of  
 770 jet  $p_T$ . The application of JFF-JECs reduces the overall quark/gluon non-closure, as illustrated for  
 771 PbPb data in Fig. 15, and slightly improves jet energy resolution overall.

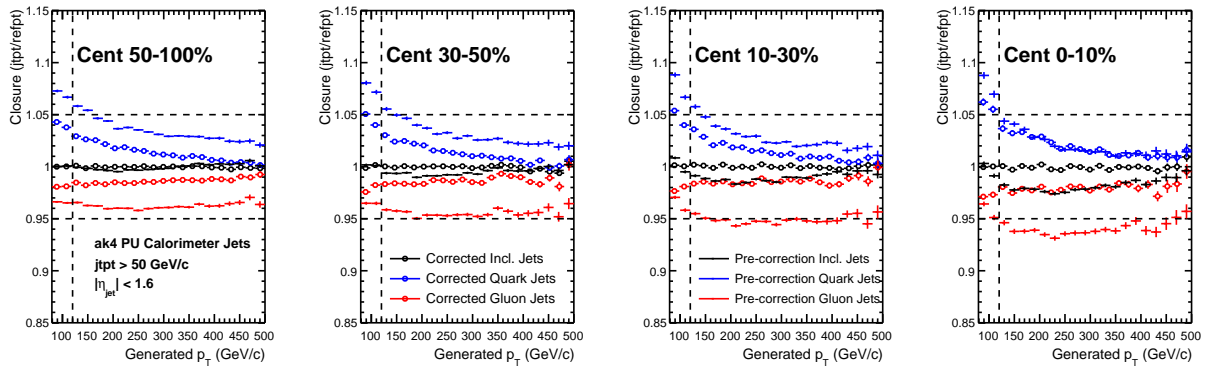


Figure 15. Closure with and without JFF-JEC for quark and gluon jets.

## 8 DATA AND MONTE CARLO SAMPLES

### 773 8.1 Data samples and event selection

774 This analysis is based on PbPb and pp data collected with the CMS detector at 2.76 TeV and 5.02  
 775 TeV during Run 1 and Run 2 of the CERN LHC. Studies at 2.76 TeV use  $166 \mu\text{b}^{-1}$  of PbPb data  
 776 collected in 2011, and  $5.3 \text{ pb}^{-1}$  of pp data collected in 2013. Studies at 5.02 TeV use  $404 \mu\text{b}^{-1}$  of  
 777 PbPb data and  $25 \text{ pb}^{-1}$  of pp data, both collected in 2015. Online collision selection was performed  
 778 using the CMS HLT described in Sec. 5.5 to obtain a minimum bias sample of PbPb collision events,  
 779 and to obtain samples of PbPb and pp data with the requirement that events contain at least one  
 780 high- $p_{\text{T}}$  jet (with  $p_{\text{T}} > 80 \text{ GeV}$  for pp data and 2.76 TeV PbPb data,  $p_{\text{T}} > 100 \text{ GeV}$  for 5.02 TeV  
 781 PbPb data). These jet triggers are fully efficient for offline-reconstructed jets with  $p_{\text{T}} > 120 \text{ GeV}$ .  
 782 Total numbers of selected events are summarized in Table I.

TABLE I. Summary of data samples and number of selected events

Dataset	Number of selected events
2.76 TeV PbPb MinimumBias	1.01 M
2.76 TeV PbPb Jet-triggered ( $p_{\text{T}} > 80 \text{ GeV}$ )	1.25 M
2.76 TeV pp Jet-triggered ( $p_{\text{T}} > 80 \text{ GeV}$ )	1.27 M
5.02 TeV PbPb MinimumBias	764 k
5.02 TeV PbPb Jet-triggered ( $p_{\text{T}} > 100 \text{ GeV}$ )	3.35 M
5.02 TeV pp Jet-triggered ( $p_{\text{T}} > 80 \text{ GeV}$ )	2.66 M

783 A number of quality cuts are applied, as is standard for CMS analyses to remove detector  
 784 noise backgrounds, ultra-peripheral collisions, beam gas, and events with exceptionally large pixel  
 785 occupancy. These selection criteria have shown to have negligible impact on dijet analyses [35, 36],  
 786 and are as follows in PbPb and pp collisions:

- 787 • Vertex-z position within 15 cm of the center of the detector ( $|v_z| < 15$ )

- 788     • Primary vertex filter – a requirement that events include a reconstructed primary vertex filter  
 789       with at least two tracks, requiring the presence of inelastic hadronic scattering and removing  
 790       beam-gas events and ultra-peripheral collisions
- 791     • Beam-scraping filter – a requirement of pixel clusters compatible with the primary vertex.  
 792       In pp, this requires that if there are more than 10 tracks, at least 25% of tracks must be  
 793       highPurity (see Sec. 6)
- 794     • HB/HE noise filter – a filter to exclude events exhibiting uncharacteristic calorimeter noise [37]
- 795     • PbPb data only: HF coincidence filter – at least 3 GeV recorded in at least each of at least  
 796       three hadronic forward calorimeter towers on each side of the interaction point
- 797     These cleaning cuts are applied to both minimum bias and jet-triggered data samples. Additional  
 798     event selection will later be applied to obtain samples of high- $p_T$  jets and dijet events, as discussed  
 799     in Sec. 8.4 below.

## 800   8.2 Collision centrality determination and classes

801     The variable centrality is used to parameterize the degree of overlap of the colliding nuclei. In  
 802     CMS, centrality is determined using total transverse energy ( $E_T$ ) in the HF calorimeter towers, in  
 803     the region  $4.0 < |\eta| < 5.2$ . The distribution of total  $E_T$  in all events is used to divide the total  
 804     minimum bias event sample into centrality bins, each containing 0.5% of the total events. The  
 805     resulting centrality distribution is flat in minimum bias data by construction. In jet-triggered, data,  
 806     however, requiring the presence of a high- $p_T$  jet results in a larger fraction of more central collisions  
 807     (in which hard-scatterings are more likely). The collisions defined as “most central” (centrality =  
 808     0%) are those with the greatest  $E_T$ , corresponding to collisions in which the nuclei collided head-on.  
 809     In contrast, the collisions defined as “least central” or “most peripheral” (centrality = 100%) are  
 810     those in which the nuclei barely overlapped at all. To observe how jet modifications evolve with  
 811     changing centrality, this analysis considers four centrality classes: 0-10% (most central), 10-30%,  
 812     30-50%, and 50-100%.

813 **8.3 Monte Carlo simulation**

814 Monte Carlo (MC) simulation is used in this analysis to evaluate and correct for jet reconstruction  
815 performance and tracking efficiency for both pp and PbPb data. Simulation of pp data and of  
816 the hard processes in PbPb data are performed using the PYTHIA (version 6, tune Z2 [38]) event  
817 generator. In order to have reasonable event samples in all jet  $p_T$  ranges, different samples are  
818 produced with various cut-off values of  $\hat{p}_T$ , which are then combined using their respective cross-  
819 sections as weights. To simulate CMS detector output for MC events, GEANT4 detector simulation  
820 is used [39]. Jet and track reconstruction performance and efficiency for pp data is evaluated by  
821 comparing observables in PYTHIA samples as generated to the same observables after they have  
822 been passed through the detector simulation and the same reconstruction procedures applied to  
823 pp data. For the relevant jet kinematics observables relevant to this analysis, PYTHIA reasonably  
824 reproduces pp data.

825 For PbPb data, the underlying event is simulated using HYDJET (Drum5 tune) [40], which  
826 combines hydrodynamics with “mini-jets” produced with quenched pythia input. Hard processes  
827 are generated using PYTHIA, and are directly embedded in this HYDJET sample (refered to as  
828 PYTHIA+HYDJET simulation), with no medium quenching effects applied to the embedded jets.  
829 This PYTHIA+HYDJET sample is used to evaluate the reconstruction effects of the presence of  
830 the QGP medium, *other* than the jet-medium interactions that are our objects of study. As for  
831 PYTHIA simulation of pp data, comparing PYTHIA+HYDJET samples that have been passed through  
832 the detector and reconstructed chain to the generated Monte Carlo allows for the evaluation of jet  
833 and track reconstruction performance.

834 **8.3.1 Monte Carlo centrality and vertex-z reweighting**

835 Simulated PYTHIA+HYDJET samples are generated minimum bias, and therefore must be reweighted  
836 to match the bias toward more central events induced by requiring the presence of a high- $p_T$   
837 jets discussed in Sec. 8.2. Reweighting factors are calculated for each 0.5%-wide centrality bin,  
838 and applied to the PYTHIA+HYDJET sample overall to match the PbPb centrality distribution.  
839 Similarly, another reweighting procedure is performed to match the distributions of the position of

840 the primary interaction along the beam direction in MC and data for both pp and PbPb collisions.  
841 Figures 16–18 illustrate the necessity and effects of these reweighting procedures.

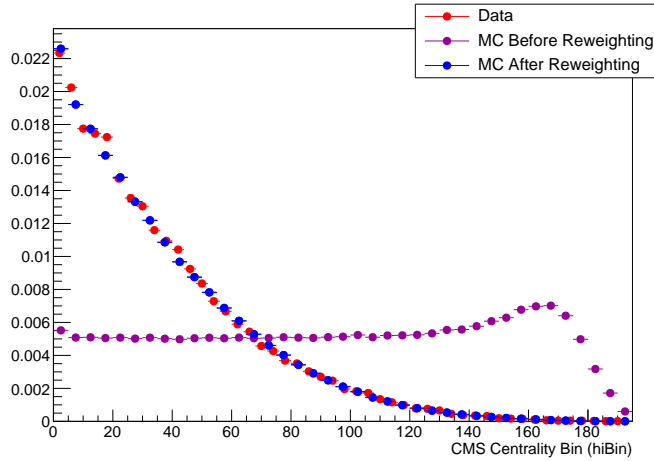


Figure 16. Centrality distribution for PYTHIA+HYDJET reweighted to match centrality distribution of PbPb data.

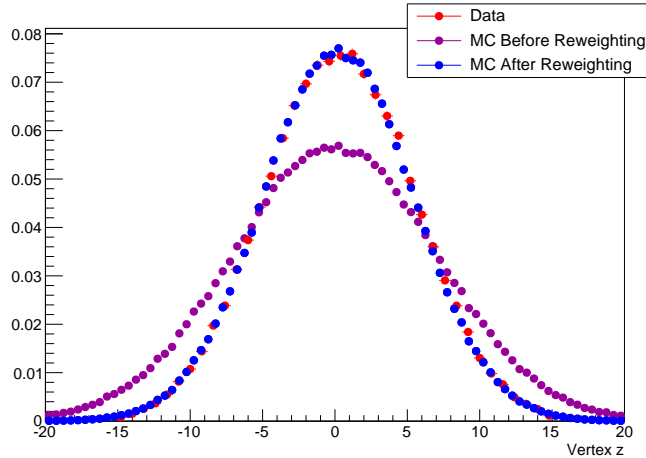


Figure 17. Vertex z distribution for PYTHIA+HYDJET reweighted to match centrality distribution of PbPb data.

### 842 8.3.2 Monte Carlo samples at 2.76 TeV

843 Tables II and III summarize the PYTHIA and PYTHIA+HYDJET samples used in this analysis by  $\hat{p}_T$ ,  
844 with respective numbers of generated events and cross-sections used for combining samples.

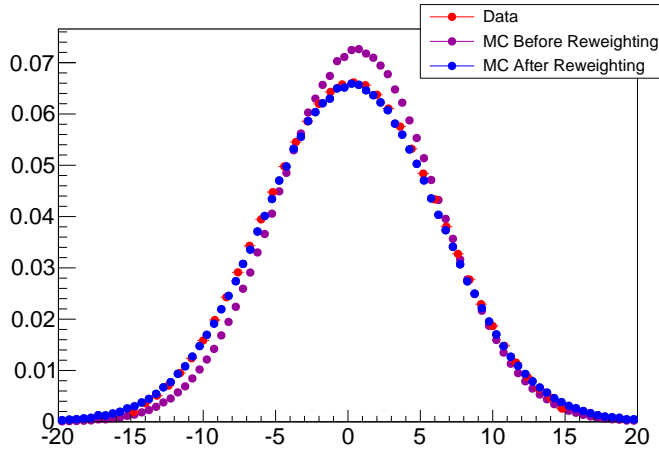


Figure 18. Vertex z distribution for PYTHIA reweighted to match centrality distribution of pp data.

TABLE II. Summary of Monte Carlo samples and generated events at 2.76 TeV

Generator	Process	Cross section (mb)	Number of events
PYTHIA+HYDJET	$\hat{p}_T > 50 \text{ GeV}$	$1.025 \times 10^{-3}$	395k
PYTHIA+HYDJET	$\hat{p}_T > 80 \text{ GeV}$	$9.865 \times 10^{-5}$	368k
PYTHIA+HYDJET	$\hat{p}_T > 120 \text{ GeV}$	$1.129 \times 10^{-5}$	367k
PYTHIA+HYDJET	$\hat{p}_T > 170 \text{ GeV}$	$1.465 \times 10^{-6}$	392k
PYTHIA+HYDJET	$\hat{p}_T > 220 \text{ GeV}$	$2.837 \times 10^{-7}$	181k
PYTHIA+HYDJET	$\hat{p}_T > 280 \text{ GeV}$	$2.837 \times 10^{-7}$	50k
PYTHIA	$\hat{p}_T > 80 \text{ GeV}$	$9.865 \times 10^{-5}$	104k
PYTHIA	$\hat{p}_T > 120 \text{ GeV}$	$1.129 \times 10^{-5}$	975k
PYTHIA	$\hat{p}_T > 170 \text{ GeV}$	$1.465 \times 10^{-6}$	69k

<sup>845</sup> **8.3.3 Summary of Monte Carlo samples at 5.02 TeV**

TABLE III. Summary of Monte Carlo samples and generated events at 5.02 TeV

Generator	Process	Cross section (mb)	Number of events
PYTHIA+HYDJET	$\hat{p}_T > 80 \text{ GeV}/c$	$4.412 \times 10^{-4}$	499k
PYTHIA+HYDJET	$\hat{p}_T > 120 \text{ GeV}/c$	$6.147 \times 10^{-5}$	496k
PYTHIA+HYDJET	$\hat{p}_T > 170 \text{ GeV}/c$	$1.018 \times 10^{-5}$	498k
PYTHIA+HYDJET	$\hat{p}_T > 220 \text{ GeV}/c$	$2.477 \times 10^{-6}$	200k
PYTHIA+HYDJET	$\hat{p}_T > 280 \text{ GeV}/c$	$6.160 \times 10^{-7}$	200k
<hr/>			
PYTHIA	$\hat{p}_T > 80 \text{ GeV}/c$	$4.412 \times 10^{-4}$	500k
PYTHIA	$\hat{p}_T > 120 \text{ GeV}/c$	$6.147 \times 10^{-5}$	500k
PYTHIA	$\hat{p}_T > 170 \text{ GeV}/c$	$1.018 \times 10^{-5}$	499k
PYTHIA	$\hat{p}_T > 220 \text{ GeV}/c$	$2.477 \times 10^{-6}$	200k
PYTHIA	$\hat{p}_T > 280 \text{ GeV}/c$	$6.160 \times 10^{-7}$	200k

846 **8.4 Jet selection and dijet asymmetry classes**

847 Jet selection in this analysis is restricted to the pseudorapidity region  $|\eta_{\text{jet}}| < 1.6$  to ensure stable  
848 reconstruction performance in the calorimeter barrel region. A requirement is also imposed that  
849 the highest- $p_T$  track contains no less than 1% and no more than 98% of the total jet  $p_T$ . In the  
850 jet selection referred to as “inclusive jets” for analysis at both 2.76 TeV and 5.02 TeV, all jets with  
851  $p_{T,\text{jet}} > 120$  GeV are considered. In this selection, it is possible to select more than one jet from  
852 the same event, provided that each jet satisfies the inclusive selection criteria.

853 In addition to the inclusive jet selection, a “dijet” selection of events containing two back-  
854 to-back high- $p_T$  jets is also analyzed for the 2.76 TeV data sample. Events are included in this  
855 sample based on the criteria that they contain highest- $p_T$  “leading” jet with  $p_{T,1} > 120$  GeV  
856 and a second-highest- $p_T$  “subleading” jet with  $p_{T,2} > 50$  GeV with relative azimuthal separation  
857  $\Delta\phi > \frac{5\pi}{6}$ . This dijet sample is subdivided into a sample of relatively “balanced” dijets, with similar  
858  $p_{T,1}$  and  $p_{T,2}$  and a sample of relatively “unbalanced” dijets in which the leading jet has a much  
859 larger  $p_T$  than the subleading jet based on asymmetry parameter  $A_J$ . The balanced’ selection is  
860 defined as those events for which  $A_J < 0.22$ , while the unbalanced selection as defined as those  
861 events for which  $A_J > 0.22$ . The dividing value  $A_J = 0.22$  is chosen for consistency with previous  
862 CMS analyses [22, 41]. In this analysis, 52% of central PbPb events are balanced, while 67% of pp  
863 events are balanced. Jet kinematics for all jet samples (broken down by asymmetry for 2.76 TeV  
864 dijet data) are shown in Appendix A.1 for 2.76 TeV data and in Appendix A.2 for 5.02 TeV data.

865 **8.5 Track selection and classes**

866 Tracks, reconstructed as described in Sec. 6 are required to satisfy the following criteria:

- 867 •  $|\eta_{\text{trk}}| < 2.4$  – restricts to the barrel region of the tracker
- 868 •  $0.5 < p_T^{\text{trk}} < 300$  GeV – excludes very low- $p_T$  tracks where reconstruction performance is not  
869 stable
- 870 • High Purity criteria – see Sec. 6.3
- 871 • Distance of closest approach (DCA) in x-y plane and in z less than 3 times the DCA error –  
872 reduces fraction of tracks not associated with a primary vertex

- 873     • Relative  $p_T^{\text{trk}}$  error less than 30% (10% for 5.02 TeV PbPb data) – removes tracks with very  
 874               poor resolution (has a negligible effect on efficiency as CMS resolution is generally good)
- 875     For 5.02 TeV PbPb data, the following additional criteria are also applied to reduce the contribution  
 876               from misidentified tracks [30]:
- 877         • Exclude tracks with fewer than 11 tracker hits
- 878         • Require that for each track the chi-squared over number of degrees of freedom ( $\chi^2/\text{Ndof}$ ) of  
 879               the track fit, also divided by the number of tracker layers (nLayer) hit as the track passed  
 880               through the detector, is less than 0.15, i.e.  $\chi^2/\text{Ndof}/\text{nLayer} < 0.15$ .
- 881         • For tracks with  $p_T > 20$  GeV (the kinematic region in which misreconstruction is difficult to  
 882               access with Monte Carlo), calorimeter matching is applied: since high- $p_T$  tracks eventually  
 883               deposit their energy in a calorimeter after passing through the tracker, tracks are required  
 884               to be associated with calorimeter transverse energy  $E_T = (E_{\text{ECAL}} + E_{\text{HCAL}})/\cosh(\eta_{\text{trk}})$ , such  
 885               that  $E_T > 0.5p_T^{\text{trk}}$
- 886     After these selection criteria are applied, tracking efficiency corrections are applied as described  
 887               in Sec. 6.4. Tracks in this analysis are considered in the following classes: 0.5–1 GeV, 1–2 GeV,  
 888               2–3 GeV, 3–4 GeV, 4–8 GeV, 8–12 GeV, 12–16 GeV, 16–20 GeV, and above 20 GeV. Not all bins  
 889               are considered in every analysis, and for 5.02 TeV studies the lowest- $p_T^{\text{trk}}$  bin is 0.7–1 GeV.

890 **8.6 Summary of analysis bins**

891 Table IV summarizes the key kinematic selections and bins for the three components to this analysis.  
 892 In all cases, identical selection is applied to PbPb and pp data. Event, jet, and track quality cuts  
 893 are not included in this table.

TABLE IV. Summary of data selections and analysis bins

Variable	2.76 TeV Inclusive	5.02 TeV Inclusive	2.76 TeV Dijets
PbPb Centrality	0-10%, 10-30%, 30-50%, 50-100%	0-10%, 10-30%, 30-50%, 50-100%	0-10%, 10-30%, 30-50%, 50-100%
Jet Selection	$ \eta_{\text{jet}}  < 1.6$ $p_T > 120 \text{ GeV}$	$ \eta_{\text{jet}}  < 1.6$ $p_T > 120 \text{ GeV}$	$ \eta_{\text{jet}}  < 1.6$ $p_{T,1} > 120 \text{ GeV}$ $p_{T,2} > 50 \text{ GeV}$ $\Delta\phi_{1,2} > \frac{5\pi}{6}$
$A_J$ Bins	–	–	$A_J < 0.22$ , $A_J > 0.22$
Track $\eta$	$ \eta_{\text{trk}}  < 2.4$	$ \eta_{\text{trk}}  < 2.4$	$ \eta_{\text{trk}}  < 2.4$
$p_T^{\text{trk}}$ Bins	1-2 GeV, 2-3 GeV, 3-4 GeV, 4-8 GeV	0.7-1 GeV, 1-2 GeV, 2-3 GeV, 3-4 GeV, 4-8 GeV	0.5-1 GeV, 1-2 GeV, 2-3 GeV, 3-4 GeV, 4-8 GeV, 8-300 GeV

## 9 JET-TRACK CORRELATION MEASUREMENTS

### 895 9.1 Analysis procedure

896 Measurements in this analysis are carried out by considering correlations between high- $p_T$  jets and  
 897 tracks in PbPb and pp collisions. Jets are selected within  $\eta < 1.6$  and  $p_T$  above a particular  
 898 threshold. For each jet, the relative separation in pseudorapidity ( $\Delta\eta = \eta_{\text{track}} - \eta_{\text{jet}}$ ) and azimuth  
 899 ( $\Delta\phi = \phi_{\text{track}} - \phi_{\text{jet}}$ ) is measured between the jet and all charged-hadron tracks within  $\eta < 2.4$ . For  
 900 each jet-track pair, these measurements are recorded in a two-dimensional  $\Delta\eta - \Delta\phi$  correlation in  
 901 a particular track transverse momentum ( $p_T^{\text{trk}}$ ) and centrality class. Each correlation is normalized  
 902 by dividing by the number of jets in the sample ( $N_{\text{jets}}$ ), resulting in a signal pair distribution,  
 903  $S(\Delta\eta, \Delta\phi)$ , that gives the per-jet yield of tracks and their relative distance from the jet:

$$904 S(\Delta\eta, \Delta\phi) = \frac{1}{N_{\text{jets}}} \frac{d^2N^{\text{same}}}{d\Delta\eta d\Delta\phi}. \quad (10)$$

904 This procedure results in a two dimensional measurement of the distribution of charged  
 905 tracks with respect to the jet axis. The same procedure may also be repeated, weighting each track  
 906 by its  $p_T^{\text{trk}}$ , in order to obtain a distribution of  $p_T^{\text{trk}}$  with respect to the jet axis. These particle  
 907 density and  $p_T^{\text{trk}}$  correlations form the basis for all results discussed in this analysis. From this  
 908 point, several additional corrections and other steps are necessary to isolate jet-related effects from  
 909 long range and uncorrelated backgrounds. These additional steps are as follows:

- 910     • A correction for jet-track pair acceptance events;
  - 911     • Separation of correlations into short-range jet peaks and and long range components;
  - 912     • Monte Carlo-based corrections for biases related to jet reconstruction.
- 913 After these steps, a range of different observables may be extracted to characterize the multiplicity  
 914 and distribution of tracks and  $p_T^{\text{trk}}$  at both small and large angles from the jet axis.

915 **9.2 Jet-track correlation pair-acceptance correction**

916 This analysis considers  $\Delta\eta$  jet-track separations as large as  $\Delta\eta = 2.5$ . With finite  $\eta$  acceptance for  
 917 both jets and tracks ( $\eta_{\text{jet}} < 1.6$  and  $\eta_{\text{track}} < 2.4$ , tracks that fall within  $\Delta\eta = 2.5$  of a jet may be  
 918 outside the tracking acceptance. This pair acceptance effect results in trapezoidal correlations that  
 919 fall with rising  $|\Delta\eta|$  as tracks are “lost” outside of the acceptance. This effect is purely geometric,  
 920 and may be corrected by reproducing this pair acceptance geometry. This is done by creating a  
 921 “mixed event” correlation in which jets in the sample are correlated to tracks within  $\eta < 2.4$  from  
 922 randomly selected events in a minimum bias PbPb sample, matched in vertex- $z$  position (within 0.5  
 923 cm) and centrality (within 2.5%). This reproduces the pair acceptance geometry from the signal  
 924 correlations:

$$ME(\Delta\eta, \Delta\phi) = \frac{1}{N_{\text{jets}}} \frac{d^2N^{\text{mix}}}{d\Delta\eta d\Delta\phi}, \quad (11)$$

925 is constructed to account for pair-acceptance effects, with  $N^{\text{mix}}$  denoting the number of mixed-  
 926 event jet-track pairs. Dividing the signal correlation  $S(\Delta\eta, \Delta\phi)$ , defined in Equation 10, by this  
 927 mixed event correlation  $ME(\Delta\eta, \Delta\phi)$  yields the corrected per-jet correlated yield distribution, as  
 928 illustrated in Figure 19:

$$\frac{1}{N_{\text{jets}}} \frac{d^2N}{d\Delta\eta d\Delta\phi} = \frac{ME(0, 0)}{ME(\Delta\eta, \Delta\phi)} \times S(\Delta\eta, \Delta\phi). \quad (12)$$

929 **9.3 Separation of correlations into long range and short-range components**

930 After correlations are corrected for pair-acceptance effects, in each correlation we are left with a  
 931 well-defined jet peak sitting at  $\Delta\eta = 0$ ,  $\Delta\phi = 0$  on top of a large combinatoric and long range  
 932 correlated background. For most measurements, it is necessary to isolate this jet peak in order to  
 933 distinguish jet-related effects from eventwise correlations. In order to achieve this, we note that the  
 934 long range correlation is independent of  $\Delta\eta$  at distances larger than  $\Delta\eta = 1.5$  from the jet. This  
 935 “sideband” region ( $1.5 < |\Delta\eta| < 3.0$ ) is used to model the underlying event, capturing both the  
 936 level of the combinatoric background in the event, and also the long range “flow” correlations in  
 937 the event. The assumption of rapidity-independence of the flow harmonics is based on the CMS

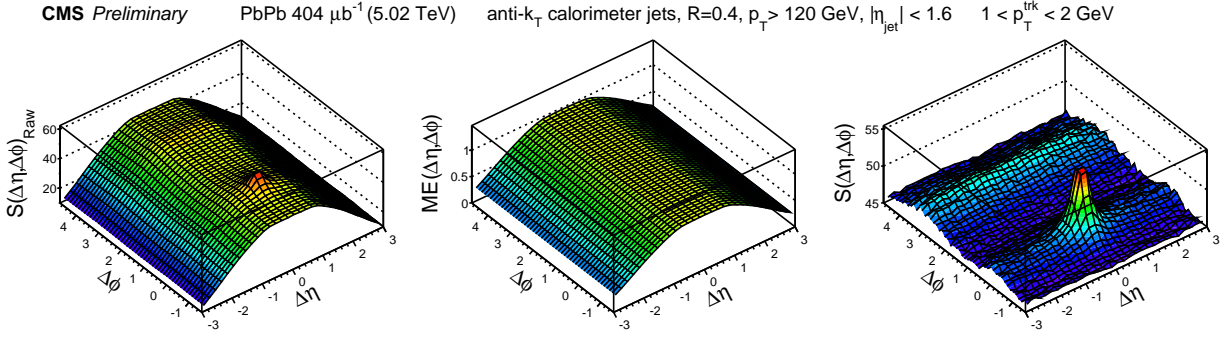


Figure 19. Illustration of the pair-acceptance correction procedure: left panel shows signal correlation  $S(\Delta\eta, \Delta\phi)$ , and center panel shows mixed event correlation  $ME(\Delta\eta, \Delta\phi)$ . Dividing the signal correlation by the mixed event correlation yields the corrected per-jet correlated yield distribution shown in the right panel.

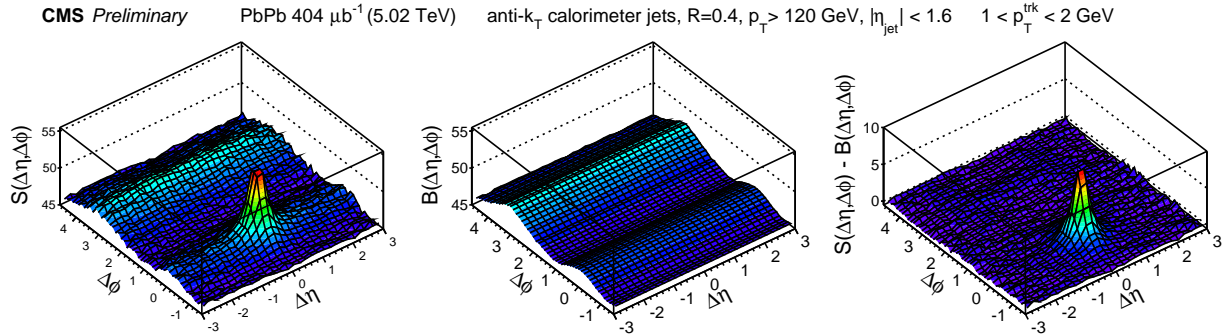


Figure 20. Illustration of the event decomposition procedure without  $\Delta\phi$  fitting: left panel shows the acceptance-corrected correlation, middle panel shows the projected and re-propagated long range distribution, and right panel shows the background-subtracted jet peak.

study [42], which shows no appreciable variation of the elliptic flow for charged particles above 1 GeV in the pseudorapidity interval of  $\Delta\eta < 3.0$  relevant for this study. As long range correlations depend only on  $\Delta\phi$ , the sideband region is projected into  $\Delta\phi$  to obtain a one-dimensional model of the underlying event. To subtract this long range correlation in 2D, this distribution may be either directly re-propagated into  $\Delta\phi$  (as shown in Figure 20), or may be fit in  $\Delta\phi$  before repropagation in a smoothing procedure as shown in Fig. 21.

The long range correlations in this distribution are in themselves interesting objects of study, as these contain information about the collective behavior of particles in the event as a whole, and

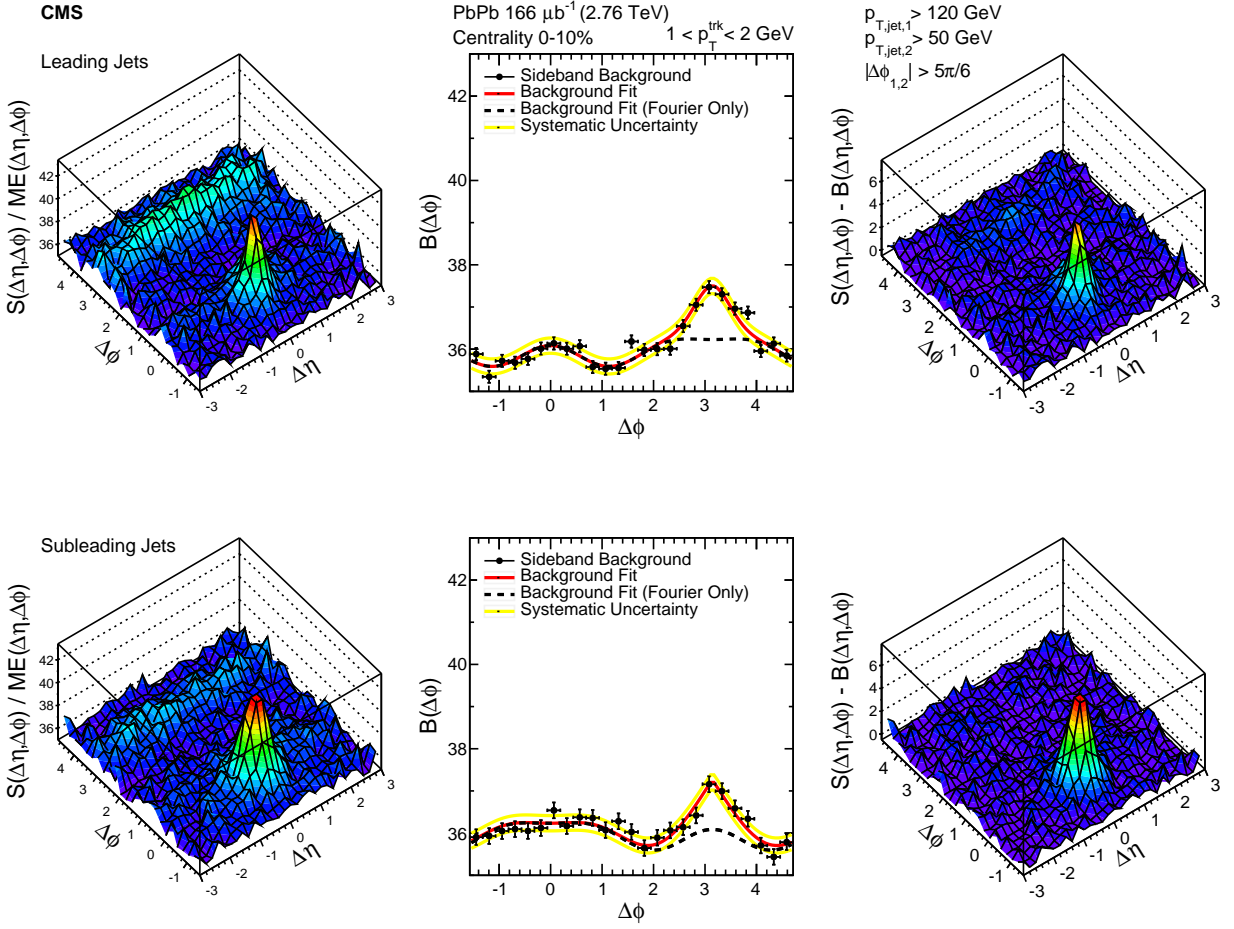


Figure 21. Illustration of the event decomposition procedure with  $\Delta\phi$  fitting: left panel shows the acceptance-corrected correlation, middle panel shows the projected and fit long range distribution, and right panel shows the background-subtracted jet peak.

the extent to which the distribution of high- $p_T$  jets in the event couples to this collective flow. To achieve this, we may apply the well-established method used to study two-particle correlations [43] to correlations between jets and tracks. In correlations to high- $p_T$  jets, however, there is the additional kinematically required contribution to the correlation from the “away-side” peak opposite the jet at  $\Delta\phi = \pi$ ). We therefore fit long range correlations function modeling harmonic flow plus a term to capture the (Gaussian or sharper) peak opposite the jet in relative azimuth:

$$B(\Delta\phi) = B_0(1+2V_1 \cos(\Delta\phi)+2V_2 \cos(2\Delta\phi)+2V_3 \cos(3\Delta\phi))+A_{AS} \exp\left(-\left(\frac{|\Delta\phi-\pi|}{\alpha}\right)^\beta\right), \quad (13)$$

952 For dijet studies, two iterations of fit are performed for each centrality class. In the first  
 953 iteration, we make use of the fact that for our dijet selection and a given value of  $\Delta\eta$  the region  
 954  $-\frac{\pi}{2} < \Delta\phi < \frac{\pi}{2}$  of the leading correlation is by definition equivalent to the region  $\frac{\pi}{2} < \Delta\phi < 3\frac{\pi}{2}$  of  
 955 the subleading correlation. We therefore perform a single fit to the combined background. Here we  
 956 fit with harmonic flow terms only:

$$B(\Delta\phi)^{\text{Dijet}} = B_0(1 + 2V_1 \cos(\Delta\phi) + 2V_2 \cos(2\Delta\phi) + 2V_3 \cos(3\Delta\phi)), \quad (14)$$

957 In this fit, we find that terms through  $V_3$  are necessary to describe the low- $p_T$ , central  
 958 background, while at higher- $p_T$  only  $V_1$ ,  $V_2$ . From this combined fit, we extract parameters  $V_1$ ,  
 959  $V_2$ , and  $V_3$ . Then, to better constrain the background under the signal and minimize the effects  
 960 of random background fluctuations, we apply the factorization relation of overall Fourier harmonic  
 961  $V_2 = v_2^{\text{jet}} \times v_2^{\text{trk}}$  [44, 45]. The values of  $v_2^{\text{trk}}$  for charged particles are determined in Ref. [43], while  
 962 the fit parameter  $v_2$  is expected to be independent of  $p_T^{\text{trk}}$  ranges for a given centrality class. The  
 963 average value of  $v_2^{\text{jet}}$  from each  $p_T^{\text{trk}}$  range is calculated, and used to fix the  $V_2$  parameter on the  
 964 second iteration of the fit. Both the combined dijet fit with  $B(\Delta\phi)^{\text{Dijet}}$  and the final  $B(\Delta\phi)$  fits are  
 965 shown in Appendix B. Through this process, we characterize the underlying event and note that  
 966 the distribution of jets as well as tracks couples to the flow modulation of the underlying event.  
 967 This has immediate consequences for studies of momentum balance between leading and subleading  
 968 hemispheres of the event: as there are non-zero contributions from odd harmonics to the long-range  
 969 correlated backgrounds, we cannot expect flow cancellation when directly subtracting hemishpere  
 970  $p_T^{\text{trk}}$  distributions.

971 For jet peak studies the underlying event is a background to subtracted to isolate jet peaks.  
 972 After this is done, either by direct subtraction or by subtracting the fit and re-propagated back-  
 973 ground, we are left with isolated 2D jet peaks. Before extracting observables, we must carefully  
 974 consider and correct for reconstruction biases affecting these correlated yields. Before correlations  
 975 are constructed, both tracks and jets are corrected for detector efficiencies and other reconstruction  
 976 effects, as discussed in detail in Sec. 6 and Sec. 7, respectively. There are two effects, however, in  
 977 which jet biases are coupled to the multiplicity of low- $p_T$  tracks, that must be corrected after corre-  
 978 lations are constructed and jet peaks are isolated. In the first, although fragmentation-dependent

jet energy corrections are applied to reduce the bias toward selecting jets with harder fragmentation,  
these corrections cannot take into count the softest particles and a residual correction is needed.  
The second arises due to the bias toward selecting jets that sit on upward (soft) fluctuations in  
the background resulting in excess low- $p_T$  yields around the jet axis. Both effects are studied and  
corrections obtained by carrying out the full analysis in Monte Carlo simulation.

#### 984 9.4 Residual Jet Fragmentation Function correction

Jets with harder fragmentation are more likely to be successfully reconstructed than jets with softer  
fragmentation, resulting in a bias toward the selection of jets with fewer associated tracks in both  
pp and PbPb data for all track- $p_T$  selections studied. This bias is partially by the jet fragmentation  
function-dependent jet energy corrections described in Sec. 7. Following the method used in [41],  
corrections are derived for this bias and for the related possible effect of "jet swapping" between  
leading, subleading, and additional jets by comparing correlated per-trigger particle yields for all  
reconstructed jets versus all generated jets. This correction is derived for each jet selection in  
PYTHIA-only simulation, and also in PYTHIA embedded and reconstructed in a HYDJET underlying  
event, excluding HYDJET tracks from the correction determination. As expected considering the  
exclusion of HYDJET tracks, the correction is very similar for pure PYTHIA and for all centralities of  
PYTHIA+HYDJET. For illustration, the derivation and magnitude of these corrections for inclusive  
jets at 2.76 TeV are shown in Figs. 22–25.

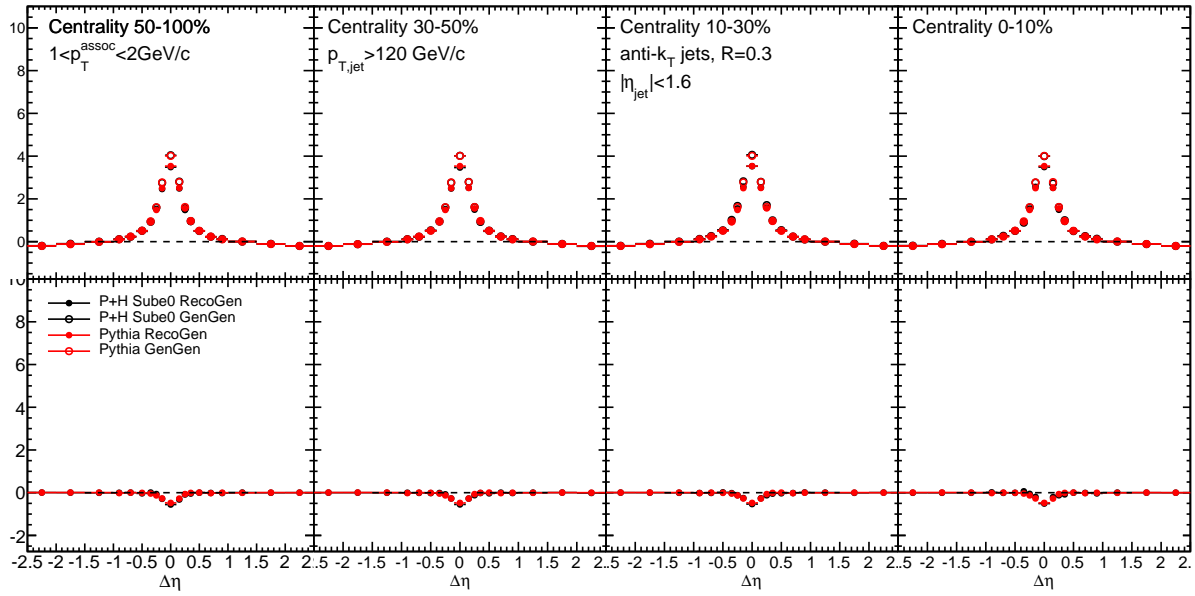


Figure 22.  $\Delta\eta$  jet fragmentation function bias corrections derived by comparing correlations between reconstructed vs. generated jets and generated PYTHIA events, with and without embedding into the HYDJET heavy ion environment, for particles  $1 < p_T^{\text{trk}} < 2 \text{ GeV}$ .

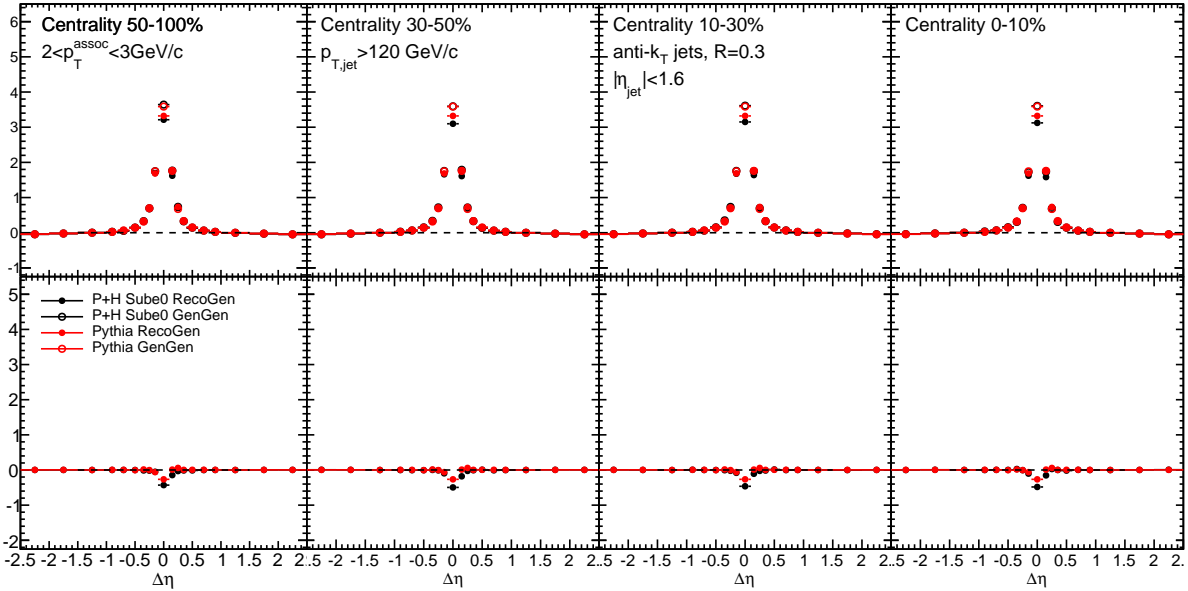


Figure 23.  $\Delta\eta$  jet fragmentation function bias corrections derived by comparing correlations between reconstructed vs. generated jets and generated PYTHIA events, with and without embedding into the HYDJET heavy ion environment, for particles  $2 < p_T^{\text{trk}} < 3 \text{ GeV}$ .

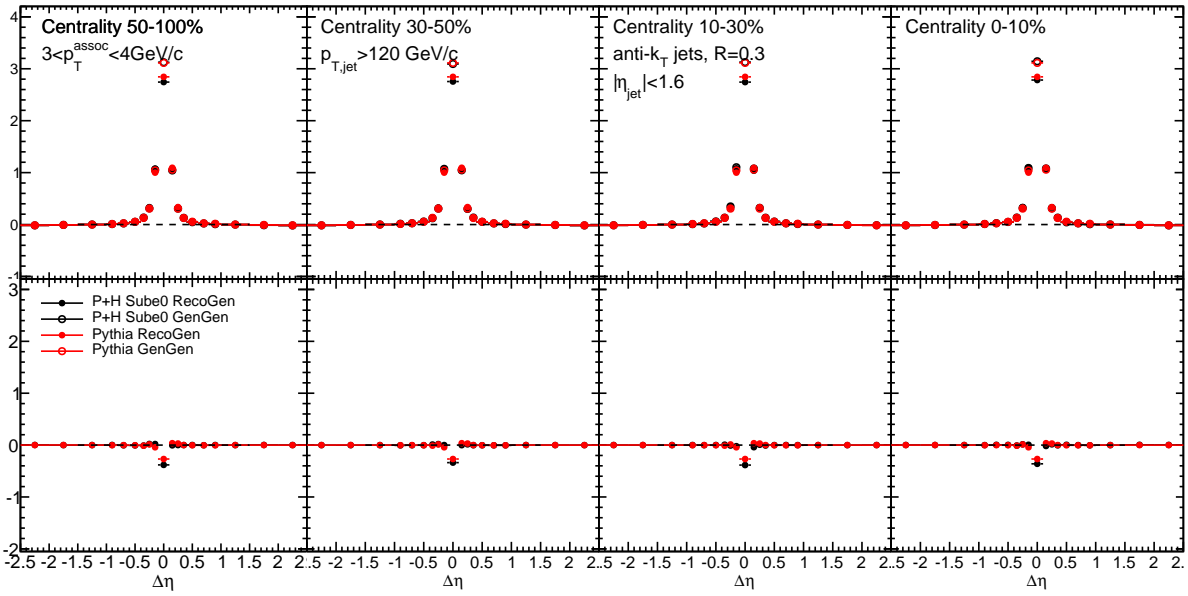


Figure 24.  $\Delta\eta$  jet fragmentation function bias corrections derived by comparing correlations between reconstructed vs. generated jets and generated PYTHIA events, with and without embedding into the HYDJET heavy ion environment, for particles  $3 < p_T^{\text{trk}} < 4 \text{ GeV}$ .

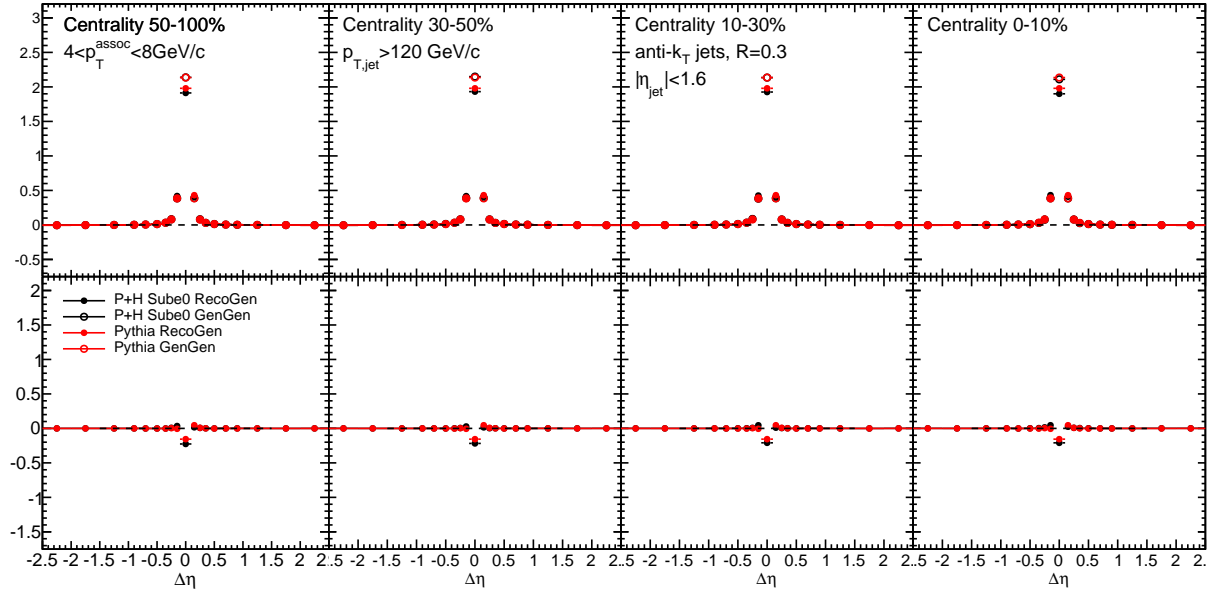


Figure 25.  $\Delta\eta$  jet fragmentation function bias corrections derived by comparing correlations between reconstructed vs. generated jets and generated PYTHIA events, with and without embedding into the HYDJET heavy ion environment, for particles  $4 < p_T^{\text{trk}} < 8 \text{ GeV}$ .

997 To assess the overall effect of these corrections, the integrated yield of these corrections is  
 998 shown as a function of transverse momentum and centrality is shown for inclusive, leading, and  
 999 subleading jets as a function of  $p_T^{\text{trk}}$  in Fig. 26 and as a function of PbPb centrality in Fig. 27.  
 1000 The correction magnitude shows little centrality dependence, and is very similar for pure PYTHIA  
 1001 simulation and PYTHIA embedded into HYDJET.

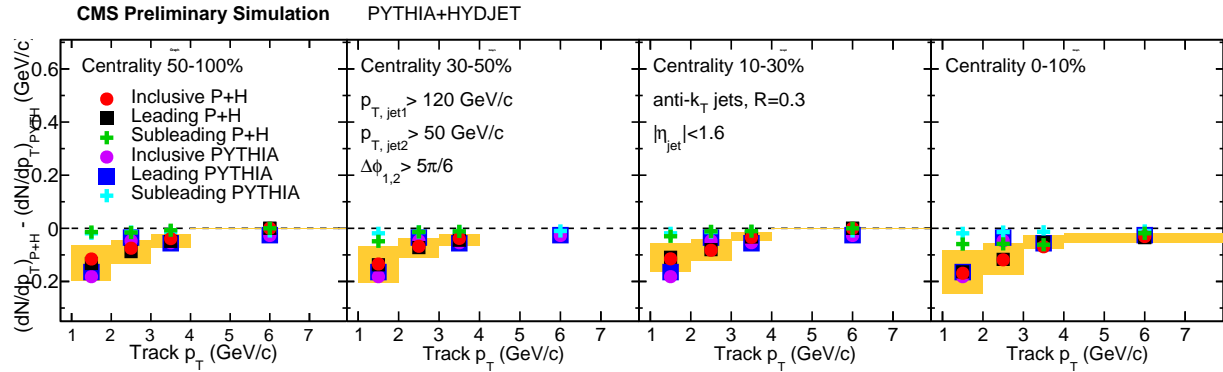


Figure 26. Integrated yield attributed to jet fragmentation function bias in jet reconstruction for PYTHIA alone and embedded into HYDDET, shown as a function of  $p_T^{\text{trk}}$  for each centrality class.

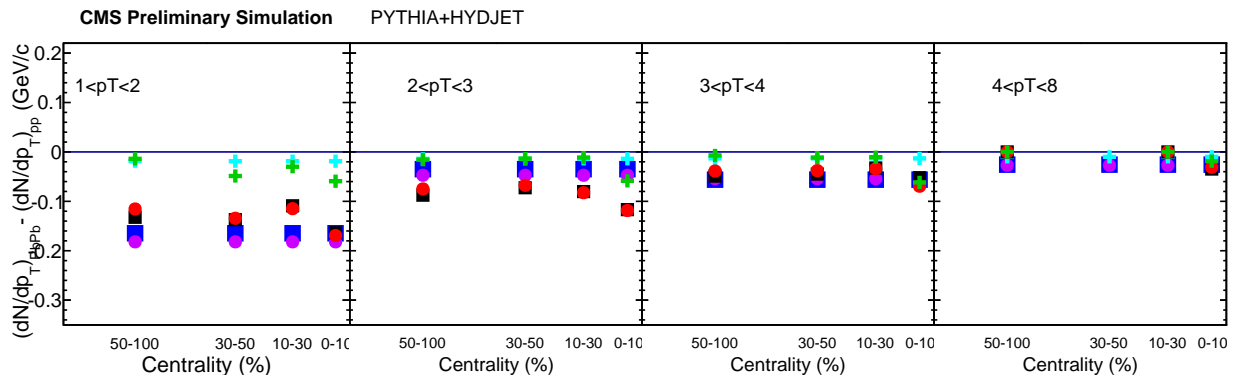


Figure 27. Integrated yield attributed to jet fragmentation function bias in jet reconstruction for PYTHIA alone and embedded into HYDDET, shown as a function of centrality for each associate track  $p_T$  range.

1002    **9.5 Background fluctuation bias correction**

1003    In central PbPb collisions background levels are very high, and naturally fluctuate throughout  
1004    the event. As discussed in Section 7, the process of jet reconstruction in PbPb collisions includes  
1005    background subtraction that accounts for the general distribution of energy in the event. However,  
1006    small, local variations in background levels remain (on the order of 5 GeV within a radius of  $R =$   
1007    0.3). These are reconstructed into the jet, raising or lowering the measured jet energy depending  
1008    on whether the jet sits on an upward or a downward fluctuation in the background. As a result,  
1009    jets with “true”  $p_T$  slightly below the 120 GeV selection threshold that sit on upward background  
1010    fluctuations will be included in the sample, while jets sit on downward will be excluded. Because  
1011    the jet spectrum is steeply falling, it is much more common for a lower- $p_T$  jet (on an upward  
1012    fluctuation) to be included in the sample than for a higher- $p_T$  jet to be excluded. This results in  
1013    the systematic inclusion of tracks from background fluctuations in the peak of tracks observed about  
1014    the jet axis, resulting in a contribution to the initially measured jet peak that must be accurately  
1015    quantified and subtracted.

1016       To estimate and subtract the contribution to the excess yield due to background fluctuation  
1017    bias in jet reconstruction to the measured excess yield, we perform simulations in PYTHIA+HYDJET  
1018    samples with reconstructed jets (but generated tracks, as the tracking efficiency uncertainty is  
1019    analyzed separately), and construct correlations excluding particles generated with the embedded  
1020    PYTHIA hard-scattering process. As the PYTHIA+HYDJET simulation does not include interactions  
1021    between the PYTHIA hard process and the medium, this procedure by construction isolates the  
1022    contribution to the jet peak that is attributable to the background fluctuation bias. The resulting  
1023    corrections are illustrated in Fig. 28 - Fig. 31 for inclusive jets at 2.76 TeV. These correlations show  
1024    a diminishing effect with increasing particle transverse momentum. We subtract the gaussian fit  
1025    to these correlations bin-by-bin from the data results, and also assign the half its magnitude as  
1026    systematic uncertainty to the final measurements. To assess the overall effect of these corrections,  
1027    the integrated yield of these corrections is shown in Fig. 32 as a function of transverse momentum  
1028    and centrality is shown for inclusive, leading, and subleading jets at 2.76 TeV.

1029       Considering that the background fluctuation bias effect in many ways mimics the jet peak  
1030    signal, it is particularly important to validate this correction and confirm both that its origin

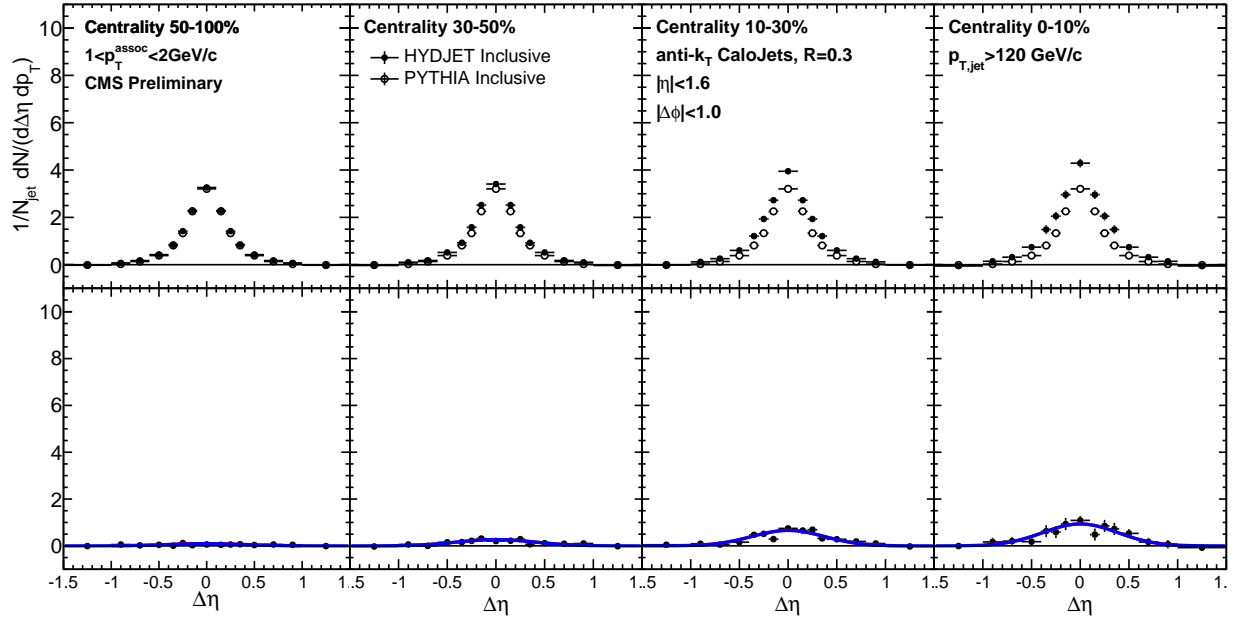


Figure 28.  $\Delta\eta$  background fluctuation bias correction for inclusive jets derived by constructing correlations in PYTHIA+HYDJET between reconstructed jets and only those tracks simulated as part of the heavy ion underlying event rather than the embedded PYTHIA hard process, for particles  $1 < p_T^{\text{trk}} < 2 \text{ GeV}$

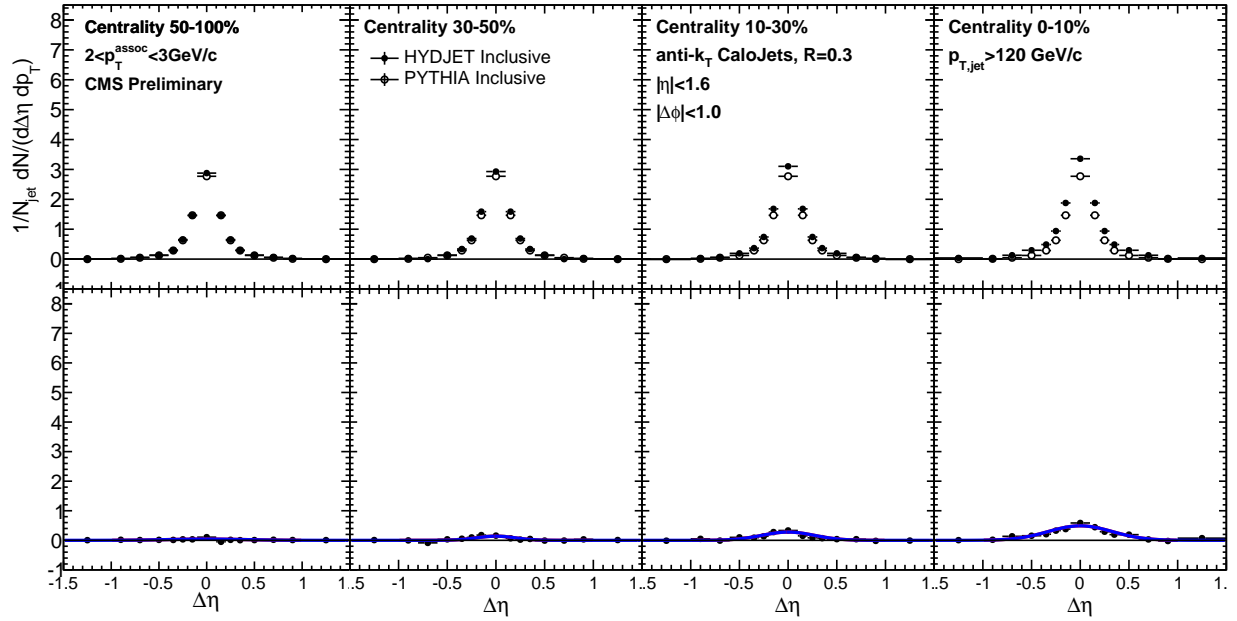


Figure 29.  $\Delta\eta$  background fluctuation bias correction for inclusive jets derived by constructing correlations in PYTHIA+HYDJET between reconstructed jets and only those tracks simulated as part of the heavy ion underlying event rather than the embedded PYTHIA hard process, for particles  $2 < p_T^{\text{trk}} < 3 \text{ GeV}$

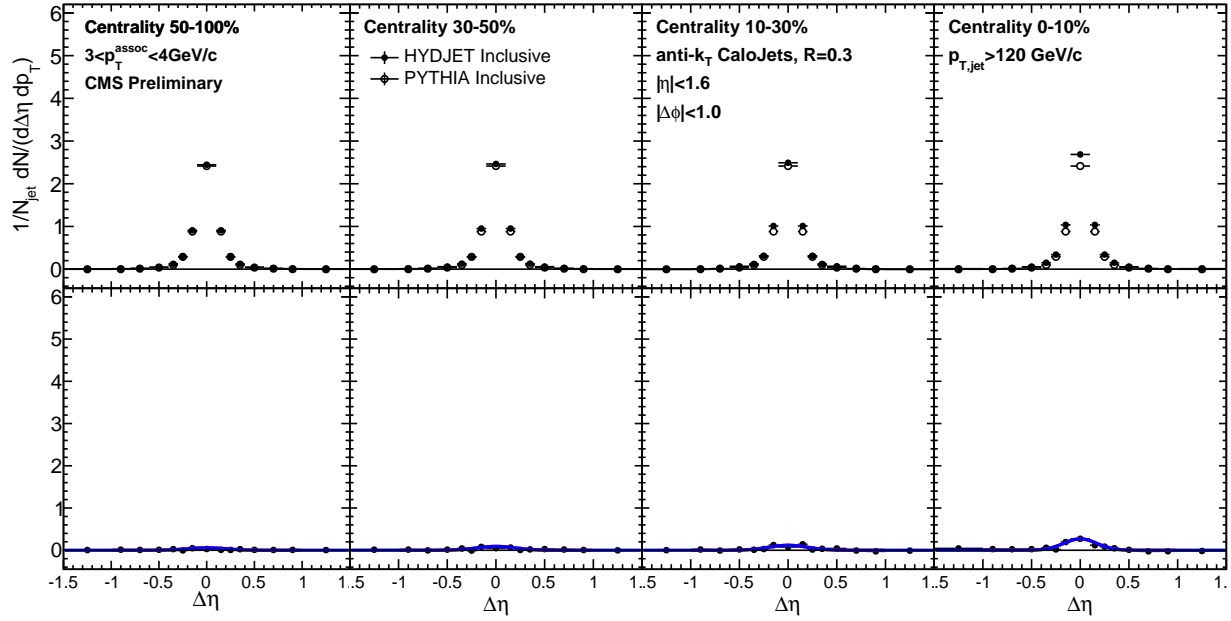


Figure 30.  $\Delta\eta$  background fluctuation bias correction for inclusive jets derived by constructing correlations in PYTHIA+HYDJET between reconstructed jets and only those tracks simulated as part of the heavy ion underlying event rather than the embedded PYTHIA hard process, for particles  $3 < p_T^{\text{trk}} < 4 \text{ GeV}$

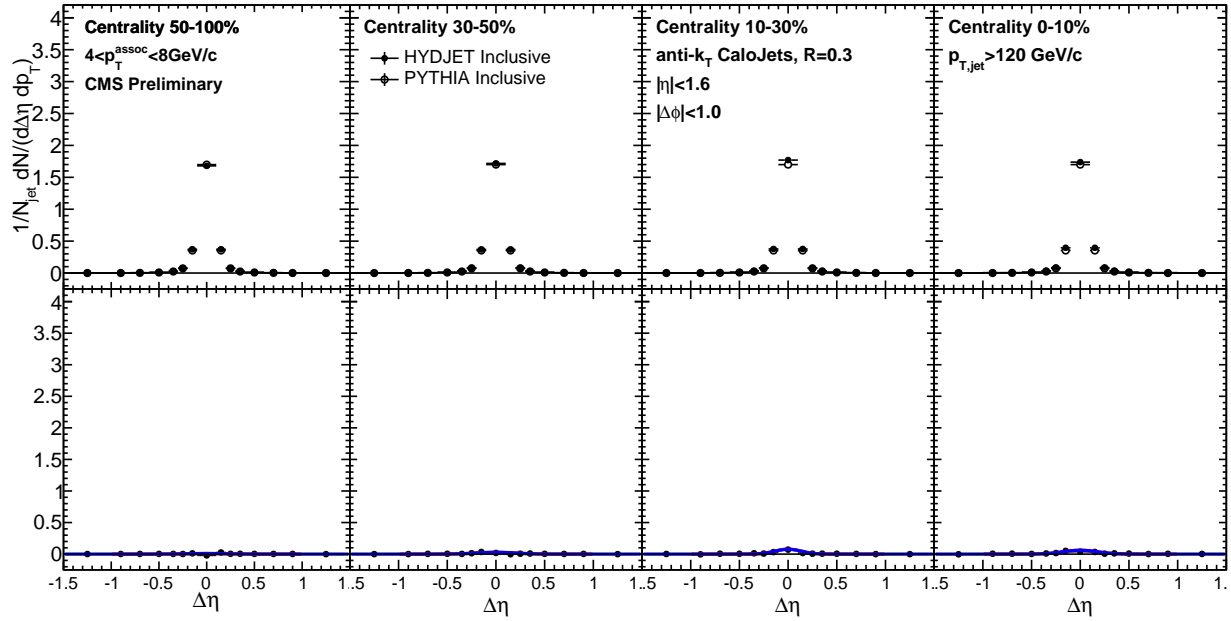


Figure 31.  $\Delta\eta$  background fluctuation bias correction for inclusive jets derived by constructing correlations in PYTHIA+HYDJET between reconstructed jets and only those tracks simulated as part of the heavy ion underlying event rather than the embedded PYTHIA hard process, for particles  $4 < p_T^{\text{trk}} < 8 \text{ GeV}$  and  $p_{T,\text{jet}} > 120 \text{ GeV}/c$

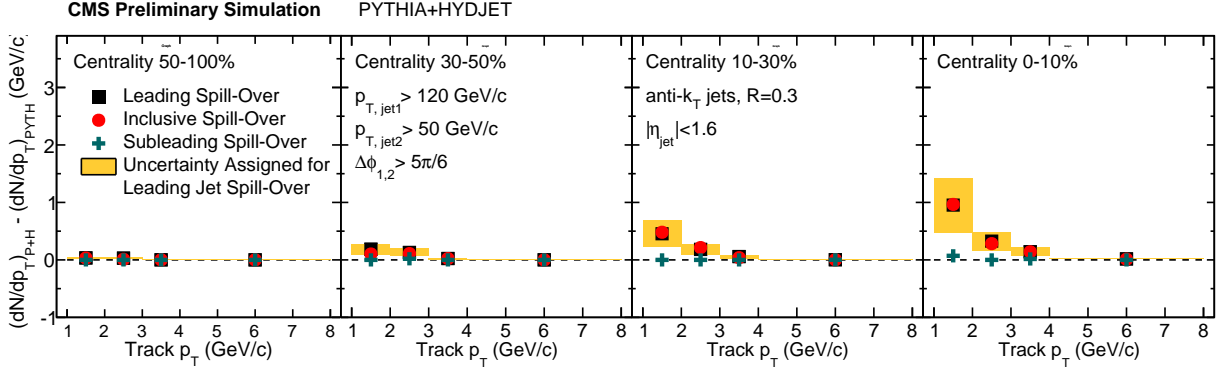


Figure 32. Integrated yield attributed to background fluctuation bias in the selection of inclusive and leading jets, shown as a function of associate track  $p_T$  for each centrality class.

is well-understood and that the HYDJET simulation used to derive it reproduces the background fluctuations in data closely enough to accurately obtain corrections. To check this, we extract a direct estimate of the effect from data using a “pseudo-embedding” of pp jets into a minimum bias PbPb data sample. The goal of this study is to verify that we recover a similar magnitude of excess yield as we attribute based on our more detailed PYTHIA+HYDJET simulations. Here we approximate the effect by adding the total transverse momentum in a circle of radius  $r = 0.3$  around all jets with  $p_T > 90$  GeV, and considering the total deviation up or down of this  $(\Sigma p_T)_{\text{cone}}$  from the average total transverse momentum  $\langle (\Sigma p_T)_{\text{cone}} \rangle$ . First, we may directly compare the average  $p_T$  and fluctuations in  $p_T$  in these random cones between data and Monte Carlo. We find that our Monte Carlo approximately reproduces the data: in data  $\langle (\Sigma p_T)_{\text{cone,data}} \rangle = 10.0$  GeV, with  $\sigma((\Sigma p_T)_{\text{cone,data}}) = 4.9$  GeV, while in Monte Carlo  $\langle (\Sigma p_T)_{\text{cone,MC}} \rangle = 11.9$  GeV, with  $\sigma((\Sigma p_T)_{\text{cone,data}}) = 5.6$  GeV.

We then use these random cones to adjust jet energy and re-select jets: we add the deviation up or down of this  $(\Sigma p_T)_{\text{cone}}$  to each embedded pp jets with this adjusted  $p_T$ . We then fill  $\Delta\eta - \Delta\phi$  correlations to all jets that pass our nominal  $p_T > 120$  GeV jet selection cut. We apply this technique to both our PYTHIA+HYDJET sample and a minimum-bias PbPb data sample to measure the charged particle yield associated with the embedded jet axis as a result of the jet fluctuation bias. As Fig. 33–34 show, this data pseudo-embedding recovers the same magnitude of excess yield due to background fluctuation bias as our nominal Monte Carlo studies, but artificially confines

1050 this effect to a  $r = 0.3$  cone due to the artificially simple jet reconstruction procedure. This gives  
 1051 confidence that the origin and magnitude of the effect are well-understood.

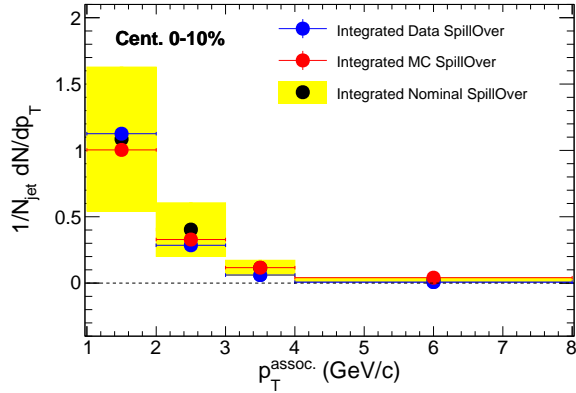


Figure 33. Total integrated magnitude of background fluctuation bias as simulated with pp jets embedded in Minimum Bias events (blue points) compared to the effect as simulated with PYTHIA jets into minimum bias HYDJET and to nominal corrections obtained with full PYTHIA+HYDJET simulation. Nominal systematic errors of  $\pm 50\%$  as assigned in this analysis are shown as yellow systematic error bars on nominal (full MC simulation) points.

1052 The background fluctuation bias could also be sensitive to the same calorimeter nonlinearity  
 1053 bias that necessitates fragmentation-jet energy corrections. To study this question and validate the  
 1054 uncertainty associated with this correction, we separately study the effect for quark jets and gluon  
 1055 jets, as shown in Figure 35. We find that this bias affects gluon jets slightly more than quark jets,  
 1056 consistent with deterioration of jet reconstruction performance for broader/softer jets, but that  
 1057 these deviations are within the 50% systematic uncertainty assigned.

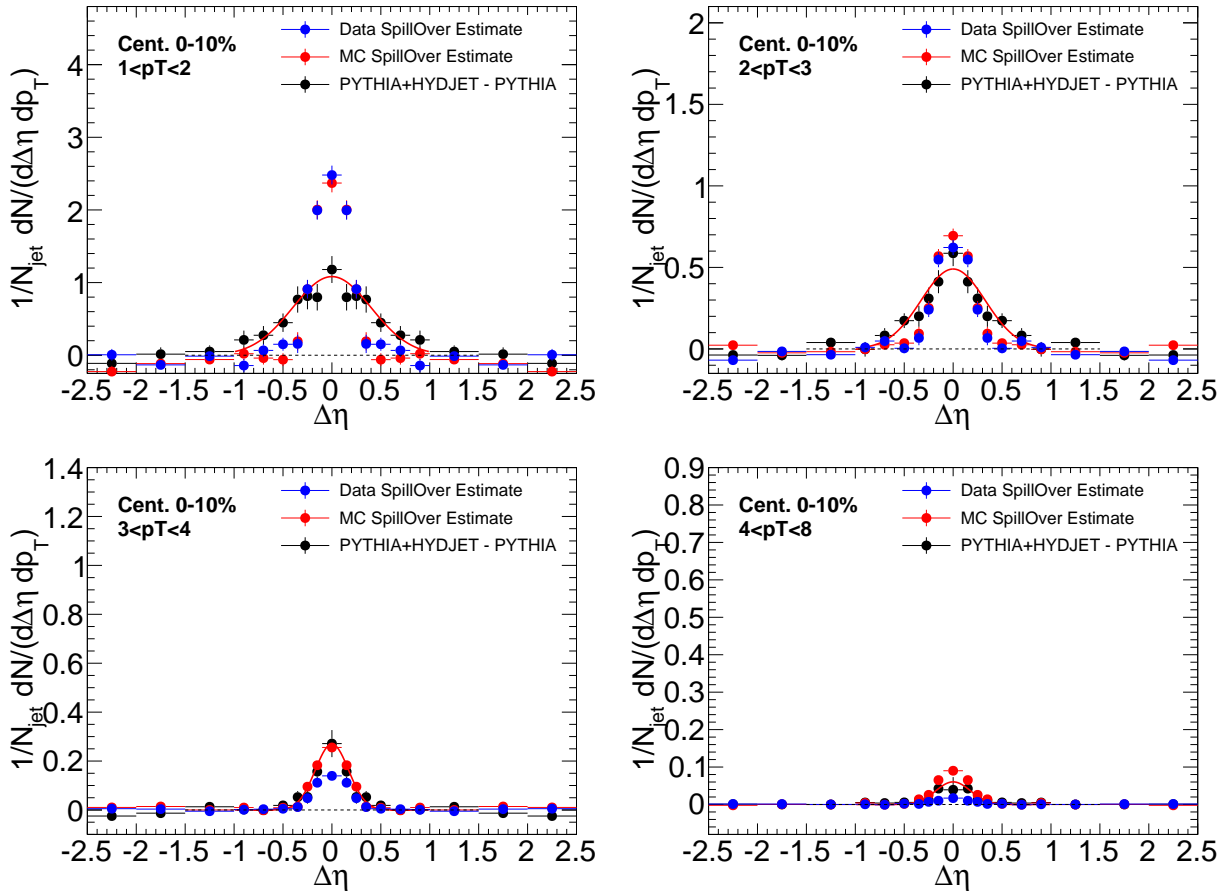


Figure 34. Correlated yield  $\Delta\eta$  due to background fluctuation bias as simulated with pp jets embedded in Minimum Bias events (blue points) compared to the effect applying the same technique with PYTHIA jets in HYDJET minimum bias events, as well as in full PYTHIA+HYDJET simulation (black points with red fit line).

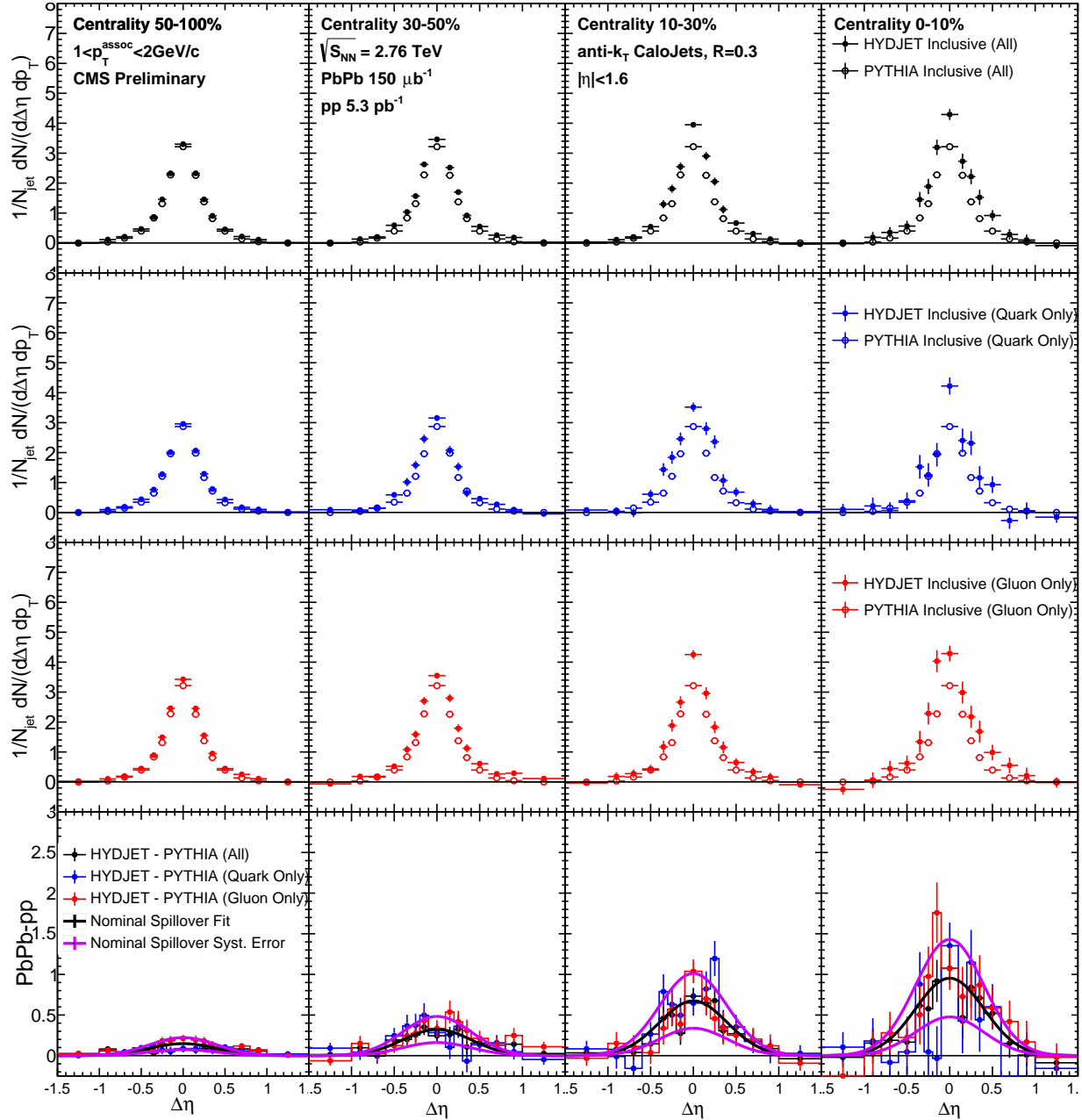


Figure 35. Comparison of magnitude of background selection bias effect for quark and gluon jets versus our nominal sample. Jet selection is inclusive in all cases.

1058 **9.6 Evaluation of systematic uncertainties**

1059 A number of sources of systematic uncertainty have been discussed in presenting jet and track  
1060 reconstruction and the jet-track correlation analysis procedure. To estimate the total systematic  
1061 uncertainty in these measurements, these contributions are added in quadrature. A brief summary  
1062 of all systematic uncertainty contributions, together with the procedure used to estimate their  
1063 magnitude follows. The contributions from each source (relative to jet peak signal) are summarized  
1064 in Tables V–VII.

1065 **9.6.1 Systematic uncertainties related to jet reconstruction**

1066 Jet reconstruction-related sources of systematic uncertainty in this analysis include the two recon-  
1067 struction biases as discussed above, as well uncertainty associated with the jet energy scale (JES)  
1068 evaluation. We consider three sources of uncertainty on the JES: (1) differences in calorimeter  
1069 response for quark versus gluon jets, meaning that medium-induced changes in jet flavor could  
1070 result in either over-correction or under-correction of jet energy and a resulting bias in jet selection  
1071 (evaluated via Monte Carlo non-closure for quark and gluon jets); (2) possible differences between  
1072 data and simulation; (3) uncertainty due to quenching effects not included in our HYDJET simula-  
1073 tion. To evaluate how each of these sources of JES uncertainty affects final correlations, we vary jet  
1074 selection threshold by the combined uncertainty, and then quantify the resulting differences in the  
1075 final correlations as a measure of the combined residual JES uncertainty. Since all the measured  
1076 correlations are studied per-reconstructed jets, the jet reconstruction efficiency does not contribute  
1077 to the systematic uncertainty of this measurement.

1078 **9.6.2 Systematic uncertainties related to tracking and tracking efficiency corrections**

1079 The tracking efficiency correction uncertainty is estimated from the ratio of corrected reconstructed  
1080 yields and generated yields by using generator level charged particles as a “truth” reference. To ac-  
1081 count for the possible track reconstruction differences in data and simulation, a residual uncertainty  
1082 in track reconstruction efficiency and fake rate corrections is also estimated.

1083 **9.6.3 Systematic uncertainty associated with pair acceptance correction and event  
1084 decomposition**

1085 Uncertainty arising from pair-acceptance effects is estimated by considering the sideband asymme-  
1086 try after dividing by the mixed-event background. Each sideband region of the final  $\Delta\eta$  distribution  
1087 ( $-2.5 < \Delta\eta < -1.5$  and  $1.5 < \Delta\eta < 2.5$ ) is separately fit with a horizontal line after background  
1088 subtraction. The greater of these two deviations from zero is assigned as systematic error. Un-  
1089 certainties resulting from the background subtraction are determined by considering the average  
1090 point-to-point deviation in two parts of the sideband region ( $1.5 < |\Delta\eta| < 2.0$  and  $2.0 < |\Delta\eta| < 2.5$ )  
1091 after background subtraction. The derivations of both of these sources of uncertainty are illustrated  
1092 in Appendix C. In PbPb data this background subtraction uncertainty is greatest for the most cen-  
1093 tral events (0–10%) and the lowest track  $p_T$  bin where the background is most significant compared  
1094 to the signal level, and decreases for less central collisions and for higher  $p_T$  tracks ( $p_T^{\text{trk}} > 2$  GeV).

1095 **9.6.4 Summary of systematic uncertainties**

1096 The contributions to total systematic uncertainty from each of the sources described above are given  
1097 in Tables V–VII. Table V gives uncertainty evaluations for correlation studies at 2.76 TeV, while  
1098 Table VI gives the same for studies at 5.02 TeV. Finally, Table VII gives uncertainty evaluations  
1099 for balanced ( $A_J < 0.22$ ) and unbalanced ( $A_J > 0.22$ ) dijet events in momentum balance studies  
1100 at 2.76 TeV.

TABLE V. Systematic uncertainties in the measurement of the jet-track correlations in PbPb and pp collisions at 2.76 TeV, as percentage of the total measured correlated yield. The numbers presented in this table summarize the range of values of systematic uncertainty (as a function of  $p_T^{\text{trk}}$ ) for different centrality bins.

Source	0–10%	10–30%	30–50%	50–100%	pp
Background fluctuation bias	3–12%	2–7%	1–5%	0–1%	–
Jet fragmentation function bias	0–2%	0–2%	0–2%	0–2%	0–2%
Residual jet energy scale	3%	3%	3%	3%	3%
Tracking efficiency uncertainty	4%	4%	4%	4%	3 %
Residual track efficiency corr.	5%	5%	5%	5%	5%
Pair acceptance corrections	5–9%	5–9%	4–8%	2–6%	2–3%
Background subtraction	2–5%	2–5%	2–5%	2–5%	1–2%
Total	9–17%	9–14%	8–13%	8–10%	7–8%

TABLE VI. Systematic uncertainties in the measurement of the jet track correlations in PbPb and pp collisions at 5.02 TeV. The numbers presented in this table summarize typical range of systematic uncertainty as a function of collision centrality. The upper limits of the cited values correspond to uncertainties at lowest  $p_T^{\text{trk}}$ , and uncertainties decrease with rising  $p_T^{\text{trk}}$ .

Source	0–10%	10–30%	30–50%	50–100%	ppRef
Background fluctuation bias	0–10%	0–5%	0–2%	0–1%	–
Background fluctuation bias residual	0–2%	0–3%	0–1%	0–1%	–
JFF bias	3–5%	3–4%	3–4%	3–4%	3%
Residual JES	4%	4%	4%	4%	4%
Tracking efficiency uncertainty	1%	1%	1%	1%	1%
Residual tracking efficiency	5%	5%	5%	5%	5%
Pair-acceptance corrections	1–5%	1–4%	1–4%	1–4%	1–2%
Event decomposition	1–9%	0–4%	0–4%	0–3%	0–3%
Total	7–16%	7–11%	7–9%	7–9%	7–8%

TABLE VII. This table summarizes the systematic uncertainties in the measurement of the  $p_T^{\text{trk}}$  correlations in PbPb and pp collisions at 2.76 TeV. Upper and lower limits are shown as a function of collision centrality. Upper values correspond to the uncertainties at lowest  $p_T^{\text{trk}}$ .

Source	0–30%	30–50%	50–100%	pp
Balanced jet selection ( $A_J < 0.22$ ):				
Background fluctuations	1–8%	1–3%	0–1%	–
JFF bias and jet swapping	0–2%	0–2%	0–2%	0–2%
Residual JES	3%	3%	3%	3%
Tracking efficiency	4%	4%	4%	3 %
Residual track efficiency corr.	5%	5%	5%	5%
Pair acceptance corrections	5–9%	4–8%	2–6%	2–3%
Event decomposition	2–5%	2–5%	2–5%	1–2%
Total	9–15%	8–13%	8–10%	7–8%
Unbalanced jet selection ( $A_J > 0.22$ ):				
Background fluctuations	1–10%	1–5%	0–2%	–
JFF bias and jet swapping	0–2%	0–2%	0–2%	0–2%
Residual JES	3%	3%	3%	3%
Tracking efficiency	4%	4%	4%	3 %
Residual track efficiency corr.	5%	5%	5%	5%
Pair acceptance corrections	5–9%	4–8%	2–6%	2–3%
Event decomposition	2–5%	2–5%	2–5%	1–2%
Total	9–16%	8–13%	8–10%	7–8%

1101

## 10 DISCUSSION OF RESULTS

1102 Jet-track correlation studies can produce measurements the density of particles (in each  $p_T^{\text{trk}}$  class)  
 1103 with respect to the jet axis and can also, by creating correlations weighted per-track by its  $p_T^{\text{trk}}$ , pro-  
 1104 duce measurements of the distribution of  $p_T^{\text{trk}}$  in the event as a whole. Both types of measurements  
 1105 are presented here, for inclusive selections of jets with  $p_T > 120$  GeV and for high- $p_T$  dijet events at  
 1106 2.76 TeV and 5.02 TeV. First, particle density correlation results are presented in Secs. 10.1- 10.2.  
 1107 Next,  $p_T^{\text{trk}}$  distributions are used to extract measurements of jet shapes (the transverse momentum  
 1108 profiles of jets) in Sec. 10.3. Finally, in Sec. 10.4,  $p_T^{\text{trk}}$  distributions are used to decompose and  
 1109 analyze the hemisphere momentum balance in dijet events.

### 1110 10.1 Inclusive jet particle density correlation results

1111 Particle density correlation studies allow for the detailed characterization of jet fragmentation,  
 1112 and of medium-induced modifications to jet fragmentation in PbPb data (as a function of collision  
 1113 centrality) compared to pp data. The analysis procedure described in Sec. 9 results in fully-corrected  
 1114 2D jet peaks in  $\Delta\eta - \Delta\phi$ , which may then be projected to obtain the distribution of particles in  
 1115 each  $p_T^{\text{trk}}$  class as a function of  $\Delta\eta$  and  $\Delta\phi$ . The top panels of Figs. 36-43 show these  $\Delta\eta$  and  
 1116  $\Delta\phi$  distributions (projected over  $|\Delta\phi| < 1$  and  $|\Delta\eta| < 1$ , respectively) for 2.76 TeV pp data and  
 1117 PbPb data in each  $p_T^{\text{trk}}$  range from 1–2 GeV (Fig. 36-37) up to 4–8 GeV (Fig. 42-43). The bottom  
 1118 panels of these figures show the differences PbPb–pp for illustration of medium modifications to jet  
 1119 fragmentation patterns. In both the  $\Delta\eta$  and  $\Delta\phi$  dimensions, centrality-dependent excesses of soft  
 1120 (low- $p_T^{\text{trk}}$ ) particles are evident. These exhibit the greatest modifications in the most central PbPb  
 1121 collisions, decreasing with centrality until the most peripheral collisions show little modification  
 1122 when compared to pp data. These excesses decrease with increasing  $p_T^{\text{trk}}$ , until in the 4–8 GeV  
 1123 range the enhancements evident at lowest- $p_T^{\text{trk}}$  reverse to possible slight depletion. In both  $\Delta\eta$  and  
 1124  $\Delta\phi$  dimensions, the soft excesses exhibit a gaussian-like distribution around the jet axis, while also  
 1125 extending to large angles  $\Delta\eta = 1$  and  $\Delta\phi = 1$  at lowest  $p_T^{\text{trk}}$ .

1126 Figures 44 and 45 show the corresponding  $\Delta\eta$  and  $\Delta\phi$  distributions at 5.02 TeV. Here,  
 1127 the distribution of particles in each  $p_T^{\text{trk}}$  class are stacked (with lowest- $p_T^{\text{trk}}$  particles on top), and  
 1128 pp data shown separately at left. Again the differences PbPb–pp are shown in bottom panels to

illustrate the medium modifications, and exhibit similar qualitative trends to those described above  
 for 2.76 TeV results. Results may also be presented as a function of radial distance from the jet axis  
 $\Delta r = \sqrt{\Delta\eta^2 + \Delta\phi^2}$ . Figure 46 presents charged particle yields, differentially in  $p_T^{\text{trk}}$ , as a function  
 of  $\Delta r$ . For comparison, the bottom row of each plot shows the difference, PbPb minus pp. This  
 shows the particles contributing to a jet fragmentation function measurement within a given radius  
 from a jet, and illustrates the radial dependence of modifications extending to at least  $\Delta r = 1$ .

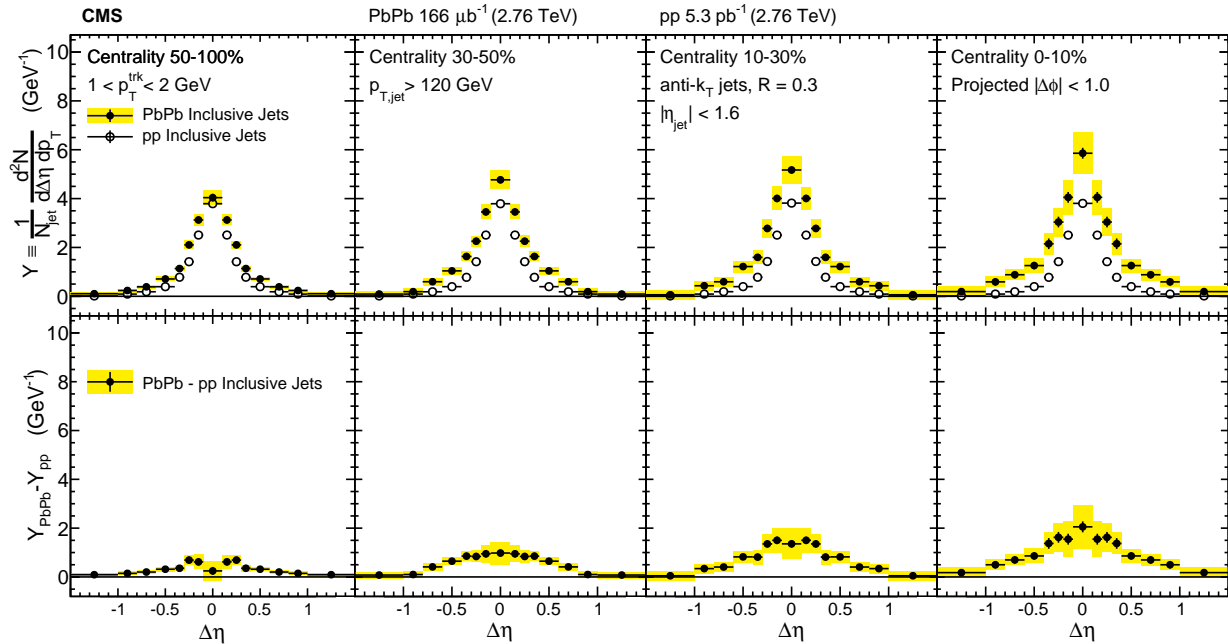


Figure 36. Symmetrized  $\Delta\eta$  distributions (projected over  $|\Delta\phi| < 1$ ) of background-subtracted particle yields correlated to PbPb and pp inclusive jets with  $p_T > 120$  GeV are shown in the top panels for tracks with  $1 < p_T^{\text{trk}} < 2$  GeV. The difference in PbPb and pp per-jet yields is shown in the bottom panels. The total systematic uncertainties are shown as shaded boxes, and statistical uncertainties are shown as vertical bars (often smaller than the symbol size).

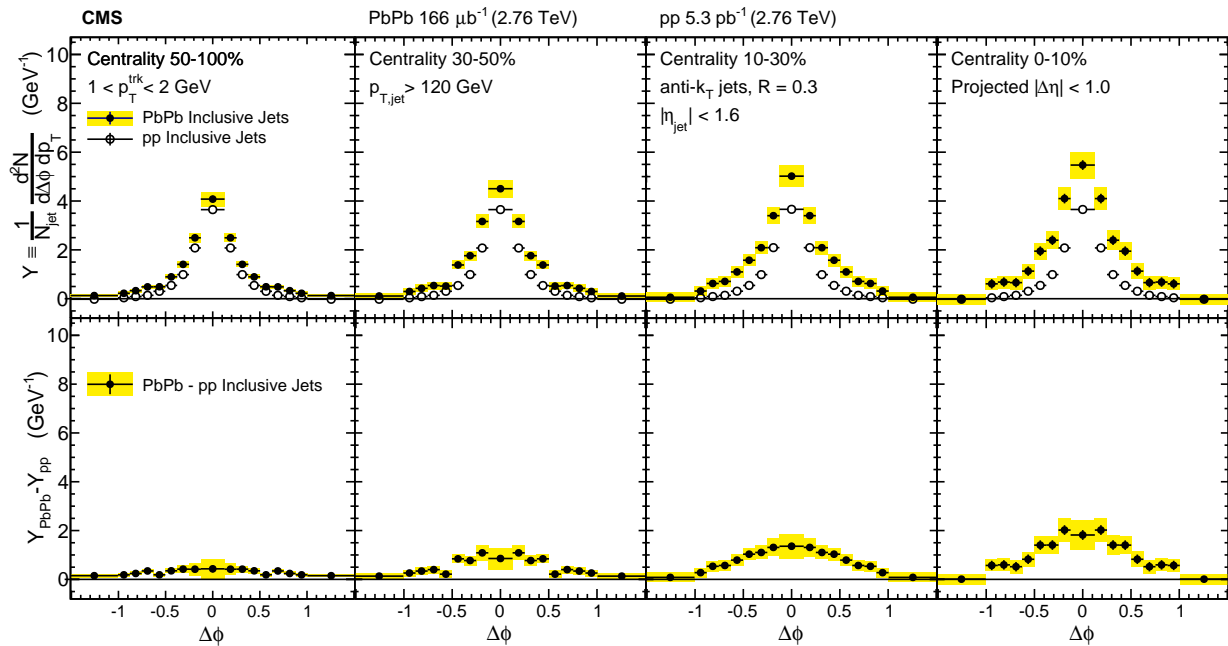


Figure 37. Symmetrized  $\Delta\phi$  distributions (projected over  $|\Delta\eta| < 1$ ) of background-subtracted particle yields correlated to PbPb and pp inclusive jets with  $p_{\text{T}} > 120 \text{ GeV}$  are shown in the top panels for tracks with  $1 < p_{\text{T}}^{\text{trk}} < 2 \text{ GeV}$ . The difference in PbPb and pp per-jet yields is shown in the bottom panels. The total systematic uncertainties are shown as shaded boxes, and statistical uncertainties are shown as vertical bars (often smaller than the symbol size).

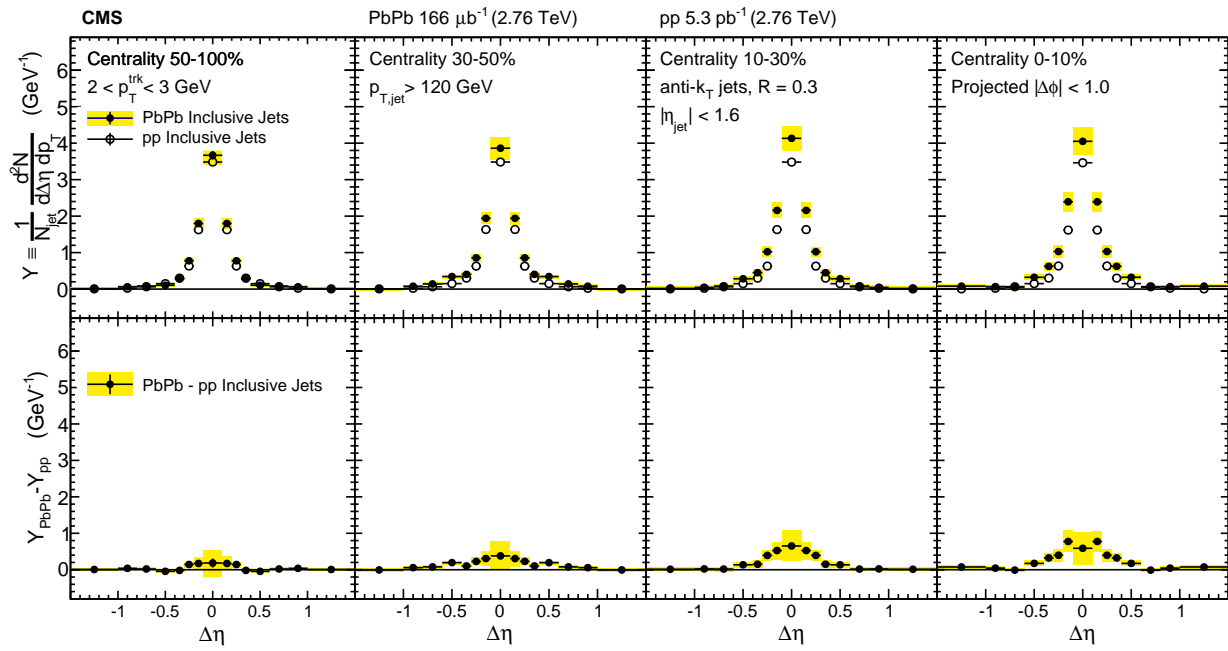


Figure 38. Symmetrized  $\Delta\eta$  distributions (projected over  $|\Delta\phi| < 1$ ) of background-subtracted particle yields correlated to PbPb and pp inclusive jets with  $p_T > 120$  GeV are shown in the top panels for tracks with  $2 < p_T^{\text{trk}} < 3$  GeV. The difference in PbPb and pp per-jet yields is shown in the bottom panels. The total systematic uncertainties are shown as shaded boxes, and statistical uncertainties are shown as vertical bars (often smaller than the symbol size).

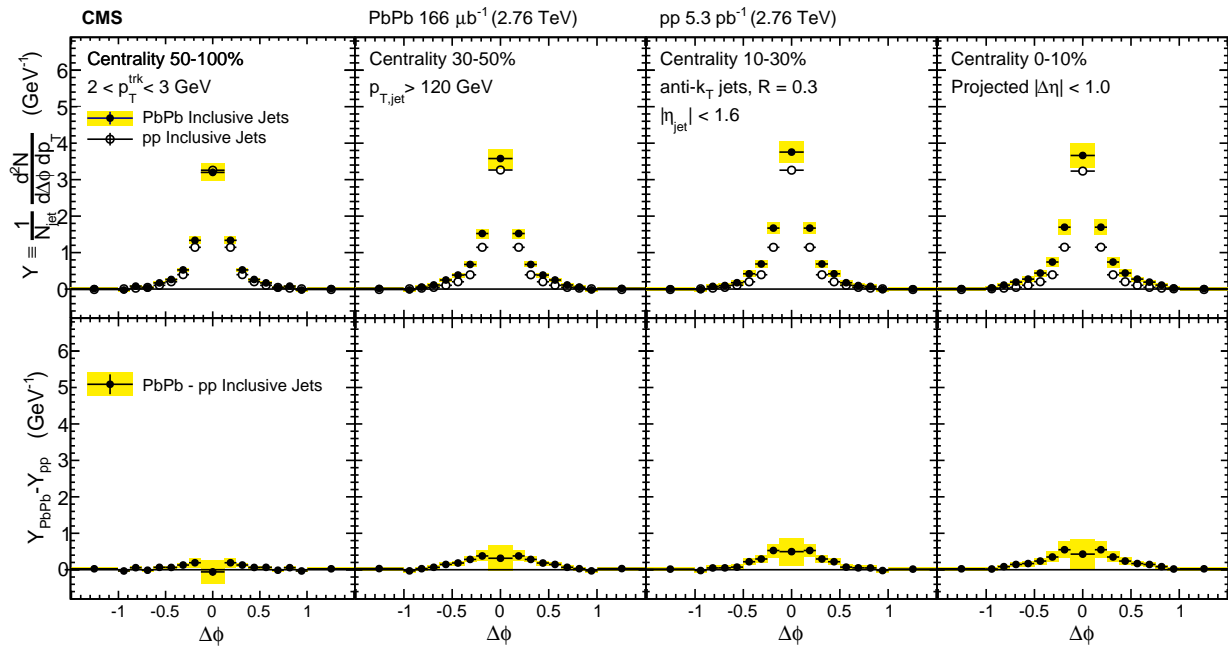


Figure 39. Symmetrized  $\Delta\phi$  distributions (projected over  $|\Delta\eta| < 1$ ) of background-subtracted particle yields correlated to PbPb and pp inclusive jets with  $p_T > 120$  GeV are shown in the top panels for tracks with  $2 < p_T^{\text{trk}} < 3$  GeV. The difference in PbPb and pp per-jet yields is shown in the bottom panels. The total systematic uncertainties are shown as shaded boxes, and statistical uncertainties are shown as vertical bars (often smaller than the symbol size).

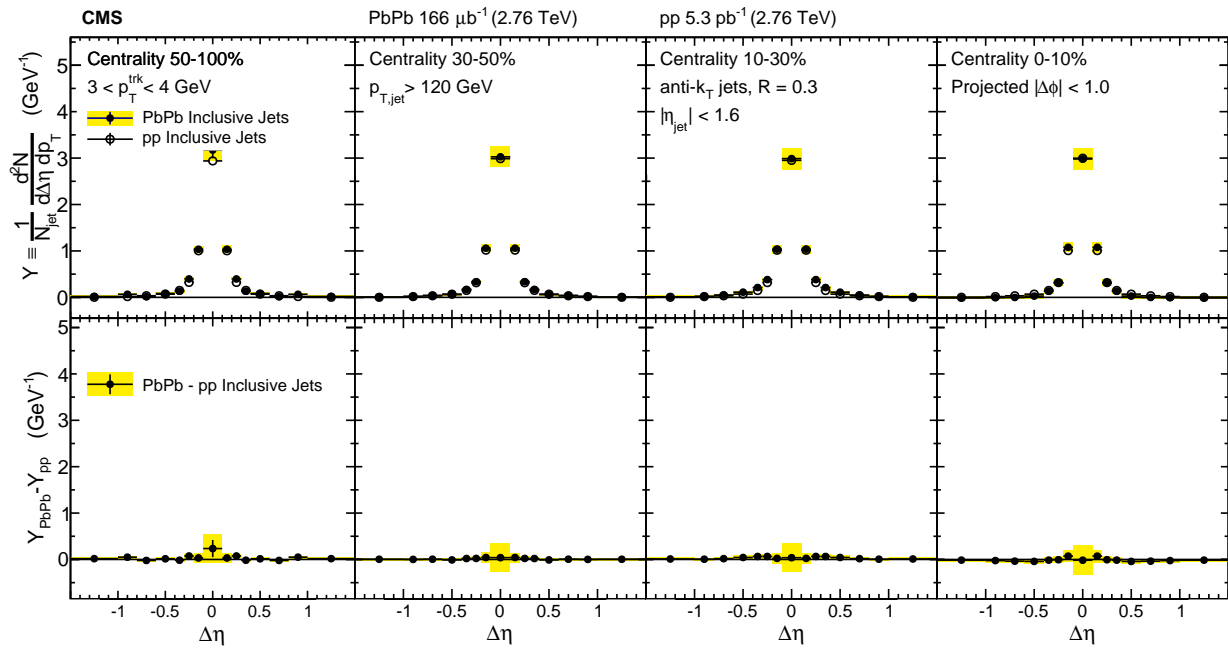


Figure 40. Symmetrized  $\Delta\eta$  distributions (projected over  $|\Delta\phi| < 1$ ) of background-subtracted particle yields correlated to PbPb and pp inclusive jets with  $p_{\text{T}} > 120 \text{ GeV}$  are shown in the top panels for tracks with  $3 < p_{\text{T}}^{\text{trk}} < 4 \text{ GeV}$ . The difference in PbPb and pp per-jet yields is shown in the bottom panels. The total systematic uncertainties are shown as shaded boxes, and statistical uncertainties are shown as vertical bars (often smaller than the symbol size).

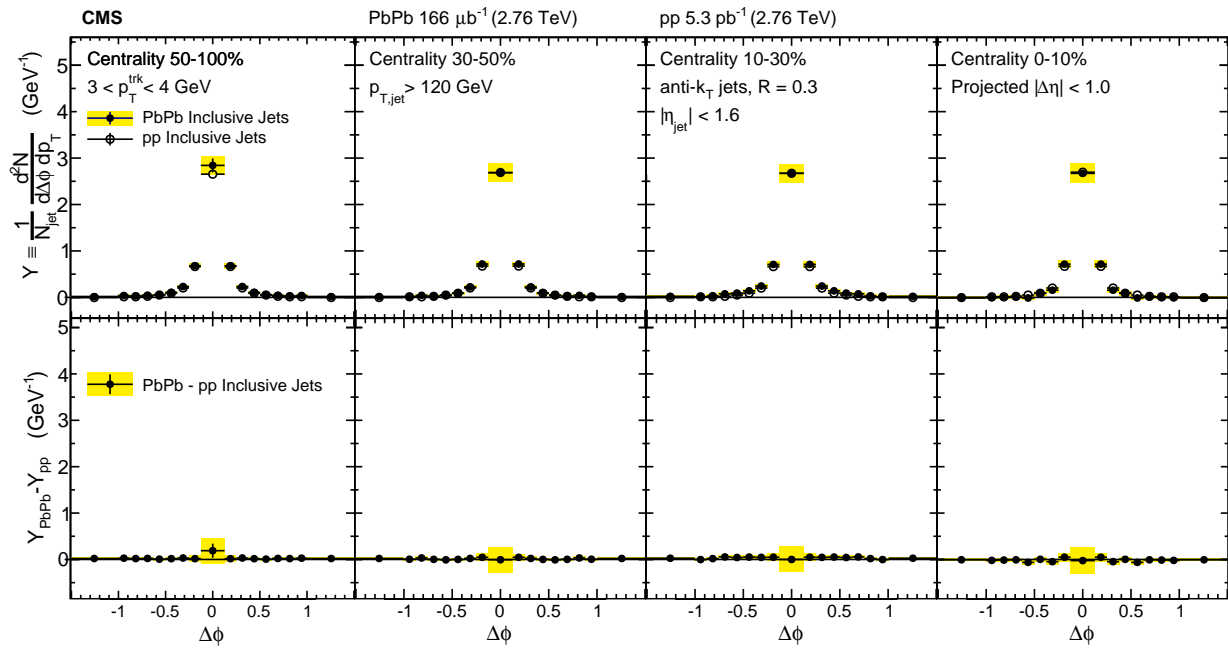


Figure 41. Symmetrized  $\Delta\phi$  distributions (projected over  $|\Delta\eta| < 1$ ) of background-subtracted particle yields correlated to PbPb and pp inclusive jets with  $p_T > 120 \text{ GeV}$  are shown in the top panels for tracks with  $3 < p_T^{\text{trk}} < 4 \text{ GeV}$ . The difference in PbPb and pp per-jet yields is shown in the bottom panels. The total systematic uncertainties are shown as shaded boxes, and statistical uncertainties are shown as vertical bars (often smaller than the symbol size).

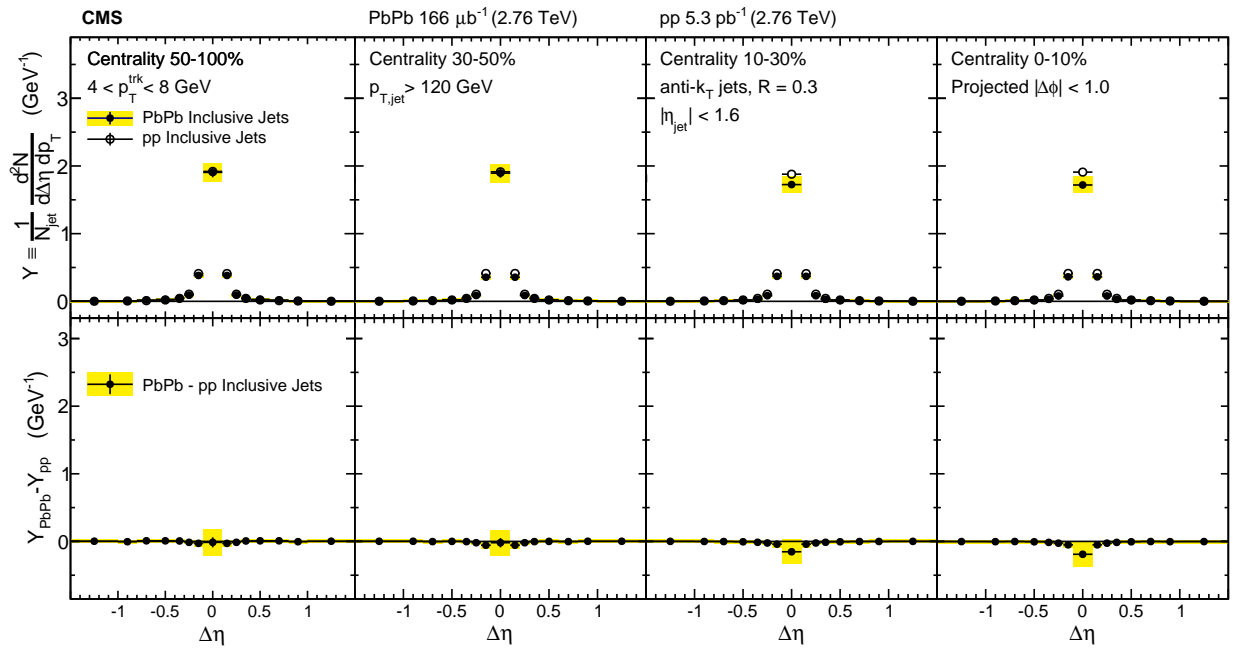


Figure 42. Symmetrized  $\Delta\eta$  distributions (projected over  $|\Delta\phi| < 1$ ) of background-subtracted particle yields correlated to PbPb and pp inclusive jets with  $p_T > 120 \text{ GeV}$  are shown in the top panels for tracks with  $4 < p_T^{\text{trk}} < 8 \text{ GeV}$ . The difference in PbPb and pp per-jet yields is shown in the bottom panels. The total systematic uncertainties are shown as shaded boxes, and statistical uncertainties are shown as vertical bars (often smaller than the symbol size).

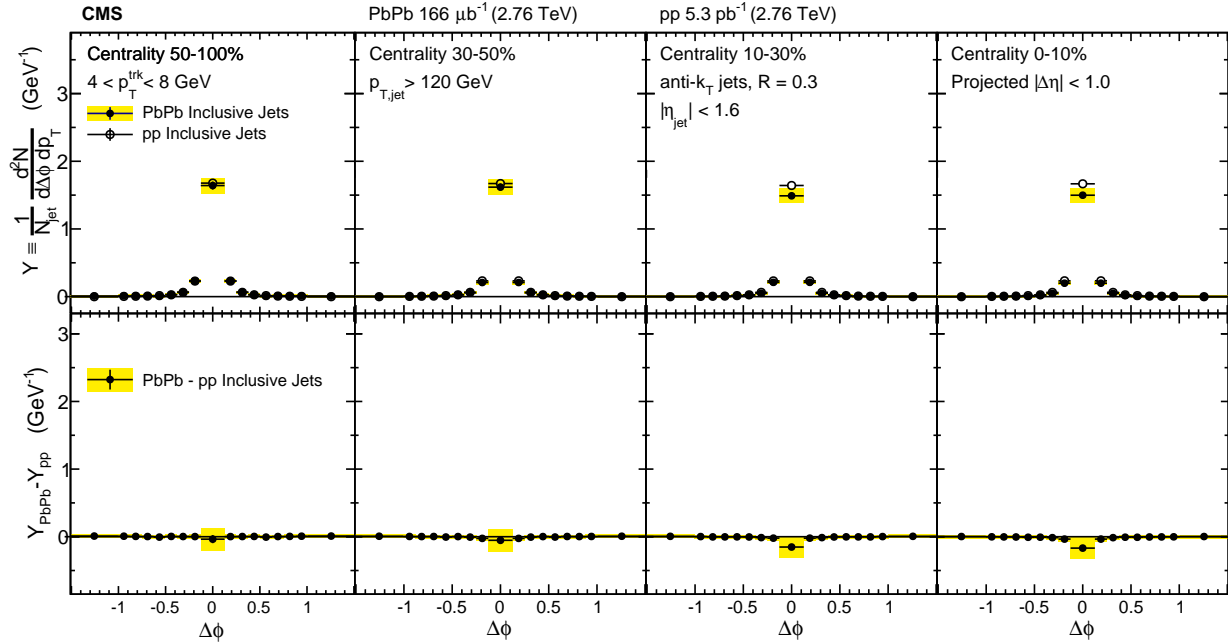


Figure 43. Symmetrized  $\Delta\phi$  distributions (projected over  $|\Delta\eta| < 1$ ) of background-subtracted particle yields correlated to PbPb and pp inclusive jets with  $p_T > 120$  GeV are shown in the top panels for tracks with  $4 < p_T^{\text{trk}} < 8$  GeV. The difference in PbPb and pp per-jet yields is shown in the bottom panels. The total systematic uncertainties are shown as shaded boxes, and statistical uncertainties are shown as vertical bars (often smaller than the symbol size).

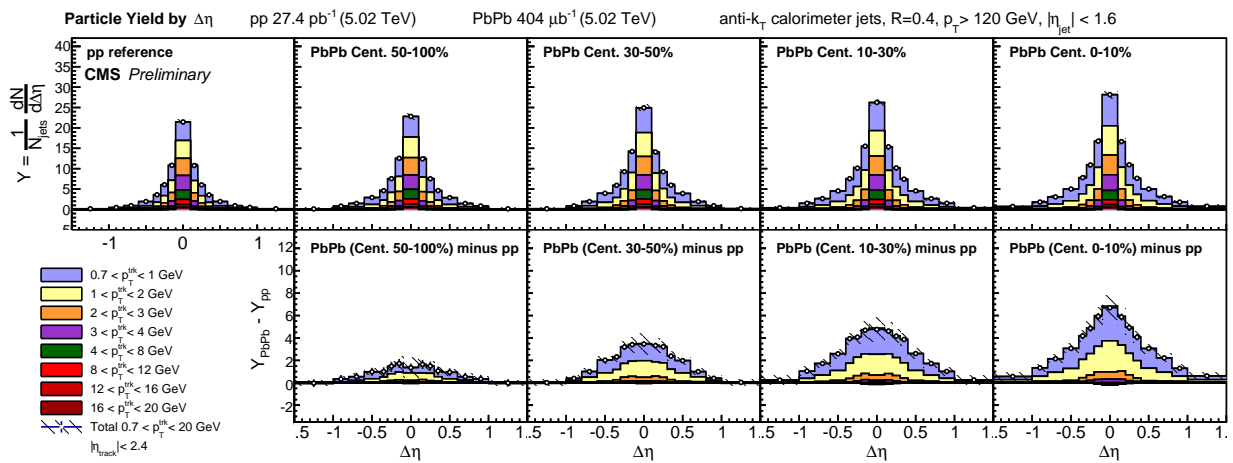


Figure 44. Top row: distributions of charged particle yields correlated to jets with  $p_T > 120$  GeV as a function of  $\Delta\eta$  (projected over  $|\Delta\phi| < 1$ ), shown differentially for all  $p_T^{\text{trk}}$  bins for pp, peripheral PbPb, and central PbPb data. Bottom row: PbPb minus pp difference in these distributions. Hatched lines on  $p_T^{\text{trk}}$ -inclusive points show total systematic uncertainties.

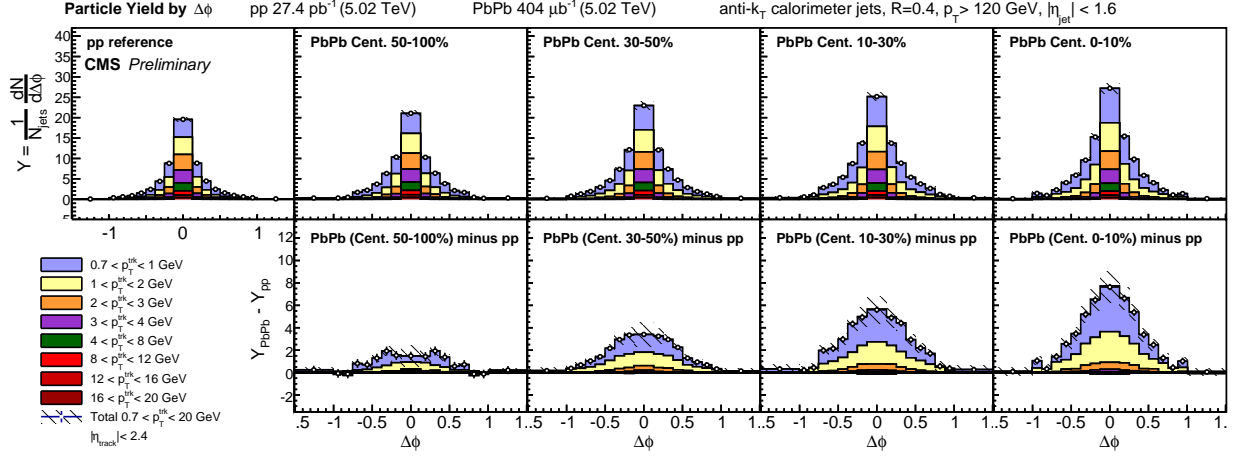


Figure 45. Top row: distributions of charged particle yields correlated to jets with  $p_T > 120 \text{ GeV}$  as a function of  $\Delta\phi$  (projected over  $|\Delta\eta| < 1$ ), shown differentially for all  $p_T^{\text{trk}}$  bins for pp, peripheral PbPb, and central PbPb data. Bottom row: PbPb minus pp difference in these distributions. Hatched lines on  $p_T^{\text{trk}}$ -inclusive points show total systematic uncertainties.

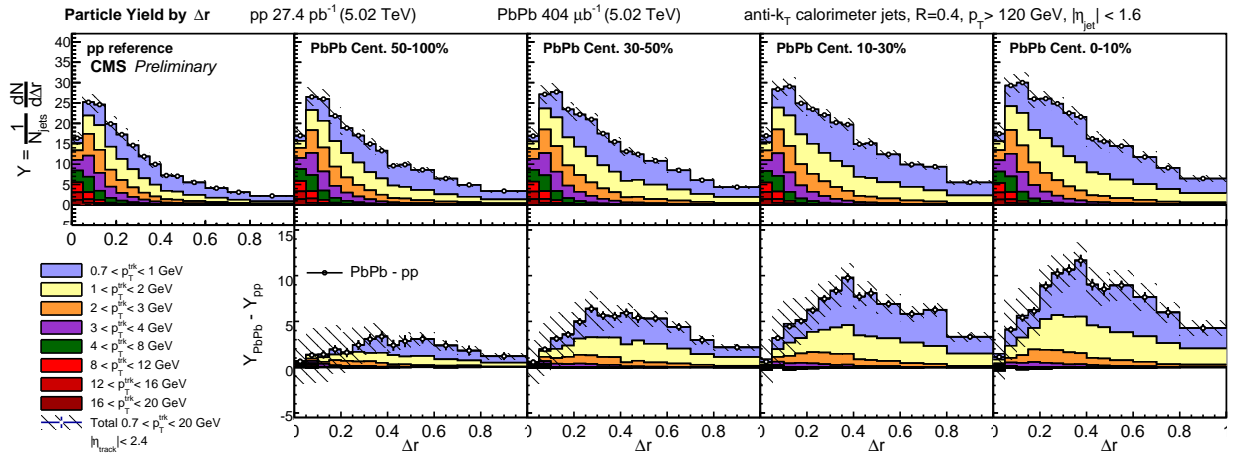


Figure 46. Top row: distributions of charged particle yields correlated to jets with  $p_T > 120 \text{ GeV}$  as a function of  $\Delta r$ , shown differentially for all  $p_T^{\text{trk}}$  bins. Bottom row: PbPb minus pp difference in these distributions. Hatched lines on  $p_T^{\text{trk}}$ -inclusive points show total systematic uncertainties.

To summarize the magnitude of the modifications to particle yields in PbPb relative to pp collisions, integrated yields as a function of  $p_T^{\text{trk}}$  are presented in the top panel of Fig. 47. The bottom panel of Fig. 47 shows differences PbPb–pp in total integrated particle yields in each  $p_T^{\text{trk}}$  class for results at 5.02 TeV compared to 2.76 TeV results. This quantifies the low- $p_T$  excess in central PbPb collisions to as many as 4 additional particles (in central PbPb relative to pp reference) per unit of  $p_T^{\text{trk}}$  in the lowest  $p_T^{\text{trk}}$  bin. This excess decreases smoothly with  $p_T^{\text{trk}}$  in each centrality bin, until the 4–8 GeV central PbPb bin is consistent with or slightly depleted relative to pp reference. For tracks with  $p_T^{\text{trk}} > 8$  GeV, there is no evident modification in PbPb compared to pp. Excess yields do not exhibit significant dependence on collision energies; particle yields at low- $p_T^{\text{trk}}$  are consistently larger at 5.02 TeV than at 2.76 TeV, but within the systematic uncertainties of the two measurements.

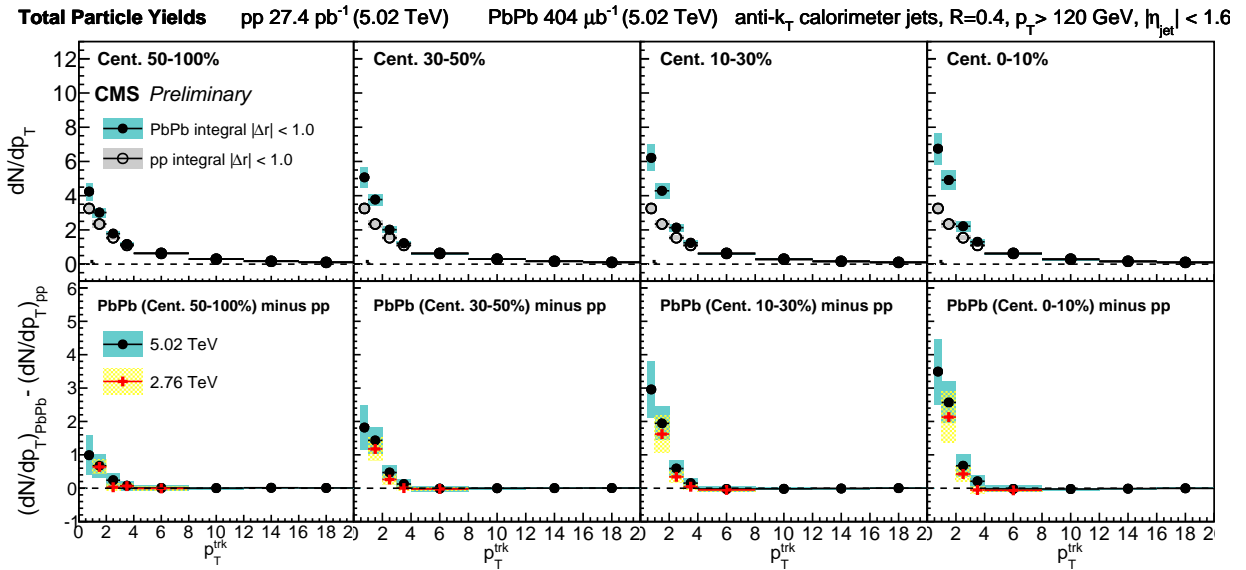


Figure 47. Top row: integrated yields of charged particle yields correlated to jets with  $p_T > 120$  GeV as a function of  $p_T^{\text{trk}}$  bins for PbPb data, compared to pp reference. Bottom row: integrated excess yield, PbPb minus pp. New measurements of excess yields at 5.02 TeV are compared to those measured at 2.76 TeV.

1146 **10.2 Dijet correlation results**

1147 In the studies of charged-particle yields correlated to an inclusive sample of jets with  $p_T > 120$   
1148 GeV presented above, jet quenching is evident in the redistribution of  $p_T^{\text{trk}}$  from harder to softer  
1149 particles, and particularly in the observed centrality-dependent excess of low- $p_T^{\text{trk}}$  particle yields. Jet  
1150 quenching effects may be further probed by considering charged-particle yields correlated to each  
1151 jet axis in dijet events. Requiring events with two back-to-back jets (leading jet  $p_{T,1} > 120$  GeV,  
1152 subleading jet  $p_{T,2} > 50$  GeV,  $\Delta\phi_{1,2} > \frac{5\pi}{6}$ ), we construct separate correlations to the leading and  
1153 the subleading jet axes. In pp data, most dijets are balanced while in central PbPb a greater fraction  
1154 of dijet pairs are unbalanced (as discussed in Sec. 8.4), suggesting that central PbPb data contains  
1155 a significant fraction of dijet pairs in which the highest- and second-highest- $p_T$  hard-scattering  
1156 products had similar transverse momenta, but in which one jet experienced a greater path-length  
1157 through the medium and correspondingly greater quenching. This is expected to correspond to a  
1158 “surface-bias” toward leading jets with very short path-lengths through the medium, that might be  
1159 expected to correspond to minimal quenching in the leading jet sample. It is therefore interesting  
1160 to separately compare charged-particle distributions with respect to the leading and subleading jet  
1161 axes in PbPb and pp data to look for evidence of path-length dependence in jet quenching.

1162 Figures 48 and 49 show these correlation patterns in  $\Delta\eta$  and  $\Delta\phi$ , respectively, for the  
1163  $1 < p_T^{\text{trk}}$  GeV range in which the greatest quenching was evident in the 2.76 TeV inclusive jet  
1164 studies. As expected, quenching effects are greater for subleading than leading jets, as evident in  
1165 larger excesses of soft particles in subleading jet correlations (while retaining the same centrality  
1166 trends and gaussian-like distributions observed for the inclusive jet sample). However, leading jets  
1167 exhibit evidence of quenching as well, showing similar soft-particle excesses to those observed in  
1168 the inclusive sample. To quantitatively compare subleading and leading jet modifications to those  
1169 in the inclusive jet sample, Fig. 50 shows integrated particle yields for all three jet samples at 2.76  
1170 TeV. Here it is clear that leading jets show similar PbPb–pp modifications to those observed in the  
1171 inclusive sample, with approximately 2 excess particles in PbPb compared to pp data at lowest- $p_T^{\text{trk}}$ ,  
1172 while the subleading jet sample shows as many as 4 excess particles in PbPb compared to pp data  
1173 at lowest- $p_T^{\text{trk}}$ .

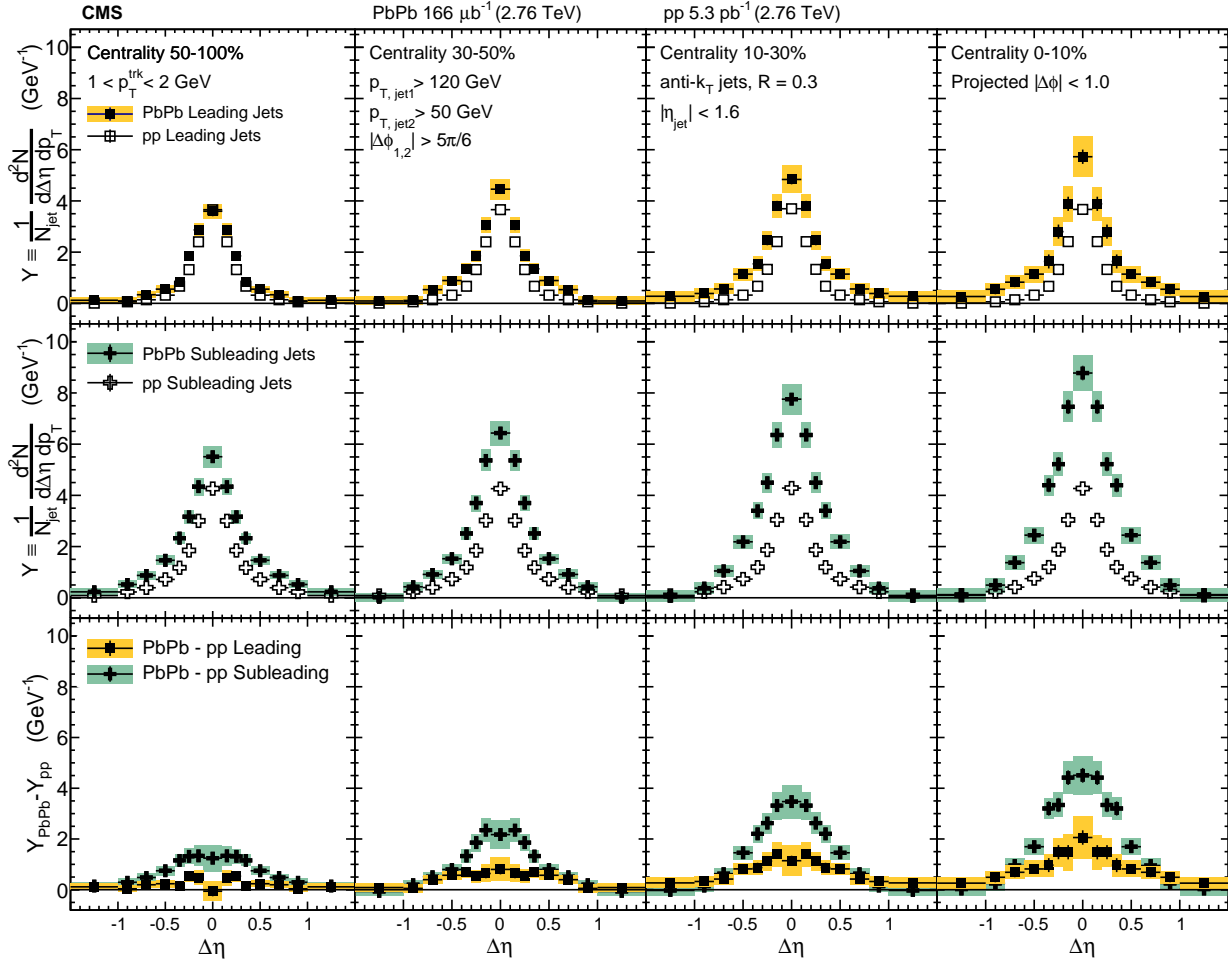


Figure 48. The top panels show the  $\Delta\eta$  distributions (projected over  $|\Delta\phi| < 1$ ) of charged-particle background-subtracted yields correlated to PbPb and pp leading jets with  $p_{T,\text{jet}1} > 120$  GeV. The middle panels show the same distributions for subleading jets with  $p_{T,\text{jet}2} > 50$  GeV, and the bottom panels show the difference PbPb minus pp for both leading and subleading jets. The total systematic uncertainties are shown as shaded boxes, and statistical uncertainties are shown as vertical bars (often smaller than the symbol size).

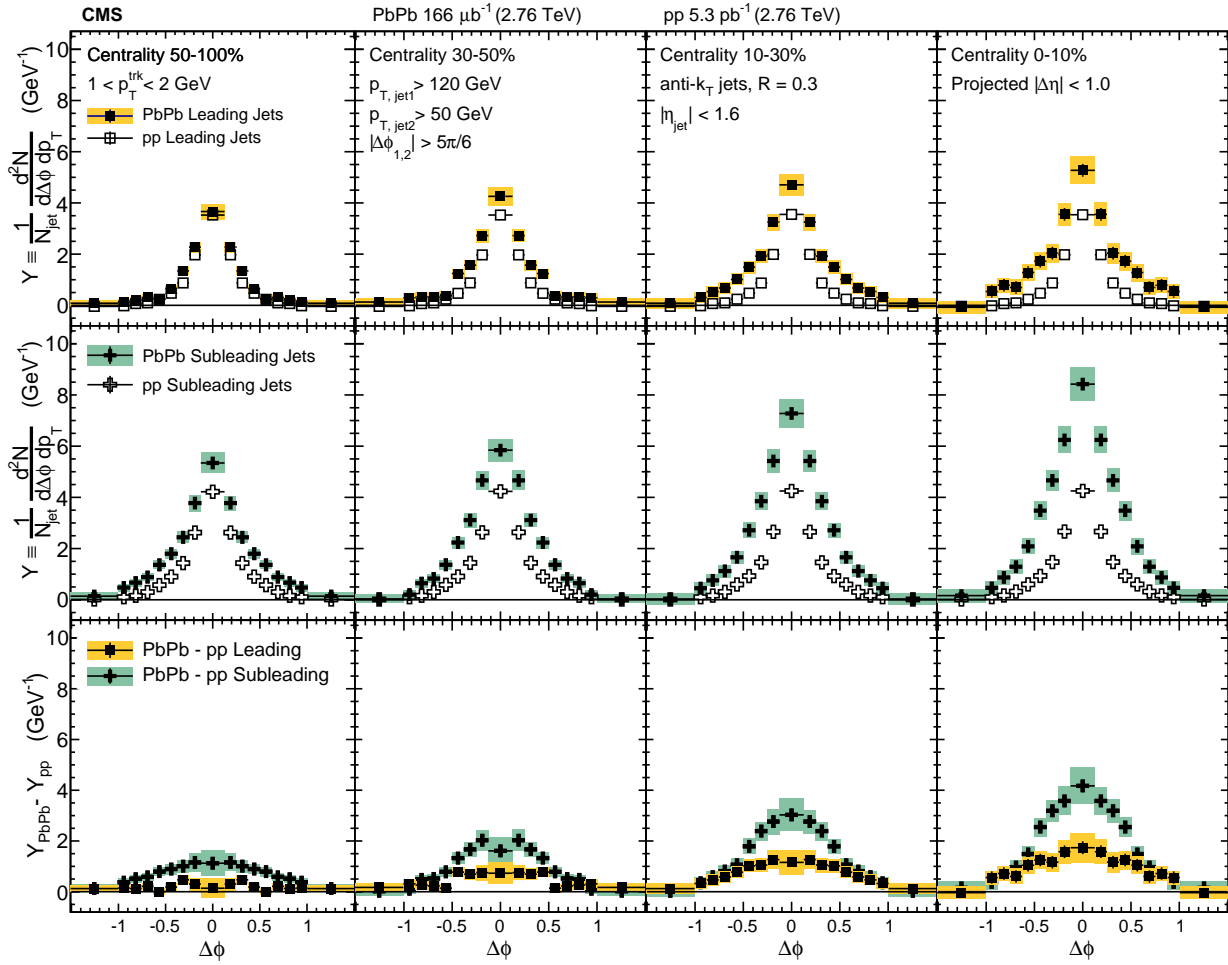


Figure 49. The top panels show the  $\Delta\phi$  distributions (projected over  $|\Delta\eta| < 1$ ) of charged-particle background-subtracted yields correlated to PbPb and pp leading jets with  $p_{T,\text{jet}1} > 120$  GeV. The middle panels show the same distributions for subleading jets with  $p_{T,\text{jet}2} > 50$  GeV, and the bottom panels show the difference PbPb minus pp for both leading and subleading jets. The total systematic uncertainties are shown as shaded boxes, and statistical uncertainties are shown as vertical bars (often smaller than the symbol size).

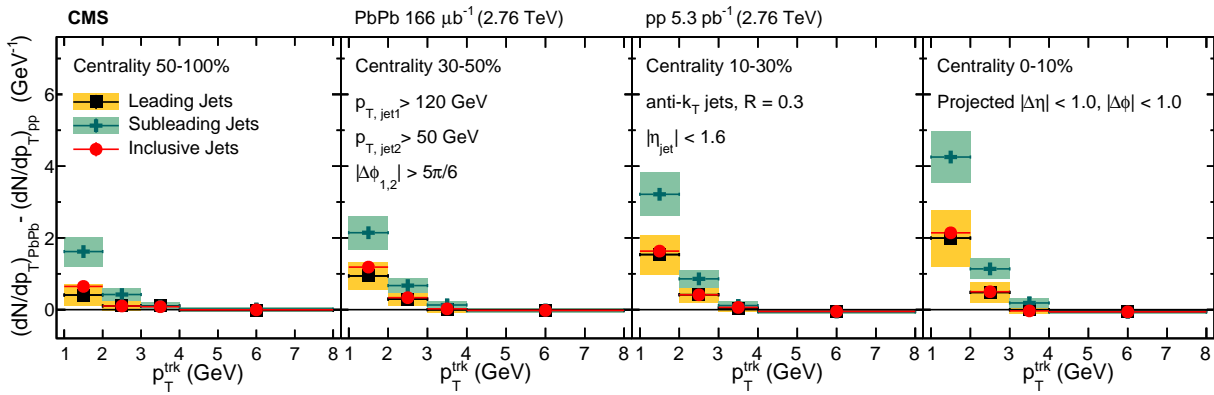


Figure 50. Total excess correlated yield observed in the PbPb data with respect to the reference measured in pp collisions, shown as a function of track  $p_T$  in four different centrality intervals (0–10%, 10–30%, 30–50%, 50–100%) for both leading jets with  $p_{T,\text{jet}1} > 120$  GeV and subleading jets with  $p_{T,\text{jet}2} > 50$  GeV. The total systematic uncertainties are shown as shaded boxes, and statistical uncertainties are shown as vertical bars (often smaller than the symbol size).

1174 In addition to characterizing the magnitude of jet quenching products (via the centrality-  
1175 dependent excess of low- $p_T^{trk}$  tracks greatest in correlations to subleading jets but also present in  
1176 leading jet correlations), modifications to charged-particle correlated yields may also be character-  
1177 ized by their widths. These studies are relevant to look for the presence and extent of jet peak  
1178 broadening due to medium interactions, and can be used to distinguish between different models  
1179 for jet-medium interaction and medium-modified jet radiation. In order to characterize correlation  
1180 widths, correlations are fit to double-gaussian functions (all  $\Delta\eta$  fits are shown in Appendix D for  
1181 illustration), and the width ( $\sigma$ ) of these fits is obtained as the range in  $|\Delta\eta|$  or  $|\Delta\phi|$  containing  
1182 67% of the total yield under the fit curve. To obtain systematic uncertainties on these fits, points  
1183 are varied up and down by their systematic uncertainties, and widths are re-calculated from these  
1184 varied distributions.

1185 Figures 51 and 52 show correlation widths in  $\Delta\eta$  and  $\Delta\phi$  for leading jets in PbPb and  
1186 pp data at 2.76 TeV. At low- $p_T^{trk}$  there is a significant broadening evident in central PbPb data  
1187 when compared to pp data, with this broadening decreasing in more peripheral collisions and with  
1188 increasing  $p_T^{trk}$  (with similar trends to those exhibited by correlated yield magnitudes). Widths  
1189 and width modifications are similar in  $\Delta\eta$  and  $\Delta\phi$ , but slightly broader in  $\Delta\phi$  for PbPb data.  
1190 These leading jet correlation widths and width modifications may also be compared to subleading  
1191 jet correlation widths and width modifications, shown in Figs. 53 and 54. In peripheral PbPb  
1192 data subleading and leading correlation widths are similar, but subleading jet PbPb correlation  
1193 widths exhibiting less centrality dependence than leading jet correlation widths so that leading jet  
1194 correlations in central PbPb data are slightly broader than subleading jet correlations (but  
1195 not significantly so, when taking into account the systematic uncertainties on both measurements).  
1196 Subleading jet peaks in pp data are, however, significantly broader than leading jet peaks in pp  
1197 data—as is to be expected since the kinematic selection defining subleading jet as that with lower- $p_T$ ,  
1198 also implies that subleading jets will on average have softer fragmentation than leading jets. Since  
1199 subleading pp jets are broader than leading pp jets while subleading and leading jets have similar  
1200 widths in PbPb, the jet peak broadening quantified as the PbPb–pp difference in widths is greater  
1201 for leading jets than for subleading jets.

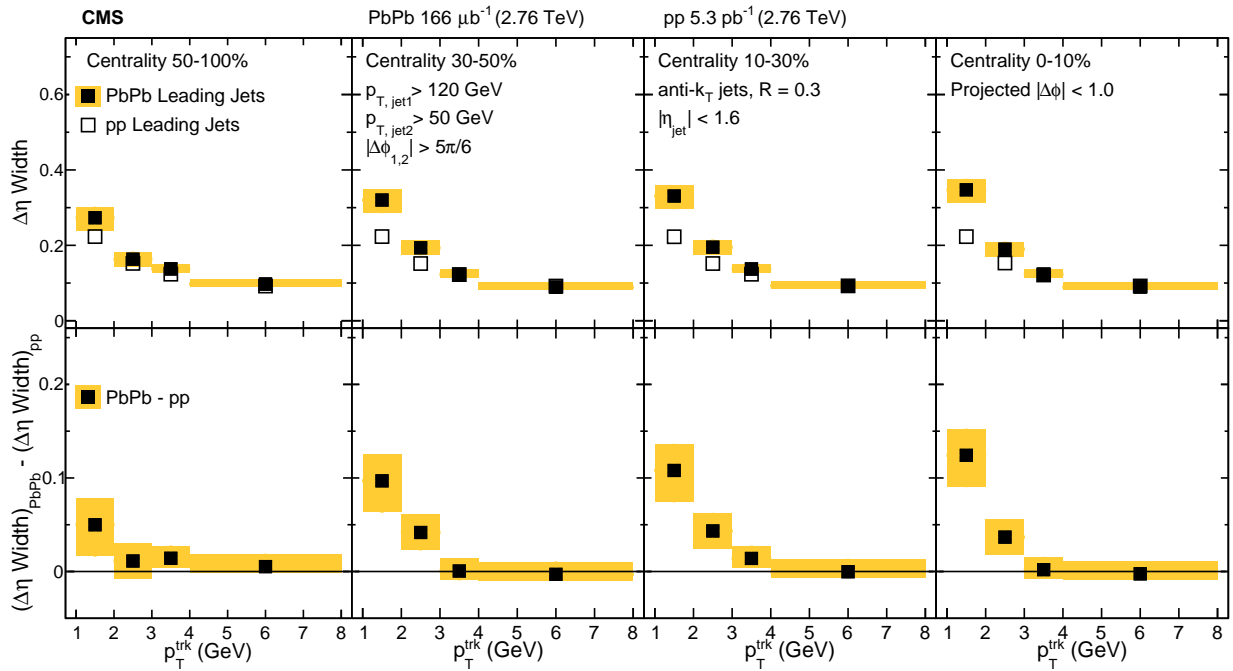


Figure 51. Comparison of the widths in PbPb and pp of the  $\Delta\eta$  charged-particle distributions correlated to leading jets with  $p_{T,\text{jet}1} > 120 \text{ GeV}$ , as a function of  $p_T^{\text{trk}}$ . The bottom row shows the difference of the widths in PbPb and pp data. The shaded band corresponds to systematic uncertainty, and statistical uncertainties are smaller than symbol size.

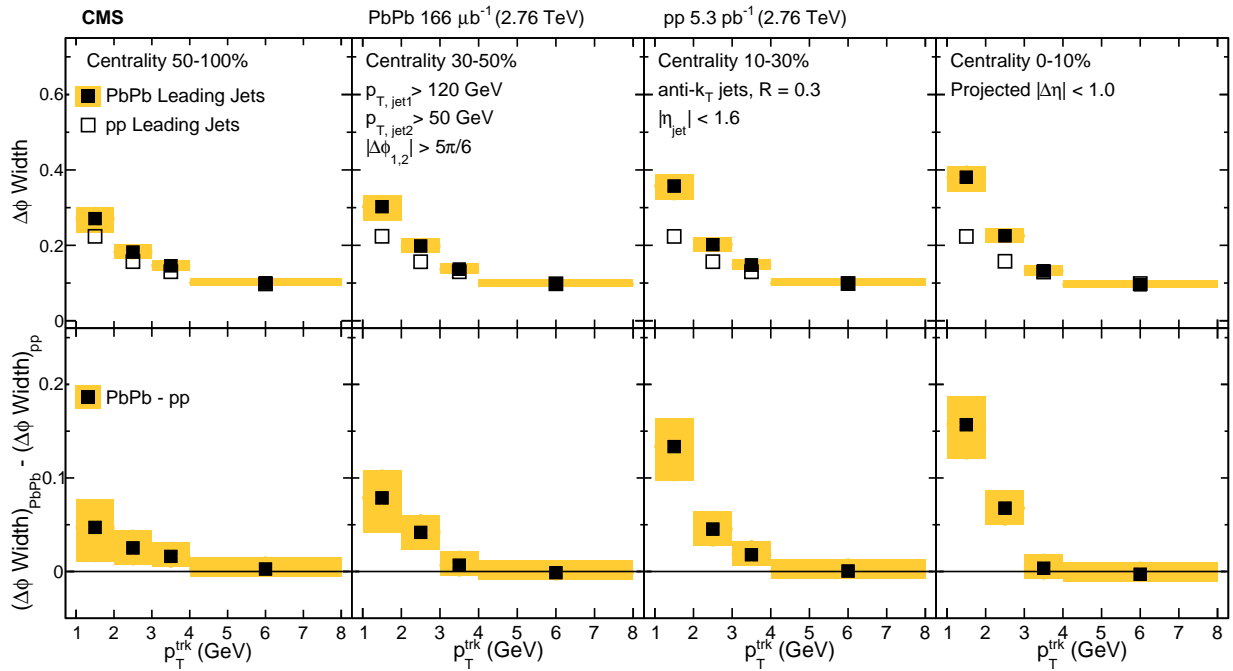


Figure 52. Comparison of the widths in PbPb and pp of the  $\Delta\phi$  charged-particle distributions correlated to leading jets with  $p_{T,\text{jet}1} > 120 \text{ GeV}$ , as a function of  $p_T^{\text{trk}}$ . The bottom row shows the difference of the widths in PbPb and pp data. The shaded band corresponds to systematic uncertainty, and statistical uncertainties are smaller than symbol size.

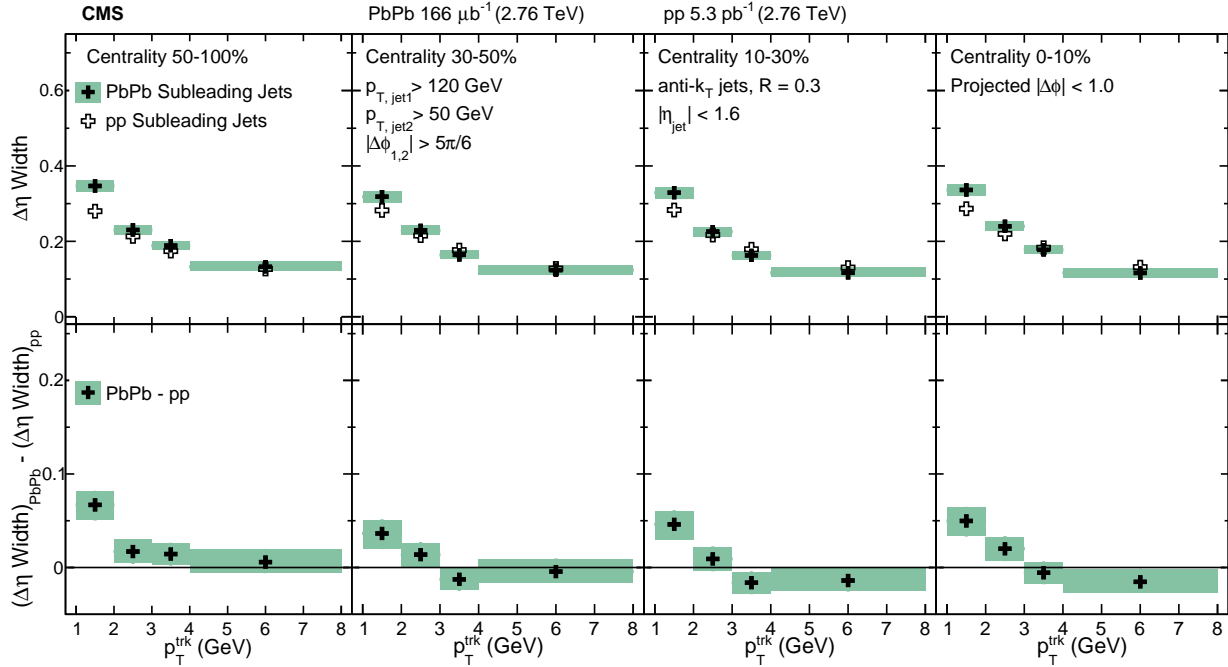


Figure 53. Comparison of the widths in PbPb and pp of the  $\Delta\eta$  charged-particle distributions correlated to leading jets with  $p_{T,\text{jet}2} > 50$  GeV, as a function of  $p_T^{\text{trk}}$ . The bottom row shows the difference of the widths in PbPb and pp data. The shaded band corresponds to systematic uncertainty, and statistical uncertainties are smaller than symbol size.

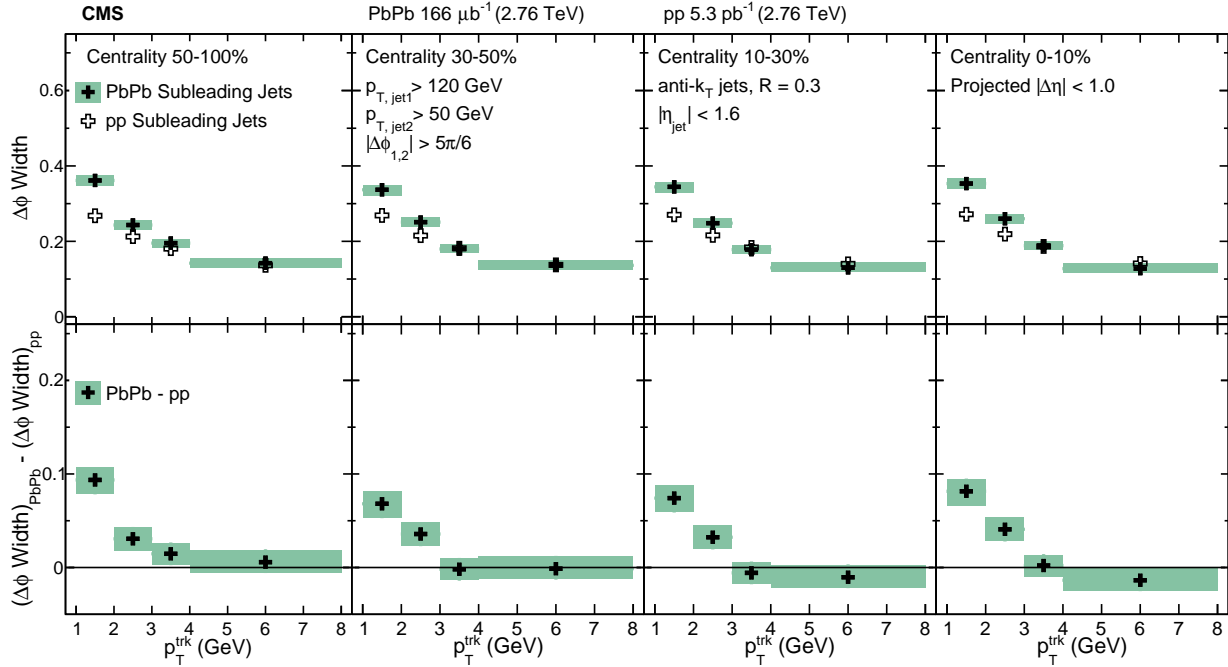


Figure 54. Comparison of the widths in PbPb and pp of the  $\Delta\phi$  charged-particle distributions correlated to leading jets with  $p_{T,\text{jet}2} > 50$  GeV, as a function of  $p_T^{\text{trk}}$ . The bottom row shows the difference of the widths in PbPb and pp data. The shaded band corresponds to systematic uncertainty, and statistical uncertainties are smaller than symbol size.

1202 **10.3 Jet shapes**

1203 A common observable to characterize and compare the widths of jet peaks is the jet shape  $\rho_{\Delta r}$ ,  
 1204 measuring the fraction of total jet transverse momentum as a function of distance  $\Delta r$  from the jet  
 1205 axis. As discussed in Sec. 4, previous CMS measurements of jet shape [18] have gained particular  
 1206 attention from the theoretical community in efforts to constrain models of jet energy loss. Jet shape  
 1207 measurements to large angles ( $\Delta r = 1$ , compared to previous measurements to only  $\Delta r = 0.3$ ) may  
 1208 be obtained from correlation studies, extending measurements to the full range of the jet peak  
 1209 and offering the capability of distinguishing between theoretical predictions based on earlier, more  
 1210 narrow, measurements.

1211 In the correlation technique, jet shapes are obtained by weighting correlations by  $p_T^{\text{trk}}$ , and  
 1212 integrating the resulting (background-subtracted) 2D jet-peak momentum distributions in annuli  
 1213 with radial width  $\Delta r = 0.05$ , where each has an inner radius of  $r_a = \Delta r - \delta r/2$  and an outer radius  
 1214 of  $r_b = \Delta r + \delta r/2$ . For this measurement, an inclusive high- $p_T^{\text{trk}}$  bin is included to capture particles  
 1215 with  $20 < p_T^{\text{trk}} < 300$  GeV. The resulting transverse momentum profile of the jet is defined as:

$$P(\Delta r) = \frac{1}{\delta r} \frac{1}{N_{\text{jets}}} \sum_{\text{jets}} \sum_{\text{tracks} \in (r_a, r_b)} p_T^{\text{trk}} \quad (15)$$

1216 This profile is then normalized to unity within  $\Delta r = 1$  to produce the jet shape  $\rho(\Delta r)$ :

$$\rho(\Delta r) = \frac{1}{\delta r} \frac{\sum_{\text{jets}} \sum_{\text{tracks} \in (r_a, r_b)} p_T^{\text{trk}}}{\sum_{\text{jets}} \sum_{\text{tracks}} p_T^{\text{trk}}} \quad (16)$$

1217 The top row of Fig. 55 presents the inclusive jet transverse momentum profile  $P(\Delta r)$  in pp  
 1218 and PbPb data at 5.02 TeV, while the middle row shows the jet shape  $\rho(\Delta r)$ , normalized to unity  
 1219 within  $\Delta r = 1$ . Here again redistribution of energy from small to large angles from the jet cone is  
 1220 evident in PbPb relative to pp reference, as seen in the dipping then rising trend in the jet shape  
 1221 ratio  $\rho(\Delta r)_{\text{PbPb}}/\rho(\Delta r)_{\text{pp}}$  presented in the bottom row.

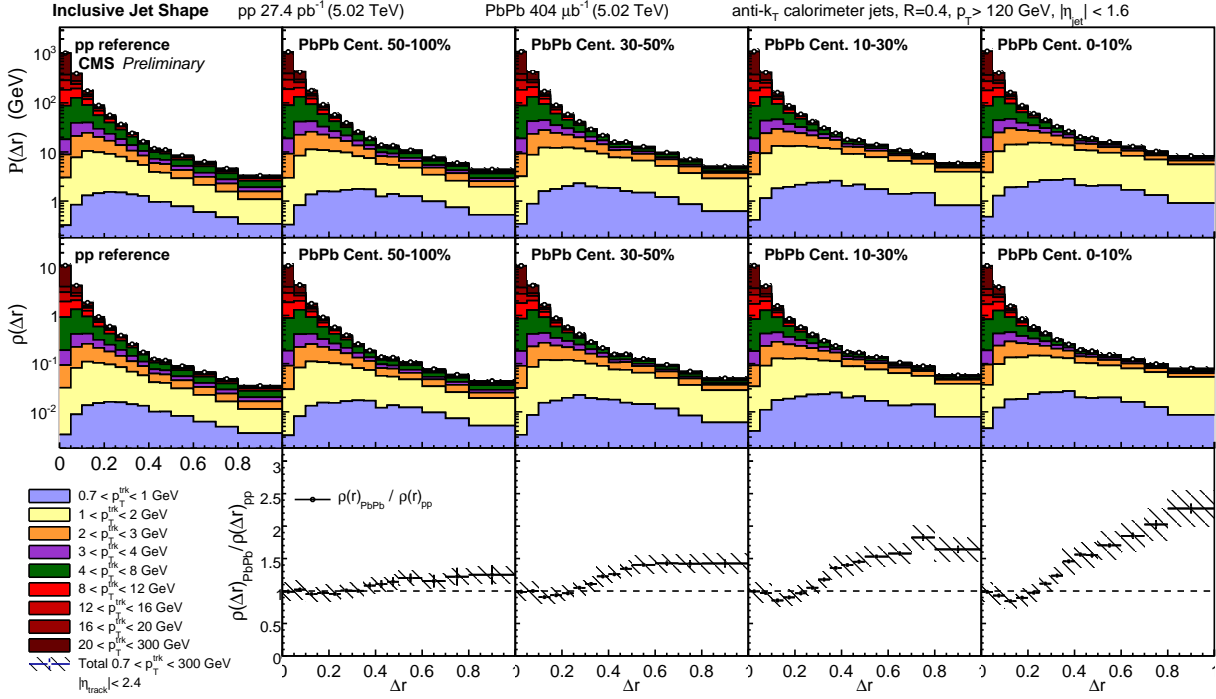


Figure 55. Top row: Transverse momentum profile of inclusive jets  $P(\Delta r)$  in pp and PbPb data at 5.02 TeV, shown differentially in  $p_T^{\text{trk}}$ . Middle row: jet shapes  $\rho(\Delta r)$  (normalized to unity over  $\Delta r < 1$ ) in PbPb and pp. Bottom row: jet shape ratio  $\rho(\Delta r)_{\text{PbPb}} / \rho(\Delta r)_{\text{pp}}$ . Hatched lines on  $p_T^{\text{trk}}$ -inclusive points show total systematic uncertainties.

In addition to studies of inclusive jet shapes, it is also interesting to consider the jet shapes and jet shape modifications of leading and subleading jets in dijet events. These studies are carried out with the same selection of 2.76 TeV dijet events used for the correlation studies presented in 10.2. In this case, for consistency with a previous CMS study measured the jet shape  $\rho(\Delta r)$  within the jet cone radius  $\Delta r = 0.3$  [18] at 2.76 TeV, these leading and subleading jet shape measurements at 2.76 TeV are normalized to integrate to unity with in the radius  $\Delta r < 0.3$ . In Fig. 56, the leading jet shape measured with this correlation technique is compared to the published CMS reference and extend this measurement to  $\Delta r = 1$ , noting that the leading jet shape is consistent within uncertainties with the previous measurement for an inclusive jet selection of all jets with  $p_T > 100$  GeV. A new measurement of subleading jet shape in Fig. 57 is then presented. As noted in the correlation width measurements discussed in Sec. 10.2, subleading jets in pp data are broader than leading jets in pp data. Therefore, although the PbPb-to-pp *modifications* are similar for leading and subleading jets, the more steeply falling pp leading jet shape results in a greater *relative*

1235 modification shown in the jet shape ratio  $\rho_{\text{PbPb}}(\Delta r)/\rho_{\text{pp}}(\Delta r)$  for leading than for subleading jets.  
 1236 Similarly, when comparing jet shape measurements at 2.76 TeV to those at 5.02 TeV, it is relevant  
 1237 to note that the pp reference is broader at 5.02 TeV than at 2.76 TeV, likely due to the greater  
 1238 fraction of gluon versus quark jets that pass the kinematic selections of the analysis at the higher  
 1239 center-of-mass energy.

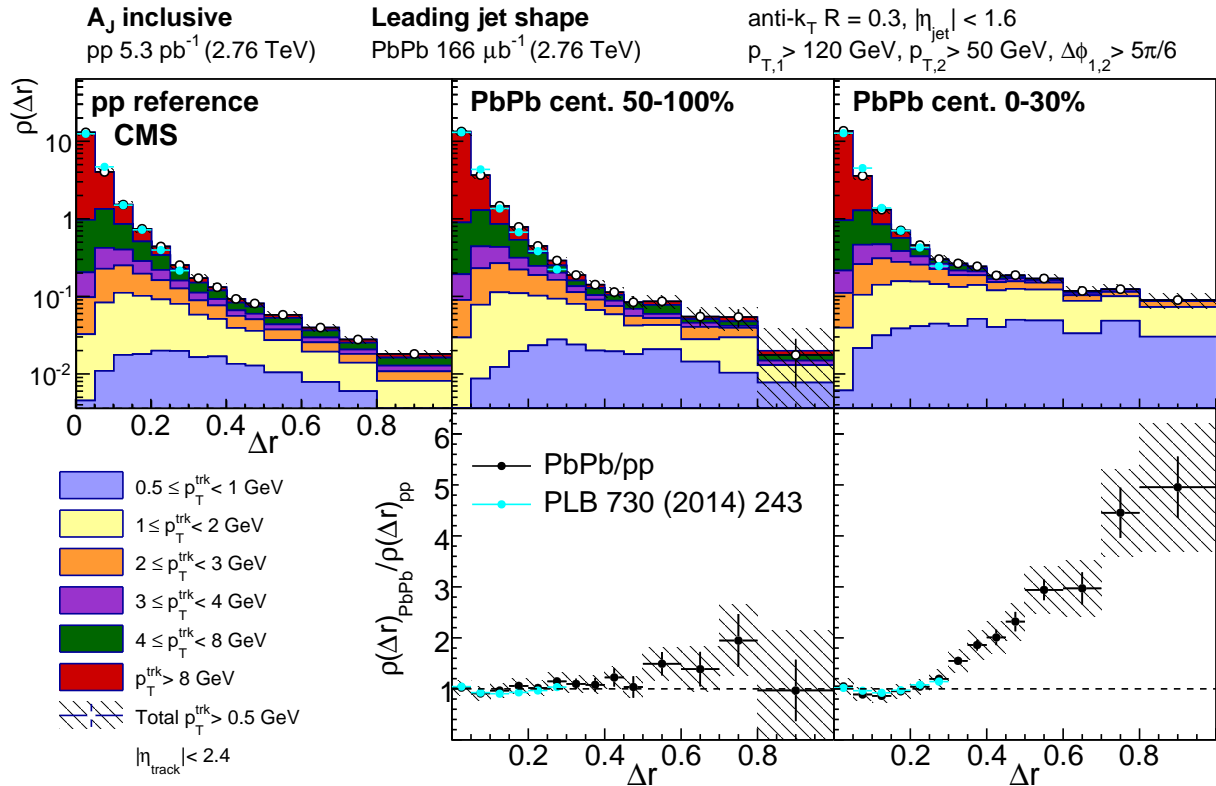


Figure 56. Top row: leading jet shape  $\rho(\Delta r)$  for pp reference and central and peripheral PbPb data, shown for all tracks with  $p_{T}^{\text{trk}} > 0.5 \text{ GeV}$  and decomposed by track transverse momentum. Shapes are normalized to unity over the region  $r < 0.3$  for consistency with the published reference shown (Ref. [18]). Bottom row: leading jet shape ratio  $\rho(\Delta r)_{\text{PbPb}}/\rho(\Delta r)_{\text{pp}}$ , again with published reference.

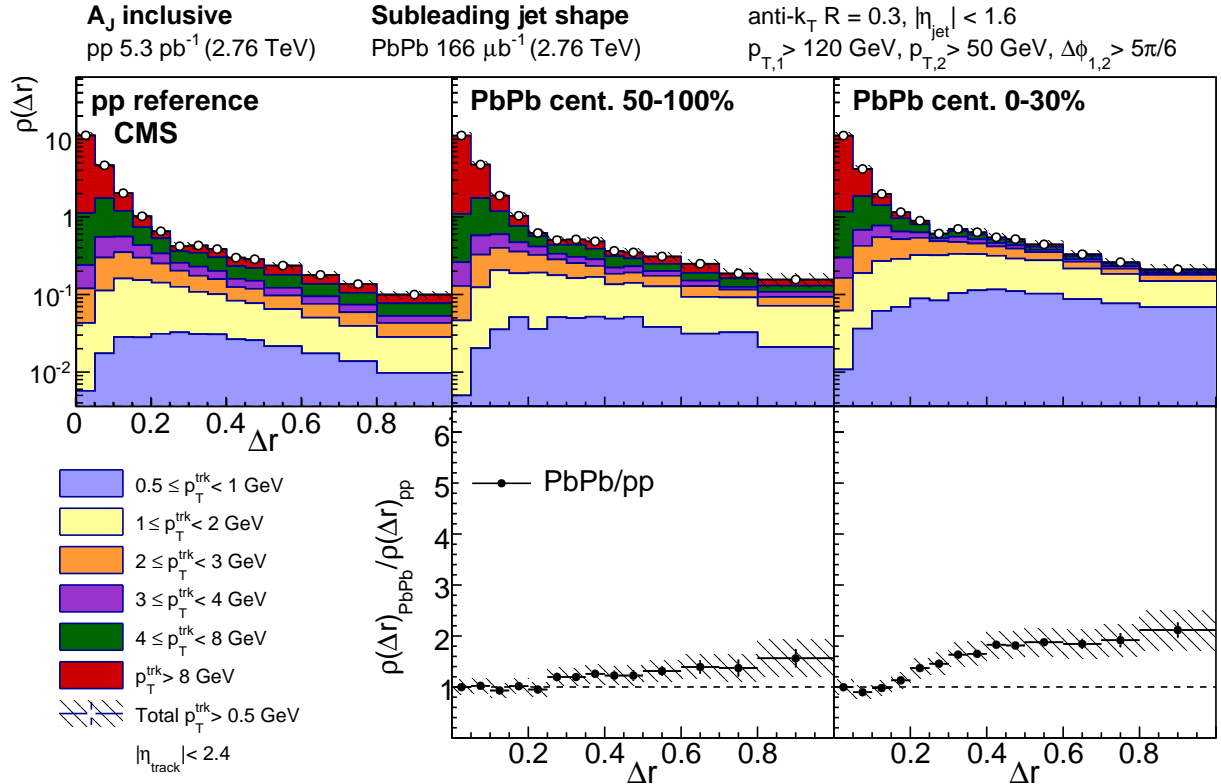


Figure 57. Top row: subleading jet shape  $\rho(\Delta r)$  for pp reference and central and peripheral PbPb data, shown for all tracks with  $p_T > 0.5$  GeV and decomposed by track transverse momentum, normalized to unity over the region  $\Delta r < 0.3$ . Bottom row: subleading jet shape ratio  $\rho(\Delta r)_{\text{PbPb}} / \rho(\Delta r)_{\text{pp}}$ .

1240 **10.4 Decomposition of hemisphere momentum balance in dijet events**

1241 The dijet results at 2.76 TeV presented in this analysis are complimented by other CMS measure-  
1242 ments conducted on the same data using the “missing- $p_T$ ” hemisphere momentum balance method  
1243 presented in Ref. [41] and discussed in Secs. 3 and 4. In this analysis, a “dijet” axis is constructed  
1244 by averaging the leading jet and subleading jet axes (these are separated by  $\Delta\phi_{1,2} = \pi$  on average,  
1245 but are not necessarily parallel in each event due to 3-jet events) to construct a dijet axis, dividing  
1246 the event into leading and subleading hemispheres with respect to this axis, and comparing the  
1247 hemisphere-wide distributions of  $p_T^{\text{trk}}$  (projected, in this case, onto the combined dijet axis) to ob-  
1248 tain the subleading-to-leading balancing distribution as a function of distance from the dijet axis  
1249  $\Delta r$ . The jet track correlation technique may be used to obtain this same measurement (comparing  
1250 subleading-to-leading distributions on average rather than event-by-event, and making use of the  
1251 fact that the subleading and leading jet axes are *on average* perfectly back-to-back). When this  
1252 cross-check is performed *without background subtraction*, the two techniques yield consistent results,  
1253 despite methodological differences and differences in jet- $\eta$  cuts. This hemisphere-wide missing- $p_T$   
1254 technique is also used to extract differences in total particle yields between the leading and sublead-  
1255 ing hemispheres, and shows an average excess of 4–5 particles with  $p_T^{\text{trk}}$  in the subleading hemisphere  
1256 compared to the leading hemisphere [41]. In the dijet correlation studies presented in this analysis  
1257 *with background subtraction*, however, only approximately 2 additional particles were found cor-  
1258 related to the subleading jet peak compared to the leading jet peak, as shown in Sec. 10.2. This  
1259 apparent difference motivates a detailed examination and decomposition of the distribution of  $p_T^{\text{trk}}$   
1260 in dijet events in order to consider contributions to the hemisphere-wide momentum balance from  
1261 both the leading and subleading jet peaks, and from the long-range correlated underlying event.

1262 For this investigation, the dijet samples of 2.76 TeV PbPb and pp data are each divided  
1263 based on asymmetry parameter  $A_J$  to further illuminate quenching effects and to decompose the  
1264 contributions to the hemisphere  $p_T^{\text{trk}}$  balance studied in Ref. [41]: a balanced sample with  $A_J < 0.22$ ,  
1265 and an “unbalanced” sample with  $A_J > 0.22$ . Transverse momentum distributions for each sample  
1266 are constructed in  $\Delta\eta - \Delta\phi$  for each sample, and are corrected for pair-acceptance effects. Like all  
1267 particle density and  $p_T^{\text{trk}}$  correlations studied in this analysis, these show jet peaks on an underlying  
1268 event that shows significant  $\Delta\phi$  correlations but is flat in  $\Delta\eta$ . Correlations are therefore projected

1269 into  $\Delta\phi$  for further study in order to preserve this underlying event structure. Studies will begin  
1270 by considering the hemisphere-wide “missing- $p_T$ ” distribution as a function of  $\Delta\phi$ , and will then  
1271 decompose this distribution into jet peak and underlying event contributions, and finally consider  
1272 the relative contributions from jet peaks and from the underlying event to the overall hemisphere  
1273  $p_T^{\text{trk}}$  balance for balanced and unbalanced dijets.

1274 Figures 58 and 59 present the hemisphere-wide balancing distribution of transverse momen-  
1275 tum around the subleading versus the leading jet for balanced and unbalanced dijets respectively.  
1276 For both selections, a wide excess of soft particles in the subleading versus leading hemisphere in  
1277 central PbPb collisions relative to pp reference is evident, reflecting the greater quenching of the  
1278 subleading jet. In the unbalanced selection, as required by momentum conservation, the signal is  
1279 enhanced in both pp and PbPb data: in pp a large excess of particles with  $p_T > 3$  GeV long-range  
1280 is present on the subleading side, compensating for the lower momentum of the highest- $p_T$  particles  
1281 in the jet itself. In peripheral PbPb data the distribution is quite similar to pp reference, while  
1282 in central PbPb data this balancing distribution consists mostly of soft particles  $p_T < 3$  GeV,  
1283 consistent with the findings of a previous CMS study [41]. To better demonstrate these medium  
1284 modifications, the difference in yield between PbPb and pp collisions is shown in the bottom panels  
1285 of Fig. 58 and Fig. 59.

1286 To better understand the redistribution of transverse momentum within the QGP, the  
1287 distributions are then separated into three components as discussed above: the gaussian-like peaks  
1288 about the leading and subleading jet axes, plus a component accounting for overall subleading-  
1289 to-leading asymmetry in the  $\Delta\phi$ -correlated long-range underlying event (measured in the region  
1290  $1.5 < |\Delta\eta| < 2.5$ ). In Fig. 60 and Fig. 61, the jet peak components are shown for balanced and  
1291 unbalanced jets respectively, presenting subleading results positive and leading results negative (in  
1292 line with the hemisphere difference measurements in Fig. 59 and Fig. 58). Jet peak distributions  
1293 after decomposition are projected over the full range  $|\Delta\eta| < 2.5$ , again for consistency with the  
1294 hemisphere difference measurements. The top row of each panel first shows the overall distribution  
1295 of momentum carried by particles with  $p_T < 8$  GeV on about the jet peak. The middle two panels  
1296 then assess modifications to the subleading and leading jets respectively. Here there is evidence  
1297 of quenching to both the subleading and the leading jet in central PbPb collisions relative to pp  
1298 reference, with an excess of low- $p_T^{\text{trk}}$  particles correlated to the jet axis in both the balanced and

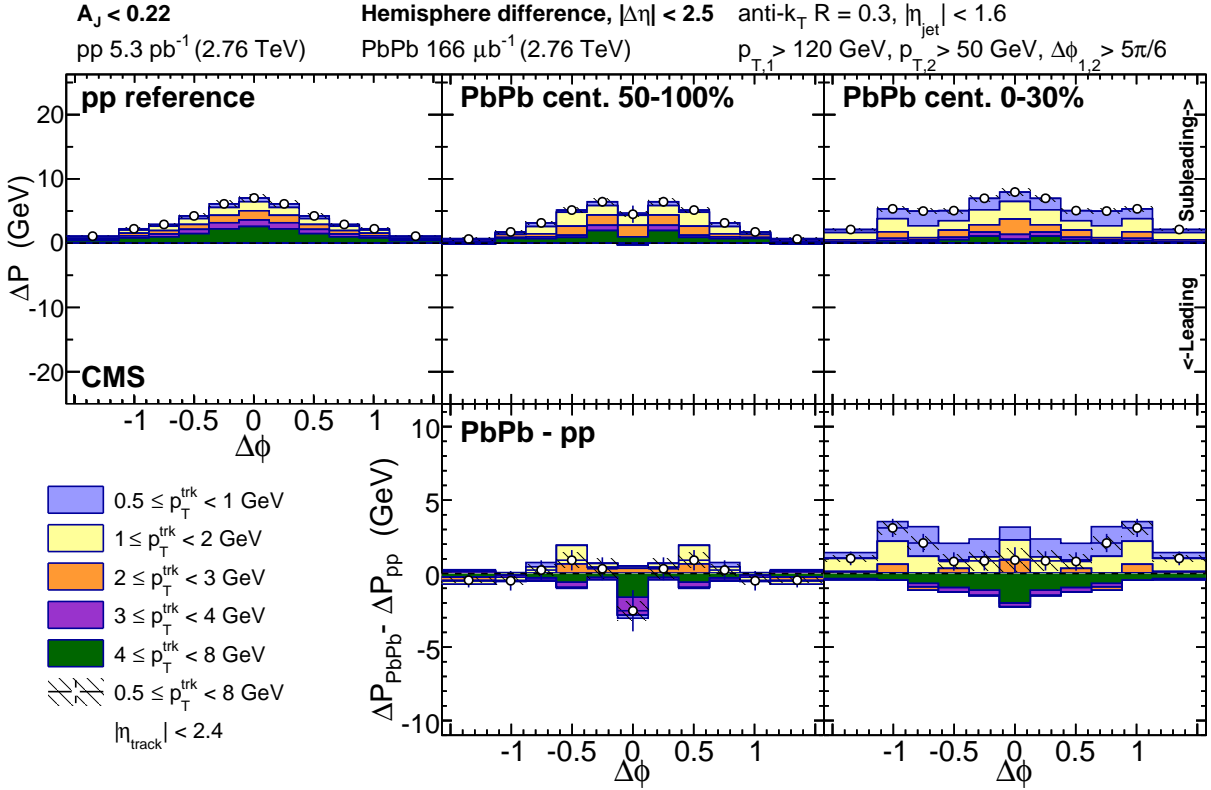


Figure 58. Top row: total hemisphere distribution in  $\Delta\phi$  of excess transverse momentum about the subleading relative to the leading jet for balanced dijets with  $A_J < 0.22$ , shown differentially by track transverse momentum for pp reference, peripheral PbPb, and central PbPb data. Bottom row: PbPb–pp difference in these  $\Delta\phi$  momentum distributions.

1299 unbalanced dijet selections, as observed in the charged particle density studies presented in Sec. 10.2.  
 1300 In unbalanced dijets this enhancement of soft- $p_T^{\text{trk}}$  particles turns into a depletion at higher- $p_T^{\text{trk}}$ , and  
 1301 is greater on the subleading than the leading side. To compare between hemispheres and assess the  
 1302 jet peak contribution to the overall hemisphere momentum balance, the double difference PbPb–pp,  
 1303 subleading–leading is presented in the bottom panel. Here it is evident that the low- $p_T^{\text{trk}}$  excess  
 1304 in central PbPb collisions is larger on the subleading than the leading side of the dijet system,  
 1305 but larger subleading-to-leading excess only accounts for only a portion of the total momentum  
 1306 redistribution in unbalanced dijet events.

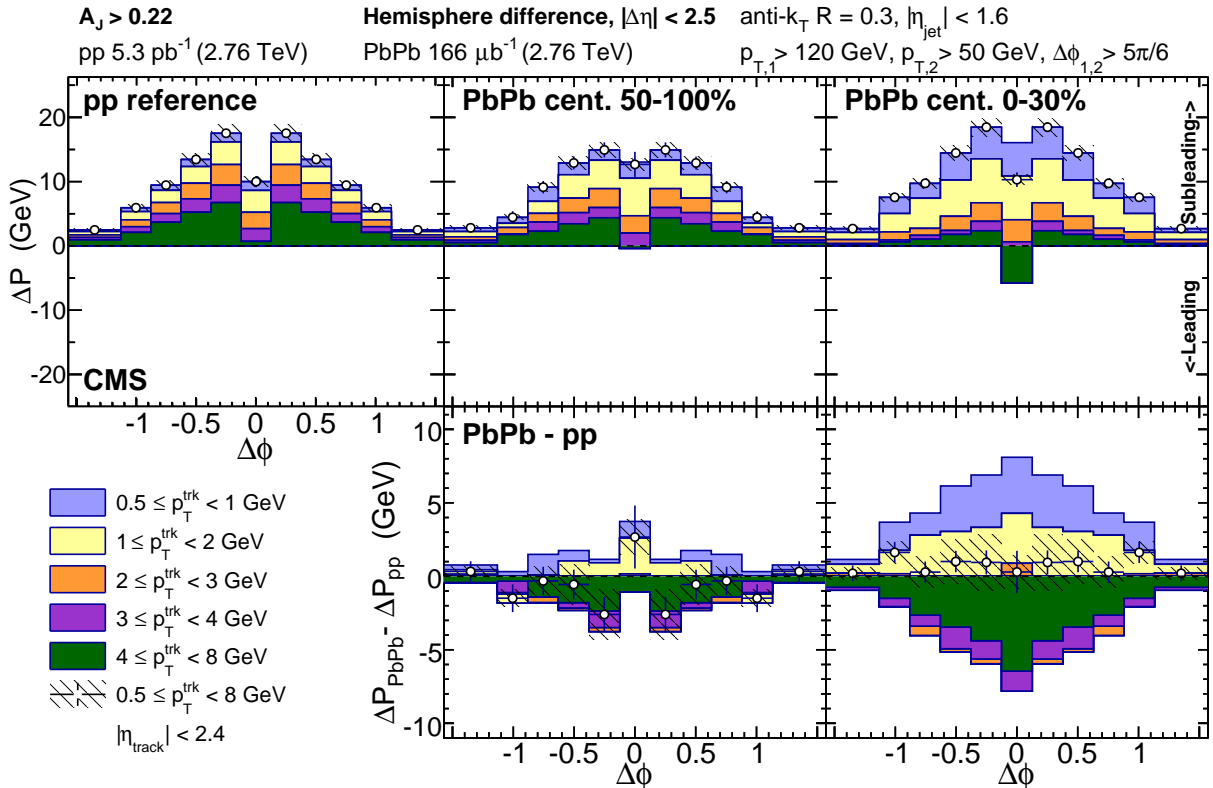


Figure 59. Top row: total hemisphere distribution in  $\Delta\phi$  of excess transverse momentum about the subleading relative to the leading jet for balanced dijets with  $A_J > 0.22$ , shown differentially by track transverse momentum for pp reference, peripheral PbPb, and central PbPb data. Bottom row: PbPb-pp difference in these  $\Delta\phi$  momentum distributions.

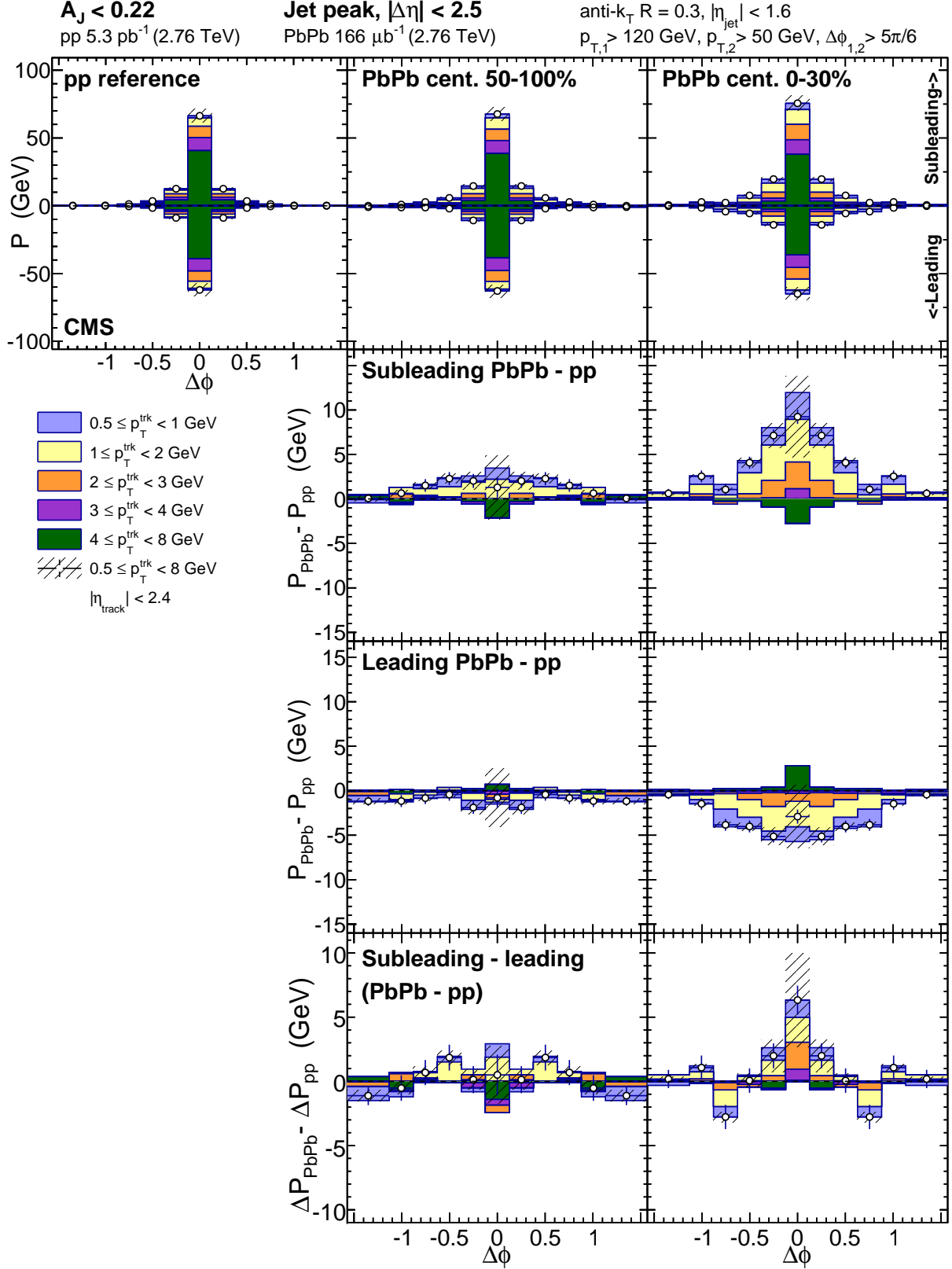


Figure 60. Top row: jet-peak (long-range subtracted) distribution in  $\Delta\phi$  of transverse momentum about the subleading (plotted positive) and leading (plotted negative) jets for balanced dijets with  $A_J < 0.22$ . Middle rows: PbPb–pp momentum distribution differences for subleading and leading jets. Bottom row: PbPb–pp, subleading–leading double difference in these  $\Delta\phi$  momentum distributions.

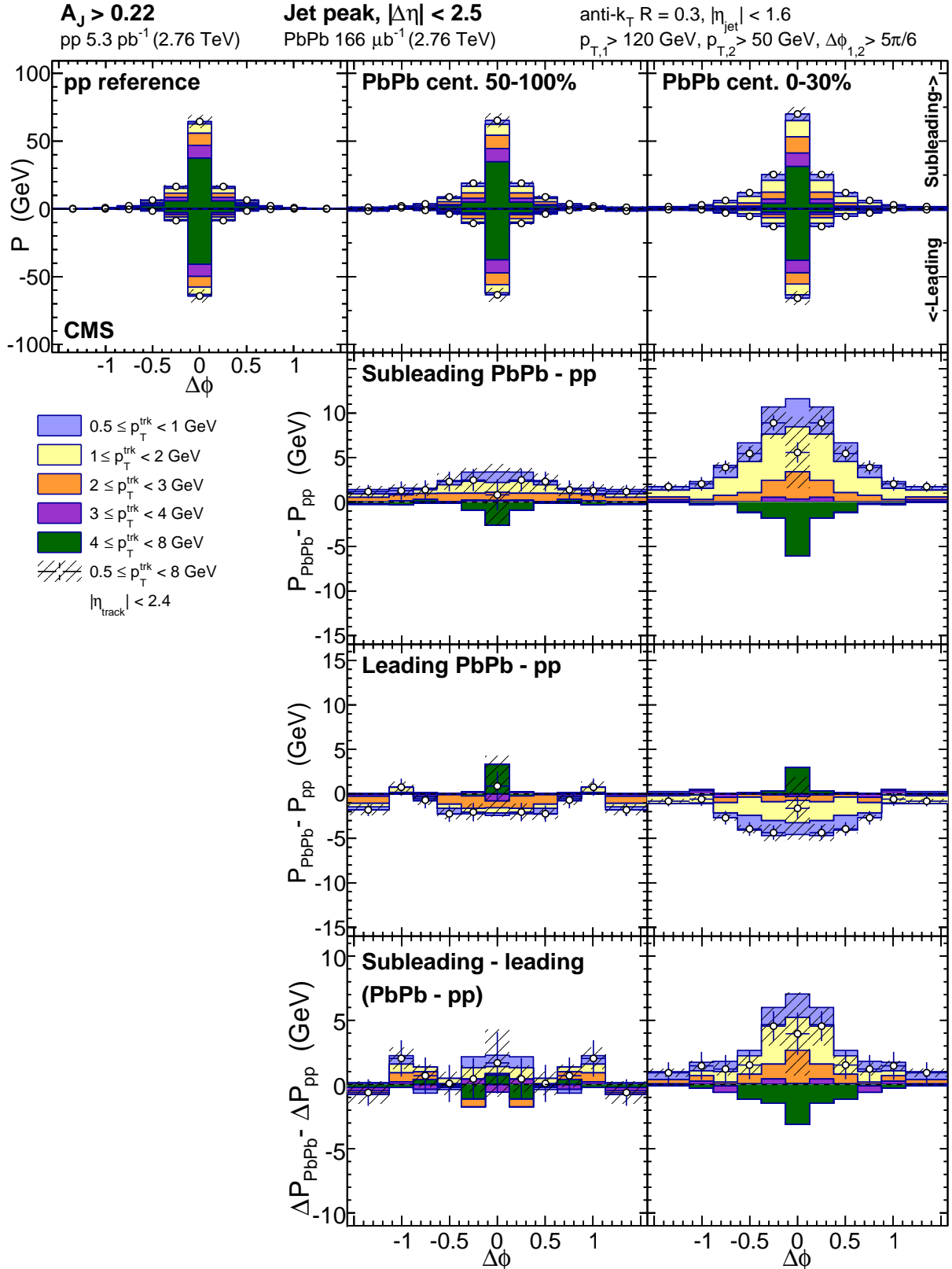


Figure 61. Top row: jet-peak (long-range subtracted) distribution in  $\Delta\phi$  of transverse momentum about the subleading (plotted positive) and leading (plotted negative) jets for balanced dijets with  $A_J > 0.22$ . Middle rows: PbPb-pp momentum distribution differences for subleading and leading jets. Bottom row: PbPb-pp, subleading-leading double difference in these  $\Delta\phi$  momentum distributions.

These jet-related studies are complemented by an analysis of the long-range subleading to leading asymmetry, presented in Fig. 62 and Fig. 63 for balanced and unbalanced jets respectively. The long-range correlated background in balanced dijet events is symmetric in pp and peripheral PbPb data, while in central PbPb data there is a small excess of low- $p_T^{\text{trk}}$  particles. In unbalanced dijets, however, there is significant asymmetry already in pp reference, with a large correlated excess of particles in all  $p_T$  classes less than 8 GeV on the subleading relative to leading side of the underlying event. This asymmetry reflects the presence of other hard-scattering products in the subleading hemisphere dijet event, as required by momentum conservation when selecting asymmetric dijets in vacuum-like collisions. In the presence of the strongly interacting medium; however, this underlying event asymmetry in asymmetric dijet events changes notably. In peripheral PbPb collisions there is already some depletion of momentum carried by high- $p_T^{\text{trk}}$  particles, and in central pp collisions subleading-to-leading underlying event excesses with  $p_T^{\text{trk}} > 2$  GeV vanish nearly completely. To assess the contribution of this long-range asymmetry to the total hemisphere imbalance, the double difference PbPb–pp, subleading–leading is plotted on the bottom panel as for (and on the same scale as) the double difference shown for the jet peaks. To assess the overall hemisphere momentum balance attributed to this long-range asymmetry, the hemisphere integral ( $|\Delta\phi| < \pi/2$  and  $|\Delta\eta| < 2.5$ ) is presented in Fig. 64 for balanced versus unbalanced dijets. For unbalanced dijets, the the overall asymmetry rises with track- $p_T$  pp reference, but falls with track- $p_T$  for central PbPb data.

Finally, to show the relative contributions to overall hemisphere momentum balance from the leading and subleading jet peaks as well as from the long-range underlying event asymmetry, a summary of hemisphere-integrated excess (PbPb–pp) yield for balanced and unbalanced dijets in central PbPb collisions is shown in Fig. 65 and Fig. 66 for central and peripheral collisions respectively. The top panels of Fig. 65 present total PbPb minus pp differences in transverse momentum associated with the subleading jet (plotted positive) and leading jet (plotted negative). Modifications to the distribution of tracks with  $p_T < 3$  GeV are evident for both the leading and subleading jet peaks, with a greater enhancement of low- $p_T^{\text{trk}}$  particles associated with the subleading jet. These total jet peak modifications in central PbPb collisions are not significantly different in unbalanced versus balanced dijets. The bottom panels of Fig. 65 present these jet-peak modifications together with the long-range modifications evident in Fig. 64 to show the decomposed

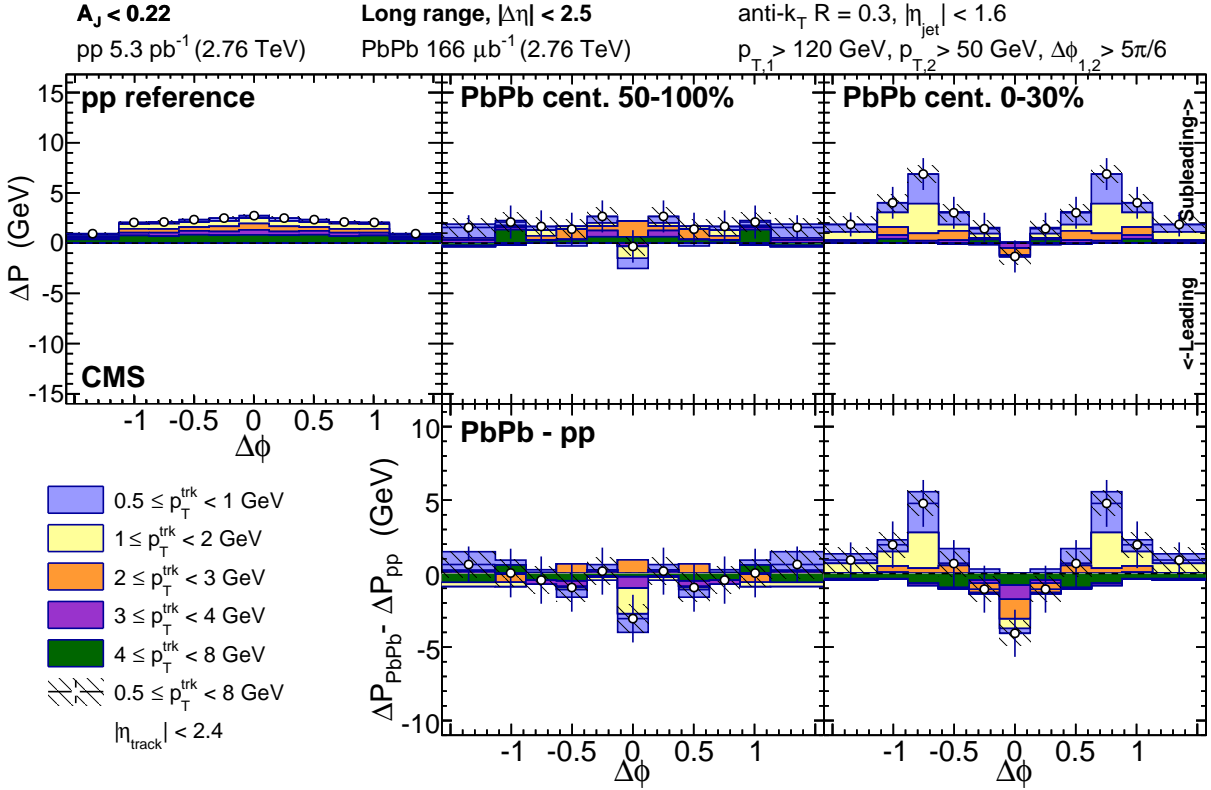


Figure 62. Top row: long-range distribution in  $\Delta\phi$  of excess transverse momentum in the subleading relative to leading sides for balanced dijets with  $A_J < 0.22$ . Bottom row: PbPb–pp difference in these  $\Delta\phi$  long-range momentum distributions.

hemisphere-wide differences in associated transverse momentum in each  $p_T^{\text{trk}}$  range. Unlike the jet peak contributions, the long-range PbPb versus modifications differ outside of uncertainties between balanced and unbalanced dijets: here the depletion of high- $p_T^{\text{trk}}$  particles in unbalanced PbPb versus pp dijets corresponds to the reduced contribution from third jets (which are prominently evident in the long-range distribution for pp unbalanced dijet events) in central PbPb unbalanced dijet events. Figure 66 presents the same hemisphere-integrated PbPb minus pp excess information for peripheral collisions for comparison to the central results shown in Fig. 65. Some possible small modifications are already evident in this 50-100% centrality range, but these differences between peripheral PbPb and pp results are in most cases smaller than systematic uncertainties.

The decomposition of integrated jet peak and long-range correlated  $p_T^{\text{trk}}$  shown in Fig. 65 and Fig. 66 clarify the relationship between the jet peak correlation studies presented in this analysis and the missing- $p_T$  measurements presented in Ref. [41]: as shown through this detailed decom-

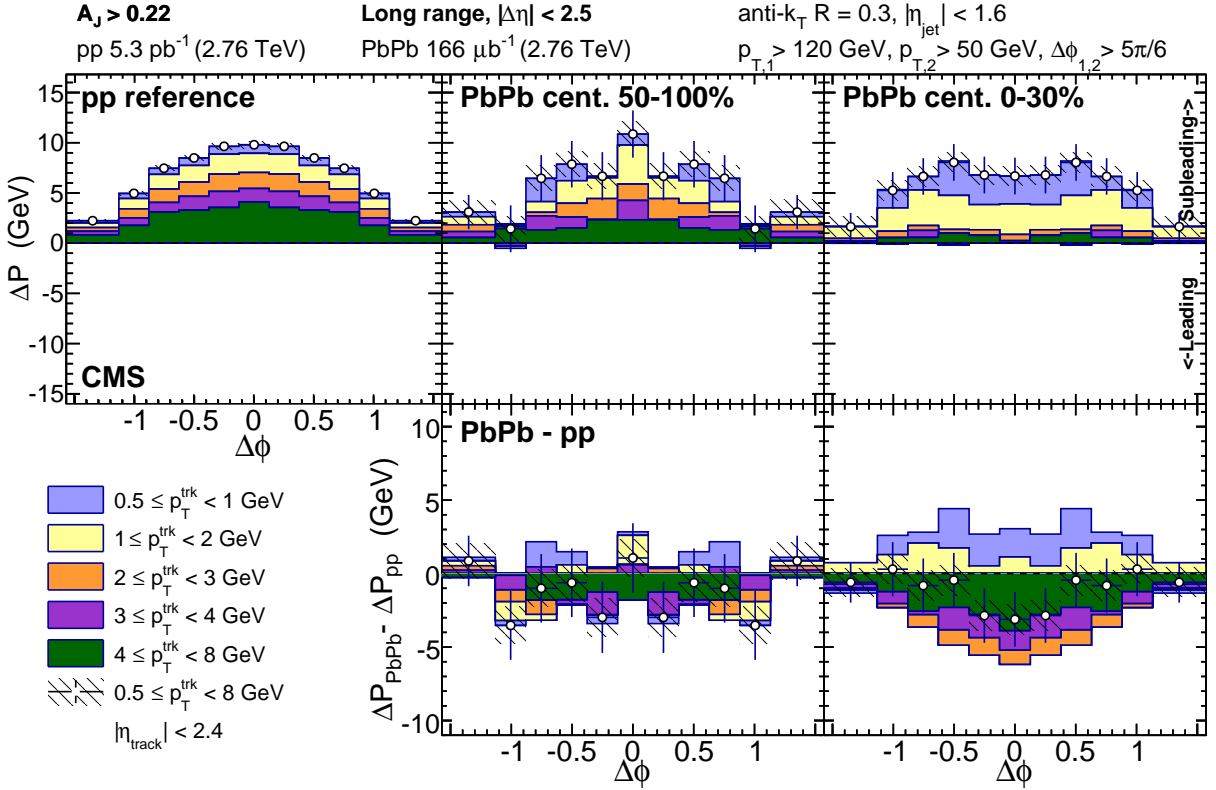


Figure 63. Top row: long-range distribution in  $\Delta\phi$  of excess tranverse momentum in the subleading relative to leading sides for balanced dijets with  $A_J > 0.22$ . Bottom row: PbPb–pp difference in these  $\Delta\phi$  long-range momentum distributions.

position, comparing hemisphere distributions as a whole include contributions from the subleading and leading jet peaks studied in correlation studies, but also a contribution from the underlying event. In both PbPb and pp data, the underlying event partially cancels with hemisphere subtraction: contributions from combinatoric background and even flow harmonics ( $V_2$  etc.) will cancel, while contributions from 3rd jets and odd flow harmonics ( $V_1$  etc.) will not. As we have seen, in pp the non-cancelling underlying event is dominated by 3rd jets, especially in the unbalanced dijet selection in which their presence is kinematically required. In PbPb, this underlying event has evident contributions from odd flow harmonics as well, reflecting coupling of jets to the event reaction plane.

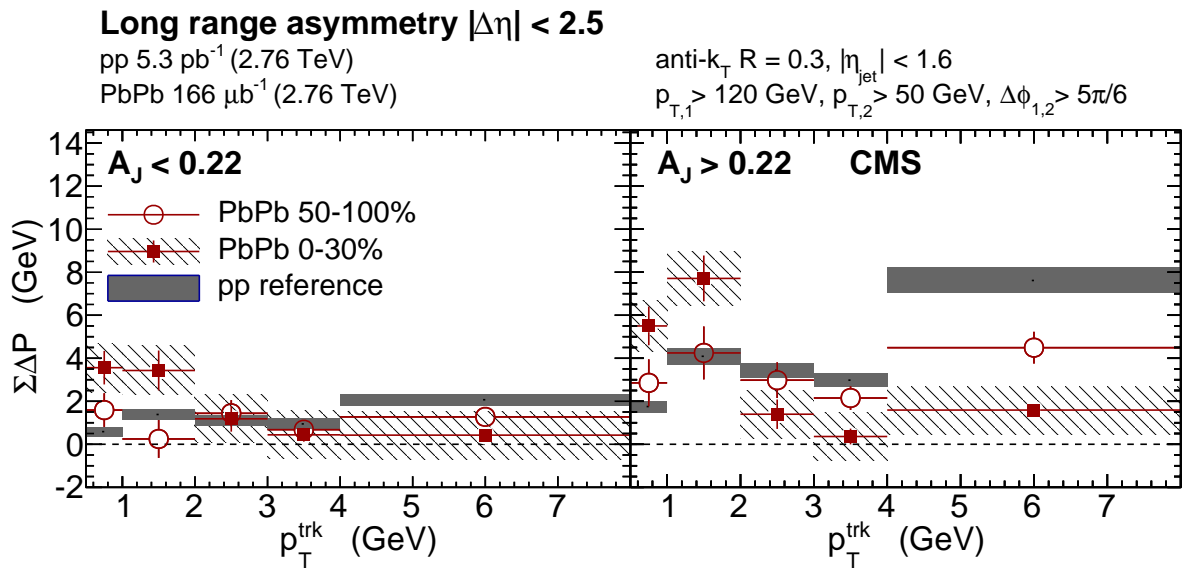


Figure 64. Integrated transverse momentum in the long-range  $\Delta\phi$ -correlated distribution as a function of track- $p_T$  integrated over  $|\Delta\phi| < \pi/2$  and  $|\Delta\eta| < 2.5$  and for pp reference, peripheral PbPb and central PbPb data for balanced compared to unbalanced dijets.

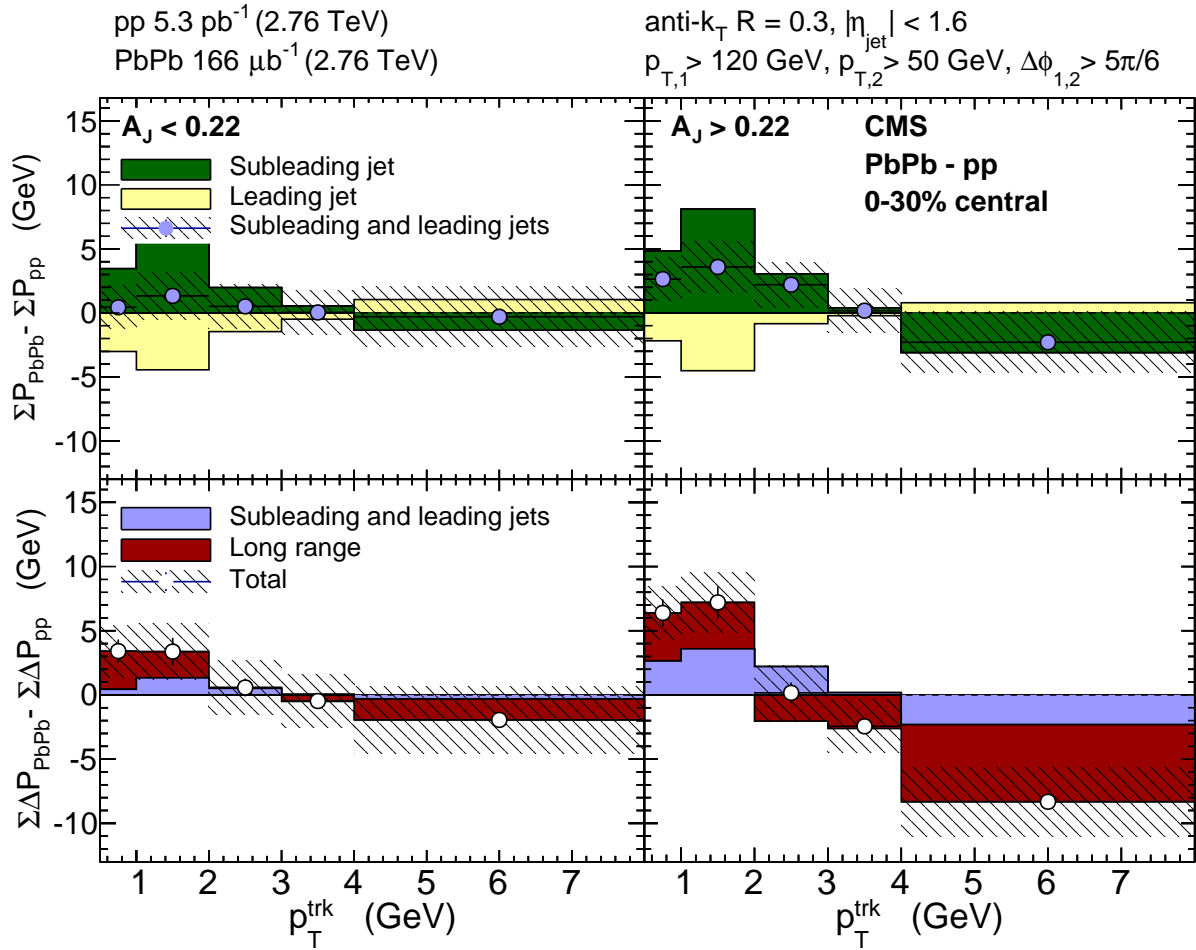


Figure 65. Modifications of jet-hadron correlated transverse momentum in central PbPb collisions with respect to pp reference, integrated  $|\Delta\phi| < \pi/2$ ,  $|\Delta\phi| < 2.5$ . Top row: subleading and leading jet peak PbPb-pp. Bottom row: relative contributions from jet peaks and long-range asymmetry to the double difference PbPb-pp, subleading-leading in total hemisphere transverse momentum.

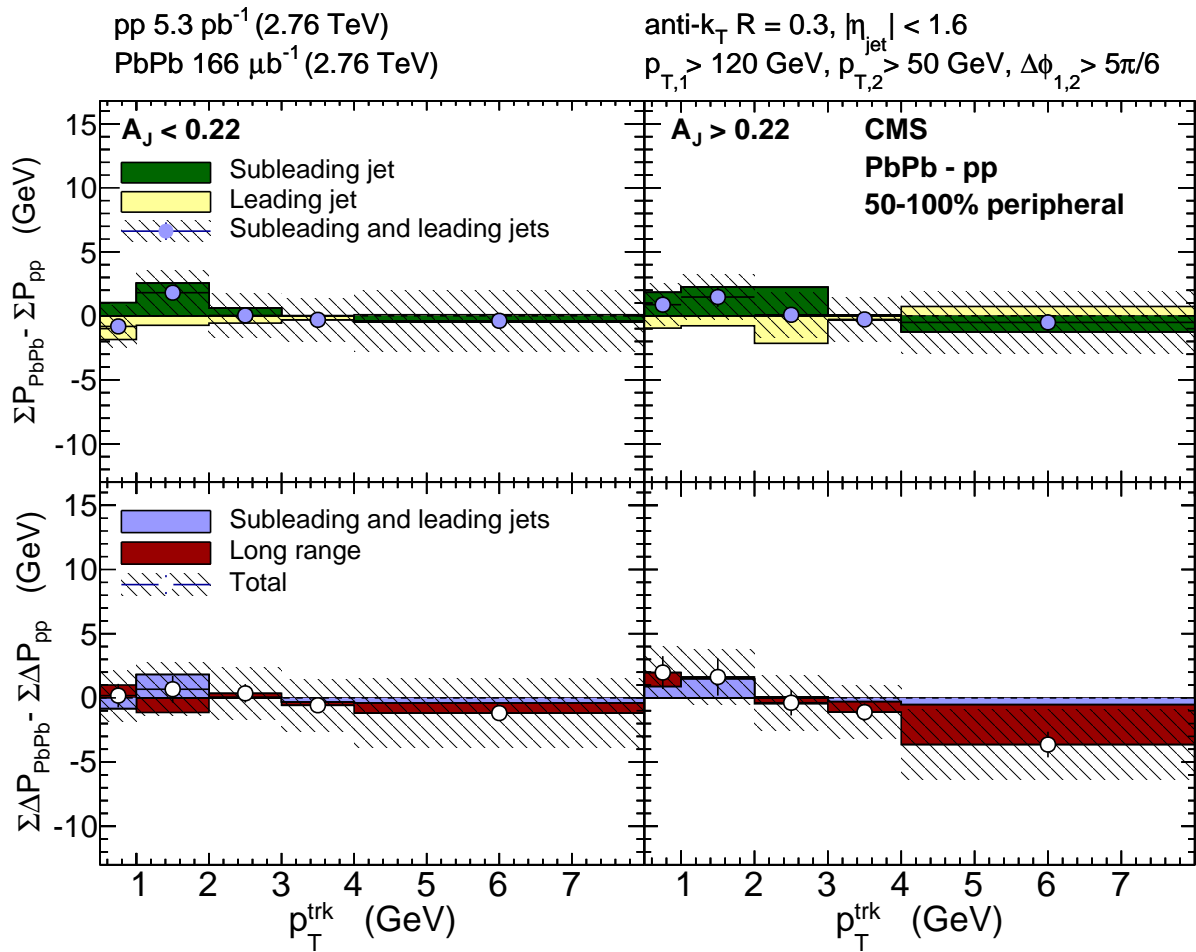


Figure 66. Modifications of jet-hadron correlated transverse momentum in peripheral PbPb collisions with respect to pp reference, integrated  $|\Delta\phi| < \pi/2$ ,  $|\Delta\phi| < 2.5$ . Top row: subleading and leading jet peak PbPb-pp. Bottom row: relative contributions from jet peaks and long-range asymmetry to the double difference PbPb-pp, subleading-leading in total hemisphere transverse momentum.

<sup>1358</sup> **10.5 Theory implications of these results**

## 11 CONCLUSION

## REFERENCES

- [1] O. K. Kalashnikov and V. V. Klimov. Phase transition in the quark-gluon plasma. *Physics Letters B*, 88:328–330, December 1979.
- [2] Edward V. Shuryak. Quantum Chromodynamics and the Theory of Superdense Matter. *Phys. Rept.*, 61:71–158, 1980.
- [3] Siegfried Bethke. World Summary of  $\alpha_s$  (2012). 2012. [Nucl. Phys. Proc. Suppl. 234, 229 (2013)].
- [4] J. D. Bjorken. Highly relativistic nucleus-nucleus collisions: The central rapidity region. *Phys. Rev. D*, 27:140–151, Jan 1983.
- [5] Ulrich W. Heinz and Maurice Jacob. Evidence for a new state of matter: An Assessment of the results from the CERN lead beam program. 2000.
- [6] I. Arsene et al. Quark-gluon plasma and color glass condensate at RHIC? The perspective from the BRAHMS experiment. *Nucl. Phys. A*, 757:1, 2005.
- [7] K. Adcox et al. Formation of dense partonic matter in relativistic nucleus nucleus collisions at RHIC: Experimental evaluation by the PHENIX collaboration. *Nucl. Phys. A*, 757:184, 2005.
- [8] B. B. Back et al. The PHOBOS perspective on discoveries at RHIC. *Nucl. Phys. A*, 757:28, 2005.
- [9] John Adams et al. Experimental and theoretical challenges in the search for the quark gluon plasma: The STAR collaboration’s critical assessment of the evidence from RHIC collisions. *Nucl. Phys. A*, 757:102, 2005.
- [10] J. D. Bjorken. Energy loss of energetic partons in QGP: possible extinction of high  $p_t$  jets in hadron-hadron collisions. FERMILAB-PUB-82-059-THY, 1982.
- [11] David d’Enterria. Jet quenching. *Landolt-Boernstein, Springer-Verlag*, Vol. 1-23A:99, 2010.
- [12] Nestor Armesto. Nuclear shadowing. *J. Phys.*, G32:R367–R394, 2006.
- [13] K. Aamodt. Suppression of Charged Particle Production at Large Transverse Momentum in Central PbPb Collisions at  $\sqrt{s_{\text{NN}}} = 2.76$  TeV. *Phys. Lett. B*, 696:30, 2011.

- 1385 [14] Vardan Khachatryan et al. Charged-particle nuclear modification factors in PbPb and pPb  
 1386 collisions at  $\sqrt{s_{NN}} = 5.02$  TeV. *JHEP*, 04:039, 2017.
- 1387 [15] Georges Aad et al. Measurements of the Nuclear Modification Factor for Jets in Pb+Pb  
 1388 Collisions at  $\sqrt{s_{NN}} = 2.76$  TeV with the ATLAS Detector. *Phys. Rev. Lett.*, 114(7):072302,  
 1389 2015.
- 1390 [16] Vardan Khachatryan et al. Measurement of inclusive jet cross-sections in pp and PbPb colli-  
 1391 sions at  $\sqrt{s_{NN}}=2.76$  TeV. *Phys. Rev. C*, 2016.
- 1392 [17] Serguei Chatrchyan et al. Measurement of jet fragmentation in PbPb and pp collisions at  
 1393  $\sqrt{s_{NN}} = 2.76$  TeV. *Phys. Rev. C*, 90:024908, 2014.
- 1394 [18] Serguei Chatrchyan et al. Modification of jet shapes in PbPb collisions at  $\sqrt{s_{NN}} = 2.76$  TeV.  
 1395 *Phys. Lett. B*, 730:243, 2014.
- 1396 [19] C. Adler et al. Disappearance of back-to-back high- $p_T$  hadron correlations in central Au+Au  
 1397 collisions at  $\sqrt{s_{NN}} = 200$  GeV. *Phys. Rev. Lett.*, 90:082302, 2003.
- 1398 [20] K. Aamodt et al. Particle-yield modification in jet-like azimuthal di-hadron correlations in  
 1399 Pb-Pb collisions at  $\sqrt{s_{NN}} = 2.76$  TeV. *Phys. Rev. Lett.*, 108:092301, 2012.
- 1400 [21] Georges Aad et al. Observation of a Centrality-Dependent Dijet Asymmetry in Lead-Lead  
 1401 Collisions at  $\sqrt{s_{NN}} = 2.76$  TeV with the ATLAS Detector at the LHC. *Phys. Rev. Lett.*,  
 1402 105:252303, 2010.
- 1403 [22] Serguei Chatrchyan et al. Observation and studies of jet quenching in PbPb collisions at  $\sqrt{s_{NN}}$   
 1404 = 2.76 TeV. *Phys. Rev. C*, 84:024906, 2011.
- 1405 [23] Lyndon Evans and Philip Bryant. LHC Machine. *JINST*, 3:S08001, 2008.
- 1406 [24] S. Chatrchyan et al. The CMS experiment at the CERN LHC. *JINST*, 3:S08004, 2008.
- 1407 [25] Tai Sakuma and Thomas McCauley. Detector and event visualization with sketchup at the  
 1408 cms experiment. *Journal of Physics: Conference Series*, 513(2):022032, 2014.
- 1409 [26] Serguei Chatrchyan et al. Description and performance of track and primary-vertex recon-  
 1410 struction with the CMS tracker. *JINST*, 9(10):P10009, 2014.

- 1411 [27] Vardan Khachatryan et al. Performance of photon reconstruction and identification with the  
 1412 CMS detector in proton-proton collisions at  $\sqrt{s_{\text{NN}}} = 8$  TeV. *JINST*, 10:P08010, 2015.
- 1413 [28] Vardan Khachatryan et al. The CMS trigger system. *JINST*, 12:P01020, 2017.
- 1414 [29] CMS Collaboration. Momentum flow relative to dijets in pbpb collisions at 2.76 tev. *CMS*  
 1415 *Analysis Note (Internal)*, AN-14-024, 2014.
- 1416 [30] CMS Internal. Study of high- $p_t$  charged particle suppression in pbpb compared to pp collisions  
 1417 at 5.02 tev. 2016.
- 1418 [31] Gavin P. Salam. Towards Jetography. *Eur. Phys. J.*, C67:637–686, 2010.
- 1419 [32] Matteo Cacciari, Gavin P. Salam, and Gregory Soyez. The anti- $k_t$  jet clustering algorithm.  
 1420 *JHEP*, 04:063, 2008.
- 1421 [33] Matteo Cacciari, Gavin P. Salam, and Gregory Soyez. FastJet user manual. *Eur. Phys. J. C*,  
 1422 72:1896, 2012.
- 1423 [34] Olga Kodolova, I. Vardanian, A. Nikitenko, and A. Oulianov. The performance of the jet  
 1424 identification and reconstruction in heavy ions collisions with CMS detector. *Eur. Phys. J. C*,  
 1425 50:117, 2007.
- 1426 [35] Serguei Chatrchyan et al. Studies of jet quenching using isolated-photon+jet correlations in  
 1427 PbPb and pp collisions at  $\sqrt{s_{\text{NN}}} = 2.76$  TeV. *Phys. Lett. B*, 718:773, 2013.
- 1428 [36] Serguei Chatrchyan et al. Measurement of jet fragmentation into charged particles in pp and  
 1429 PbPb collisions at  $\sqrt{s_{\text{NN}}} = 2.76$  TeV. *JHEP*, 10:087, 2012.
- 1430 [37] CMS. Identification and Filtering of Uncharacteristic Noise in the CMS Hadron Calorimeter.  
 1431 *JINST*, 5:T03014, 2010.
- 1432 [38] Torbjorn Sjöstrand, Stephen Mrenna, and Peter Skands. PYTHIA 6.4 physics and manual.  
 1433 *JHEP*, 05:026, 2006.
- 1434 [39] S. Agostinelli et al. GEANT4—a simulation toolkit. *Nucl. Instrum. and Methods A*, 506:250,  
 1435 2003.

- 1436 [40] I. P. Lokhtin and A. M. Snigirev. A model of jet quenching in ultrarelativistic heavy ion  
1437 collisions and high- $p_T$  hadron spectra at RHIC. *Eur. Phys. J. C*, 45:211, 2006.
- 1438 [41] Vardan Khachatryan et al. Measurement of transverse momentum relative to dijet systems in  
1439 PbPb and pp collisions at  $\sqrt{s_{\text{NN}}} = 2.76$  TeV. *JHEP*, 01:6, 2016.
- 1440 [42] S. Chatrchyan et al. Azimuthal anisotropy of charge particles at high transvere momenta in  
1441 pb-pb collisions at  $\sqrt{s_{\text{NN}}} = 2.76$  TeV. *Phys. Rev. Lett.*, 109:022301, 2012.
- 1442 [43] Serguei Chatrchyan et al. Centrality dependence of dihadron correlations and azimuthal  
1443 anisotropy harmonics in PbPb collisions at  $\sqrt{s_{\text{NN}}} = 2.76$  TeV. *Eur. Phys. J.*, C72:2012,  
1444 2012.
- 1445 [44] K. Aamodt et al. Harmonic decomposition of two-particle angular correlations in Pb-Pb  
1446 collisions at  $\sqrt{s_{\text{NN}}} = 2.76$  TeV. *Phys. Lett. B*, 708:249, 2012.
- 1447 [45] Serguei Chatrchyan et al. Long-range and short-range dihadron angular correlations in central  
1448 PbPb collisions at a nucleon-nucleon center of mass energy of 2.76 TeV. *JHEP*, 07:076, 2011.

## APPENDICES

### 1450 A Jet kinematics

1451 The following sections summarize jet kinematics for inclusive jets and dijets at 2.76 TeV, for inclu-  
 1452 sive jets at 5.02 TeV, and for dijets in each asymmetry class at 2.76 TeV.

#### 1453 A.1 Jet kinematics at 2.76 TeV

1454 The kinematic observables of jets in pp and PbPb 2.76 TeV events (solid markers) are compared  
 1455 with Monte Carlo (hatched marks). All spectra have been normalized to unity. Comparing the jet  
 1456 spectra observed in PbPb data (pp data) and in PYTHIA+HYDJET (PYTHIA) samples, a reasonable  
 1457 agreement in the overall shape is found.

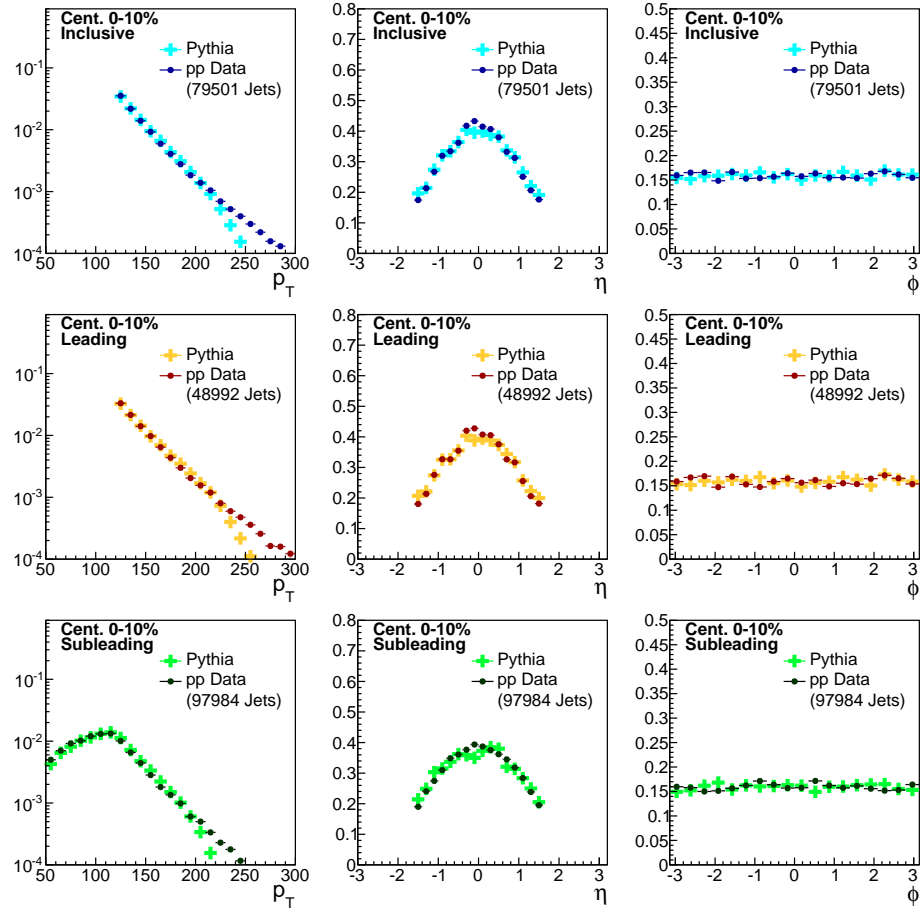


Figure 67. Distribution of transverse momentum, pseudorapidity, and azimuthal distribution of all jet selections for Pythia data compared to PYTHIA simulation.

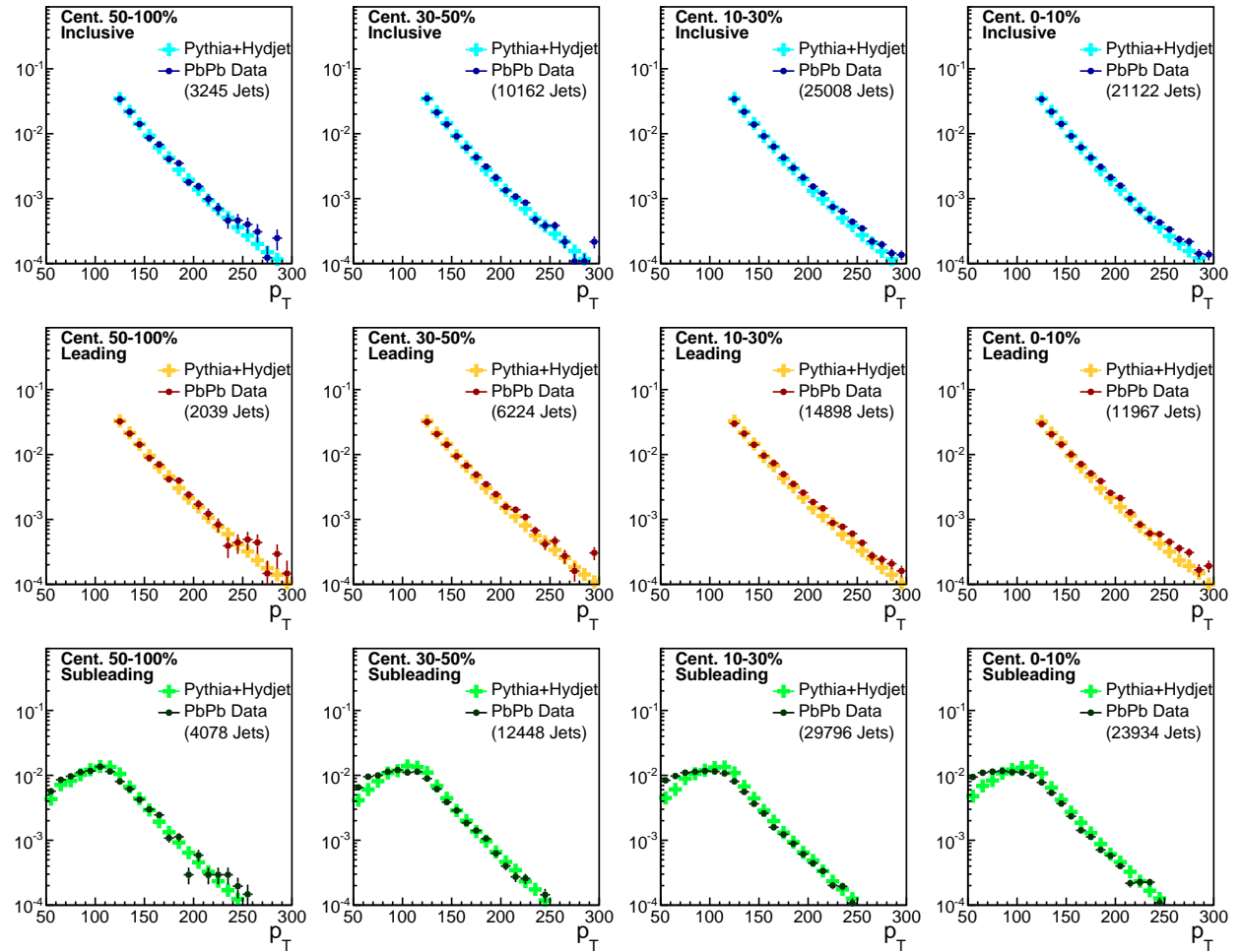


Figure 68. Transverse momentum distribution of all jet selections for PbPb data at 2.76 TeV compared to PYTHIA+HYDJET simulation.

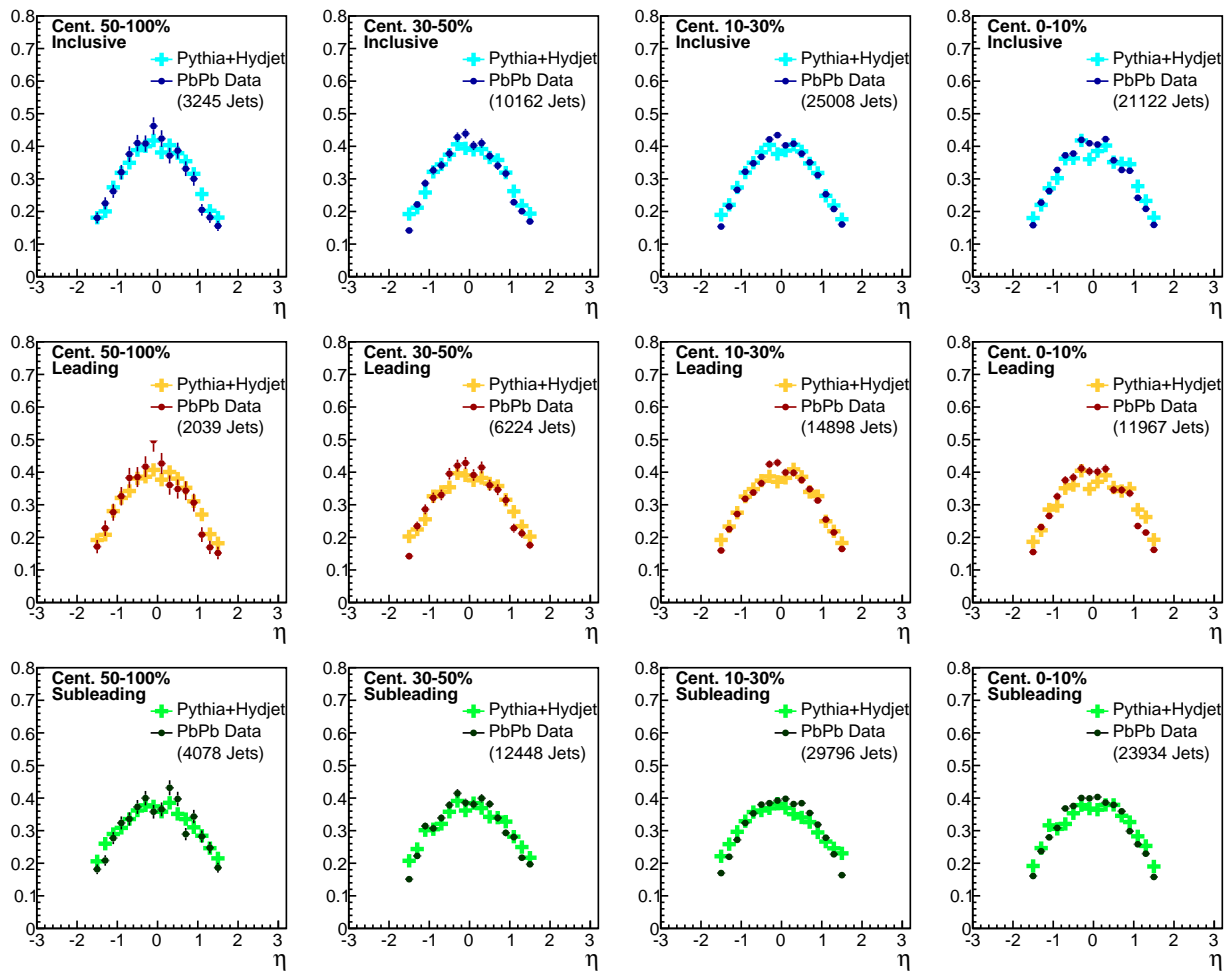


Figure 69. Pseudorapidity distribution of all jet selections for PbPb data at 2.76 TeV compared to PYTHIA + HYDJET simulation.

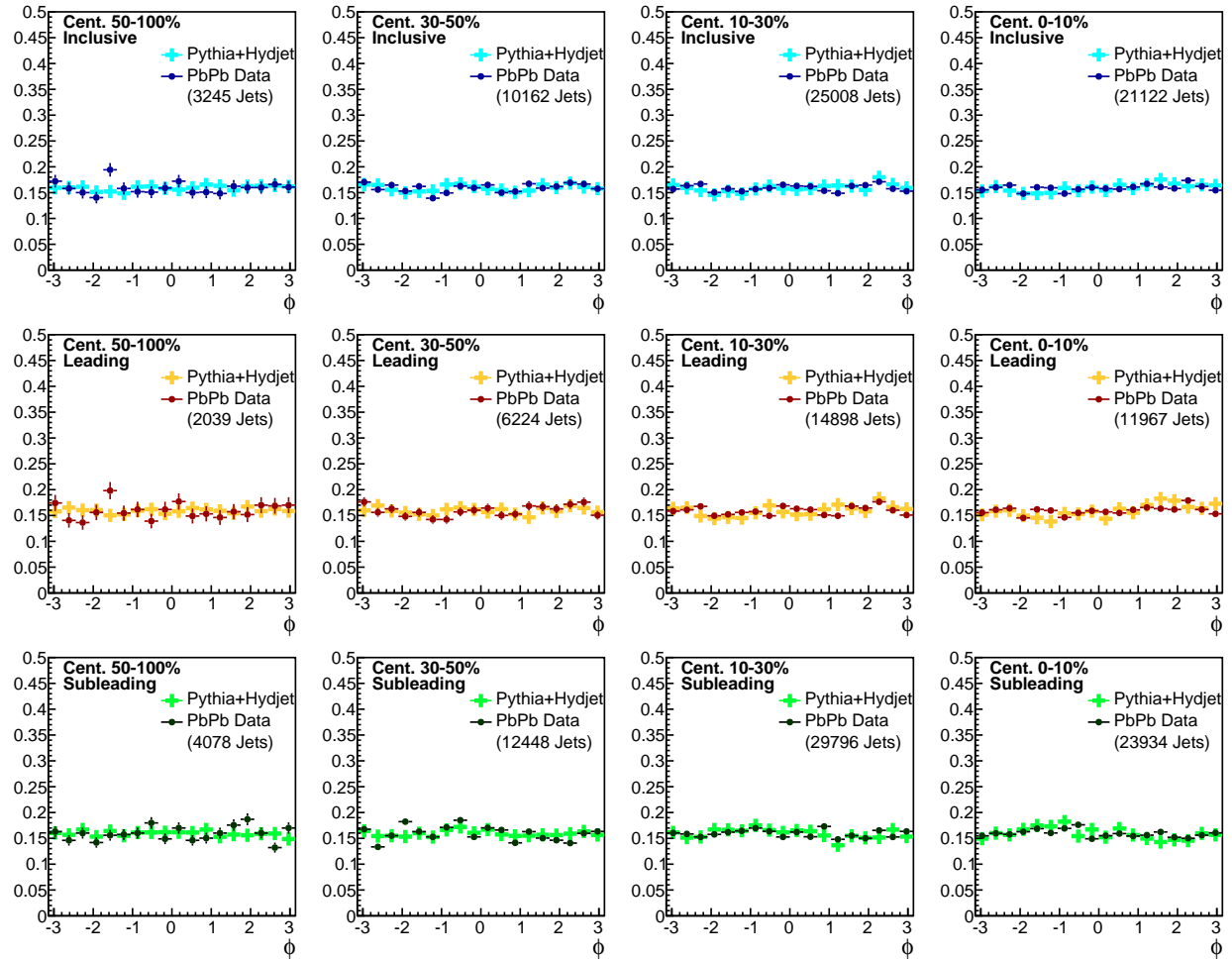


Figure 70. Azimuthal angle distribution of all jet selections for PbPb data at 2.76 TeV compared to PYTHIA+HYDJET simulation for each collision centrality bin.

1458 **A.2 Inclusive jet kinematics at 5.02 TeV**

1459 Jet  $p_T$ ,  $\eta$ , and  $\phi$  distributions for 5.02 TeV data, comparing PbPb data to PYTHIA+HYDJET and  
 1460 pp data to PYTHIA simulation.

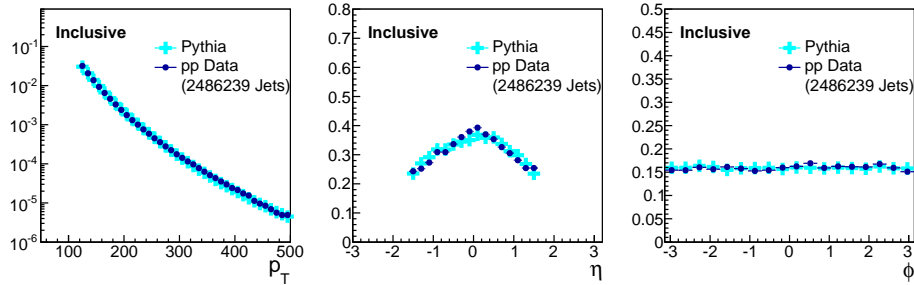


Figure 71. Distribution of pseudorapidity distribution of all jet selections for PbPb data compared to PYTHIA+HYDJet simulation for each collision centrality bin.

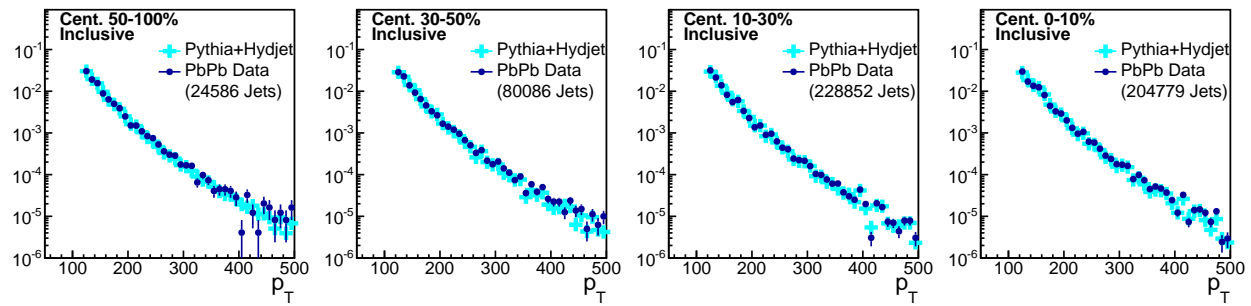


Figure 72. Transverse momentum distribution for PbPb data compared to PYTHIA+HYDJet simulation for each collision centrality bin.

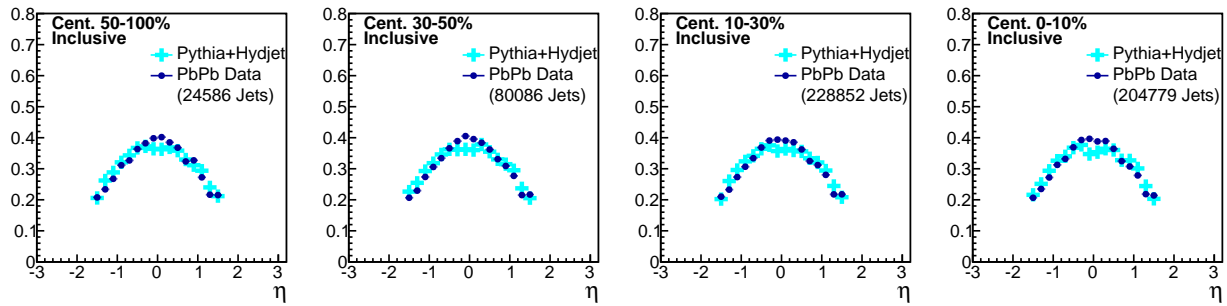


Figure 73. Jet  $\eta$  distribution for PbPb data compared to PYTHIA+HYDJet simulation for each collision centrality bin.

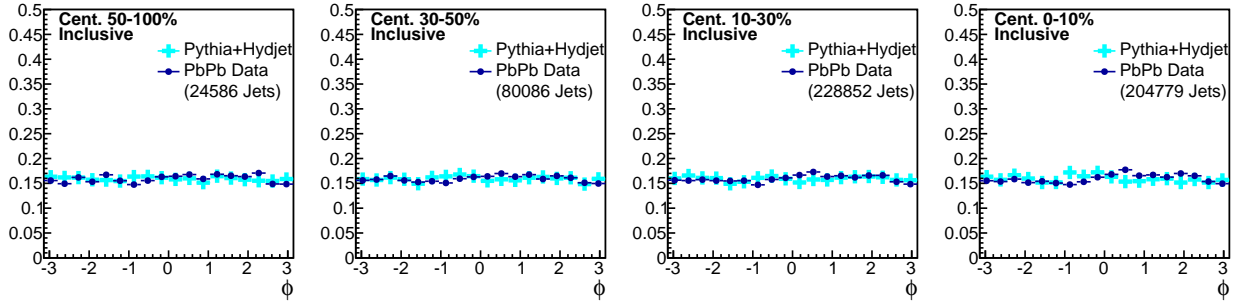


Figure 74. Jet  $\phi$  distribution for PbPb data compared to PYTHIA+HYDJET simulation for each collision centrality bin.

<sup>1461</sup> **A.3 Dijet kinematics in asymmetry classes at 2.76 TeV**

<sup>1462</sup> In the figures below, jet transverse momentum, pseudorapidity, and azimuth are shown for our  $A_J$ -  
<sup>1463</sup> inclusive sample, compared to each  $A_J$  selection in our analysis. Note that  $A_J$ -selection primarily  
<sup>1464</sup> affects the subleading jet spectrum, while the leading jet spectrum is nearly unchanged. Jet  $\eta$  and  
<sup>1465</sup> jet  $\phi$  exhibit no significant  $A_J$ -dependence for leading or subleading jets. Distributions are shown  
<sup>1466</sup> first for pp, and then for PbPb data at 2.76 TeV.

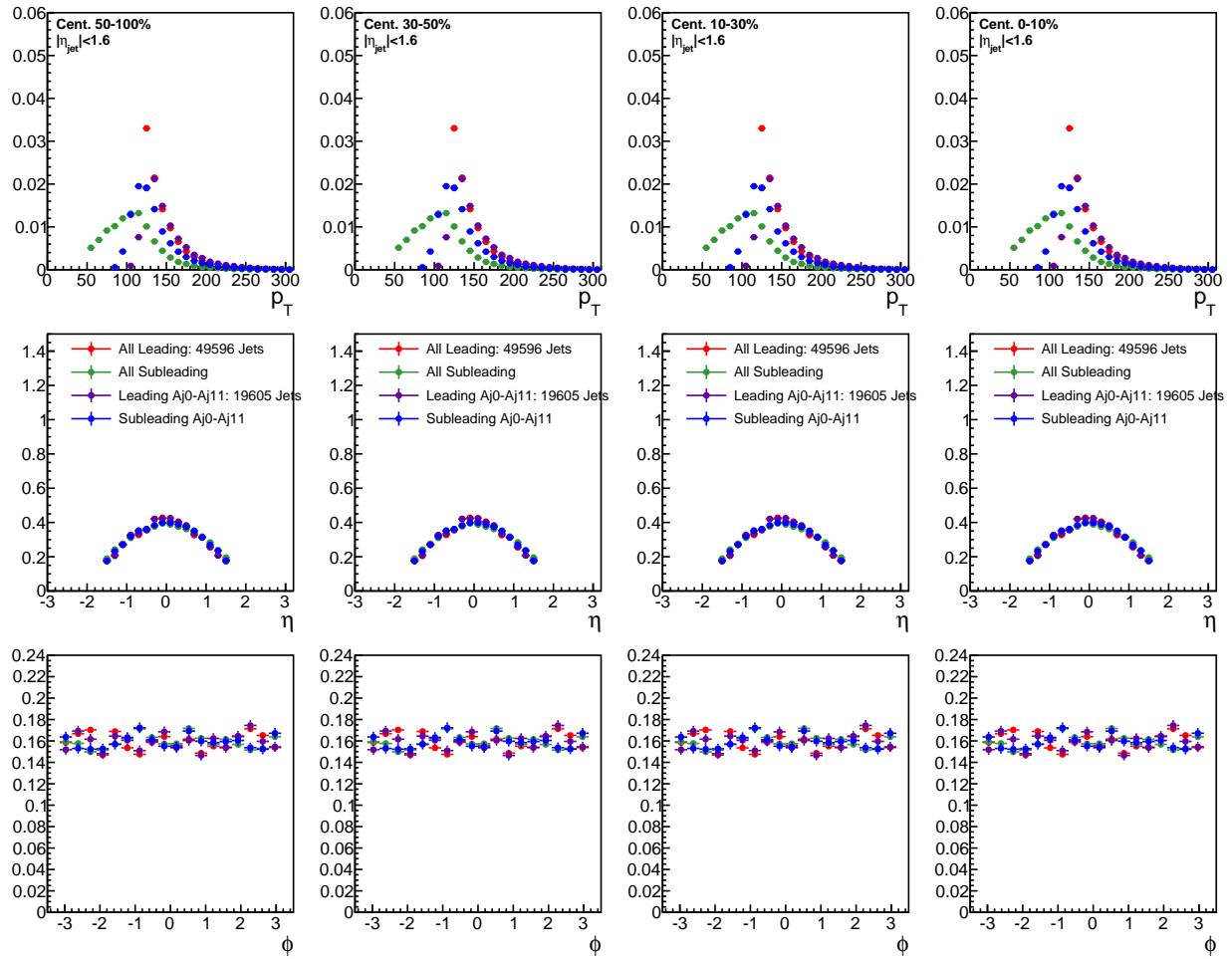


Figure 75. Jet  $p_T$ ,  $\eta$ , and  $\phi$  for all pp dijets and for pp dijets with  $A_J$ :  $0 < A_J < 0.11$ .

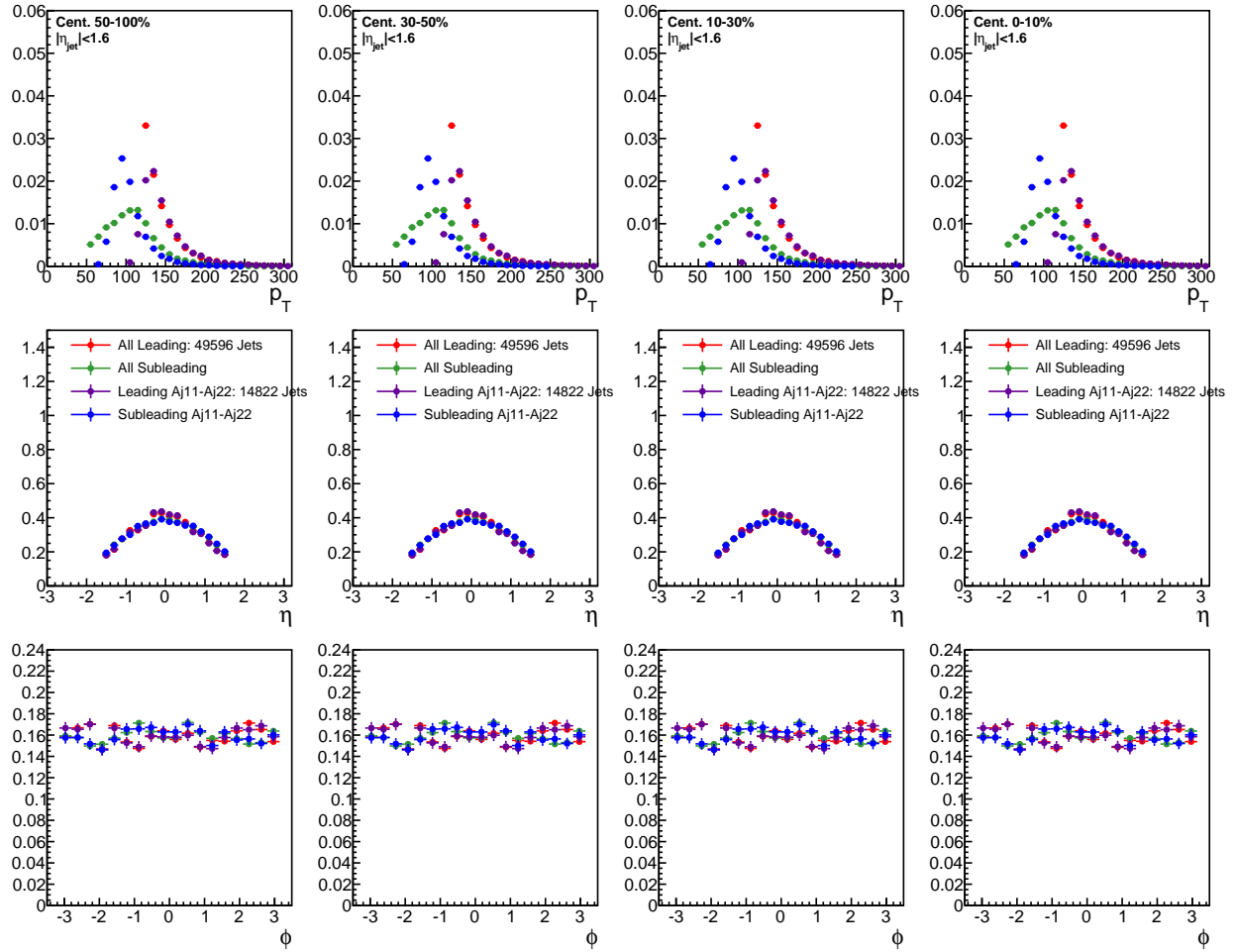


Figure 76. Jet  $p_T$ ,  $\eta$ , and  $\phi$  for all pp dijets and for pp dijets with  $A_J$ :  $0.11 < A_J < 0.22$ .

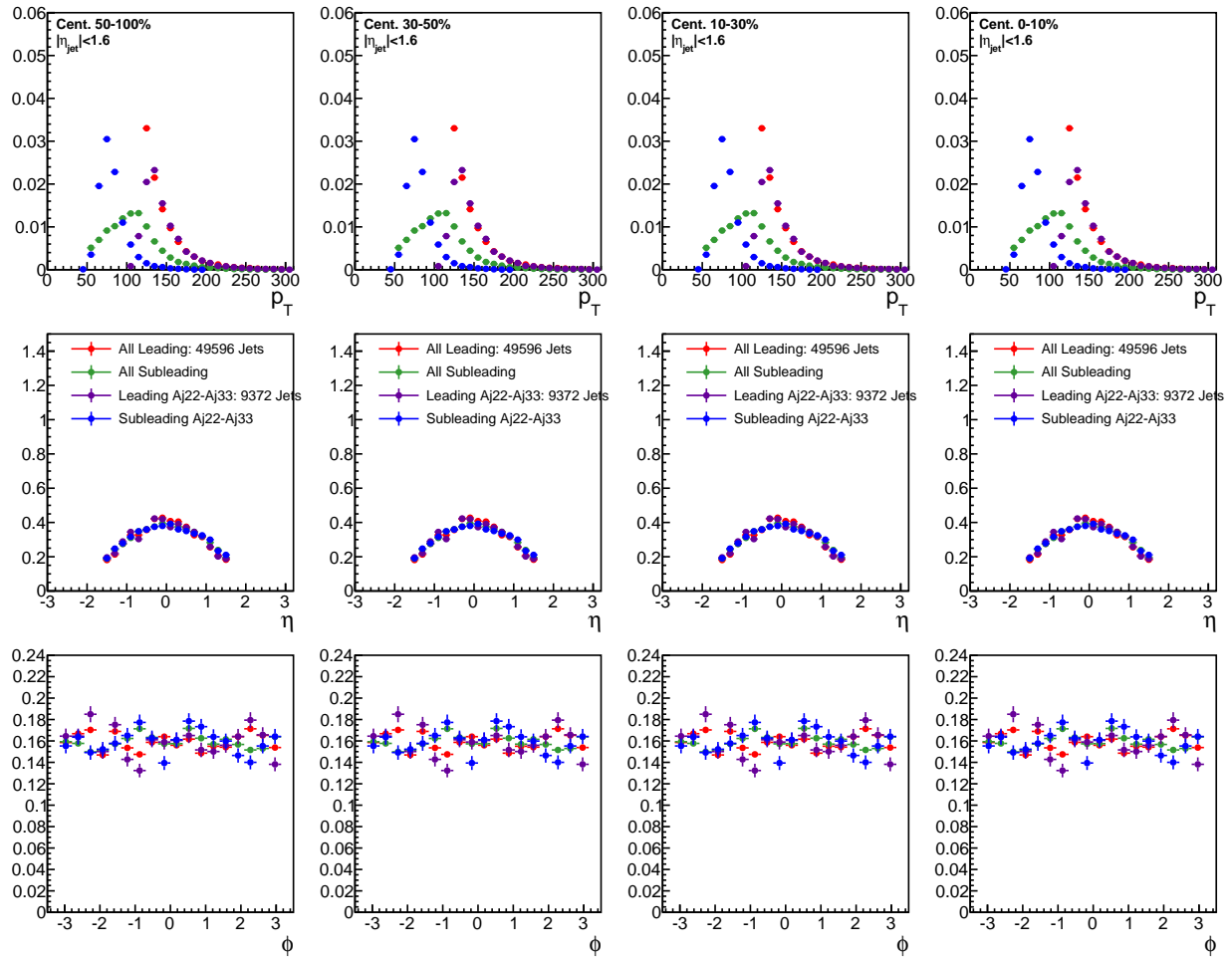


Figure 77. Jet  $p_T$ ,  $\eta$ , and  $\phi$  for all pp dijets and for pp dijets with  $A_J$ :  $0.22 < A_J < 0.33$ .

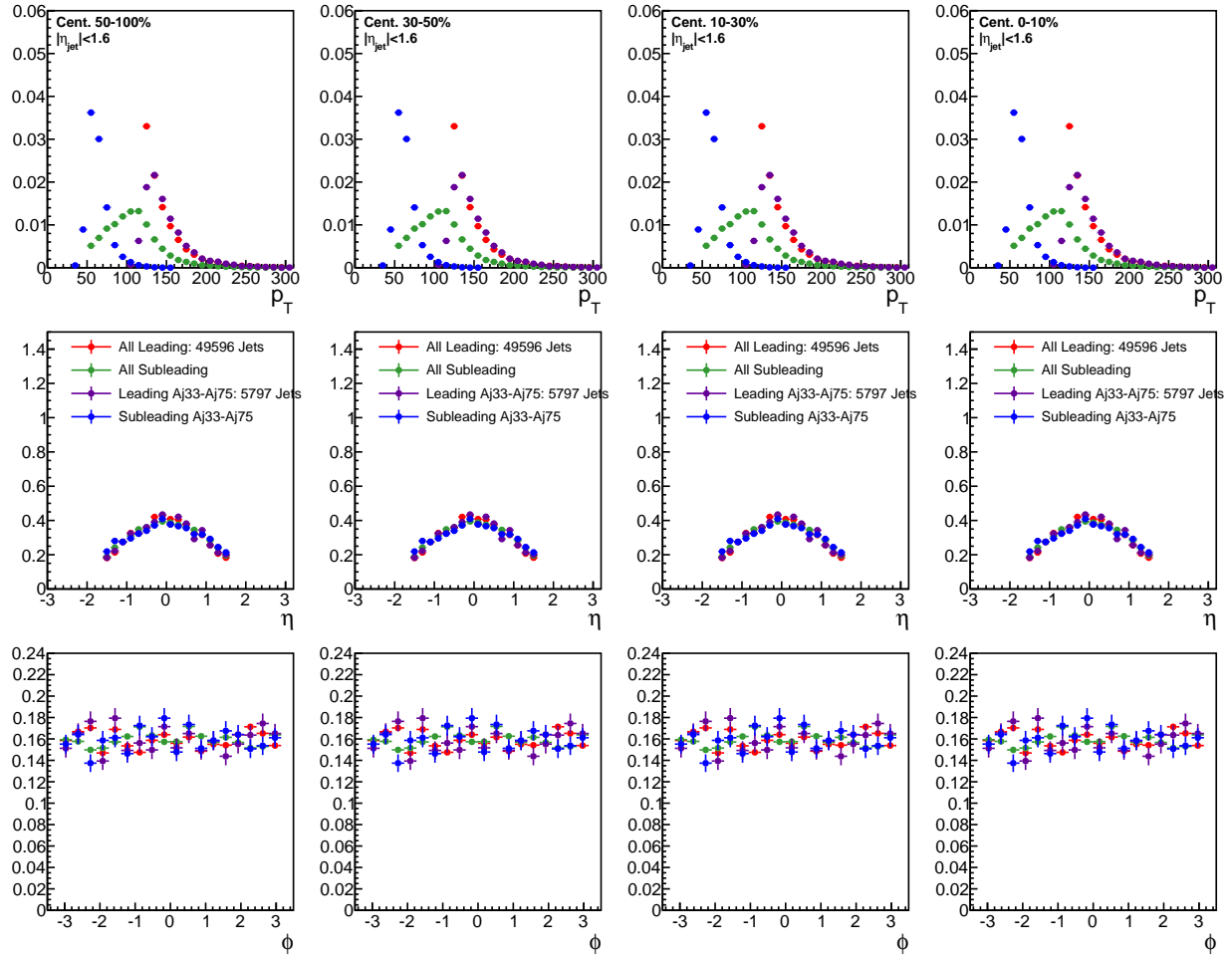


Figure 78. Jet  $p_T$ ,  $\eta$ , and  $\phi$  for all pp dijets and for pp dijets with  $A_J$ :  $A_J > 0.33$ .

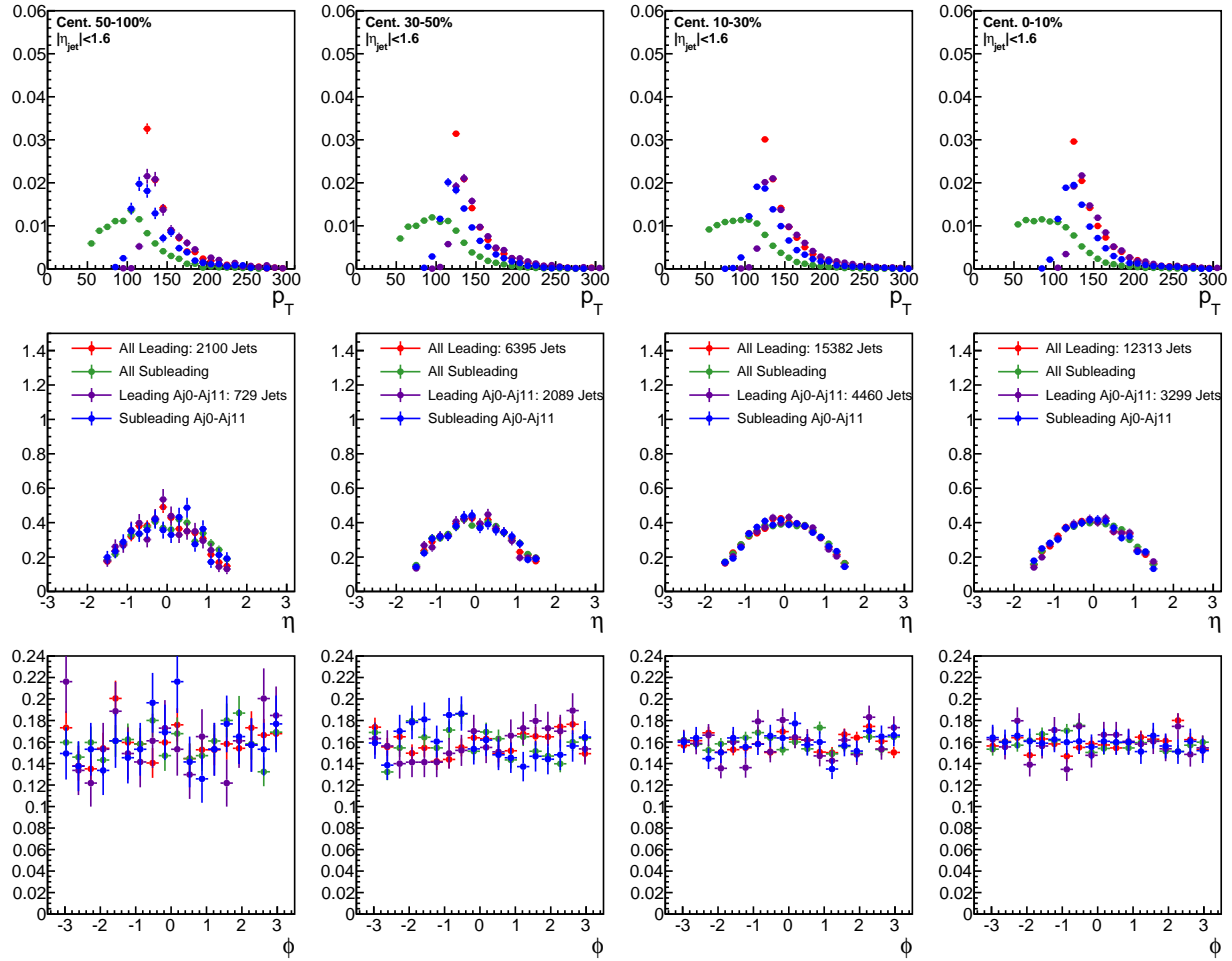


Figure 79. Jet  $p_T$ ,  $\eta$ , and  $\phi$  for all PbPb dijets and for PbPb dijets with  $0 < A_J < 0.11$ .

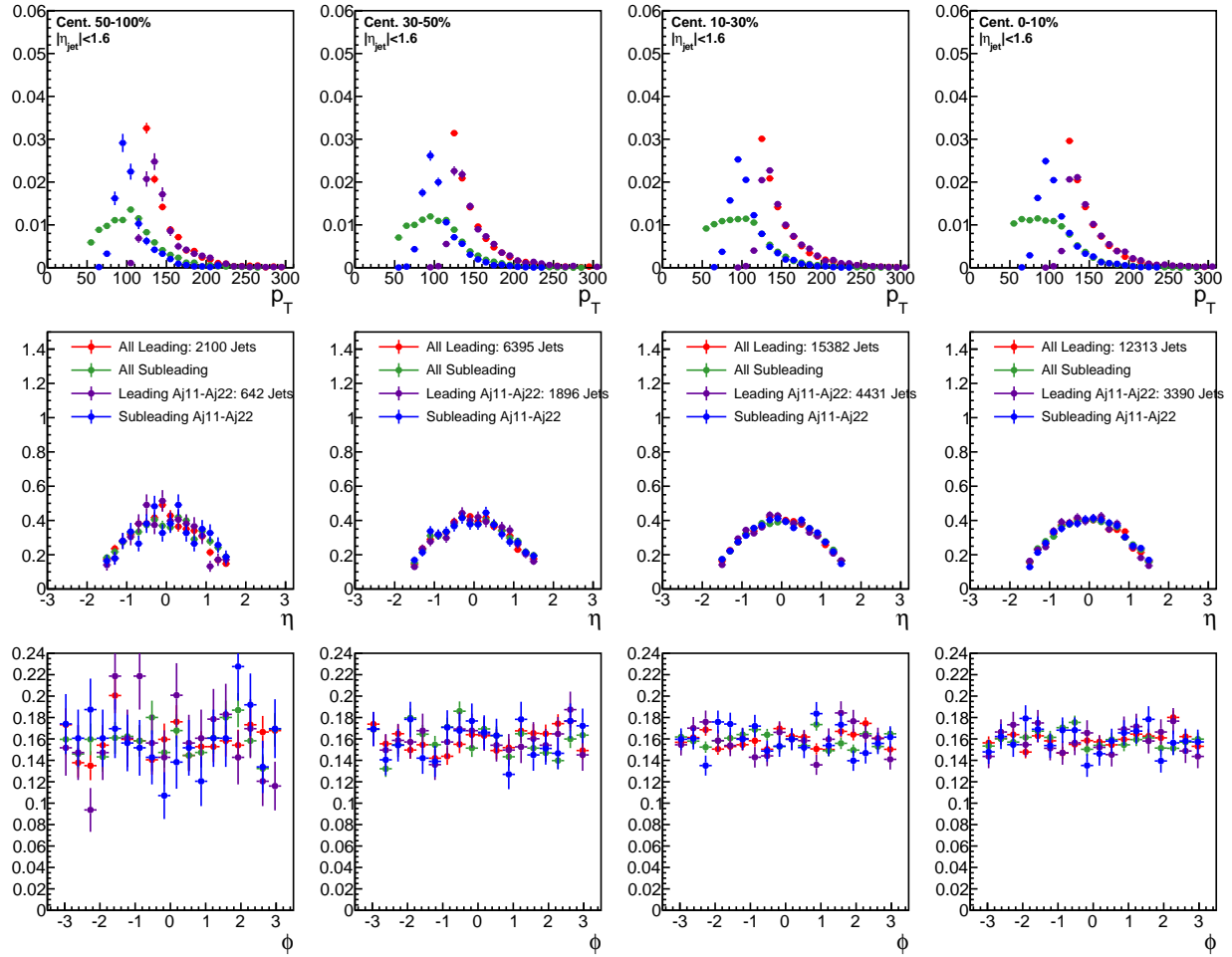


Figure 80. Jet  $p_T$ ,  $\eta$ , and  $\phi$  for all PbPb dijets and for PbPb dijets with  $0.11 < A_J < 0.22$ .

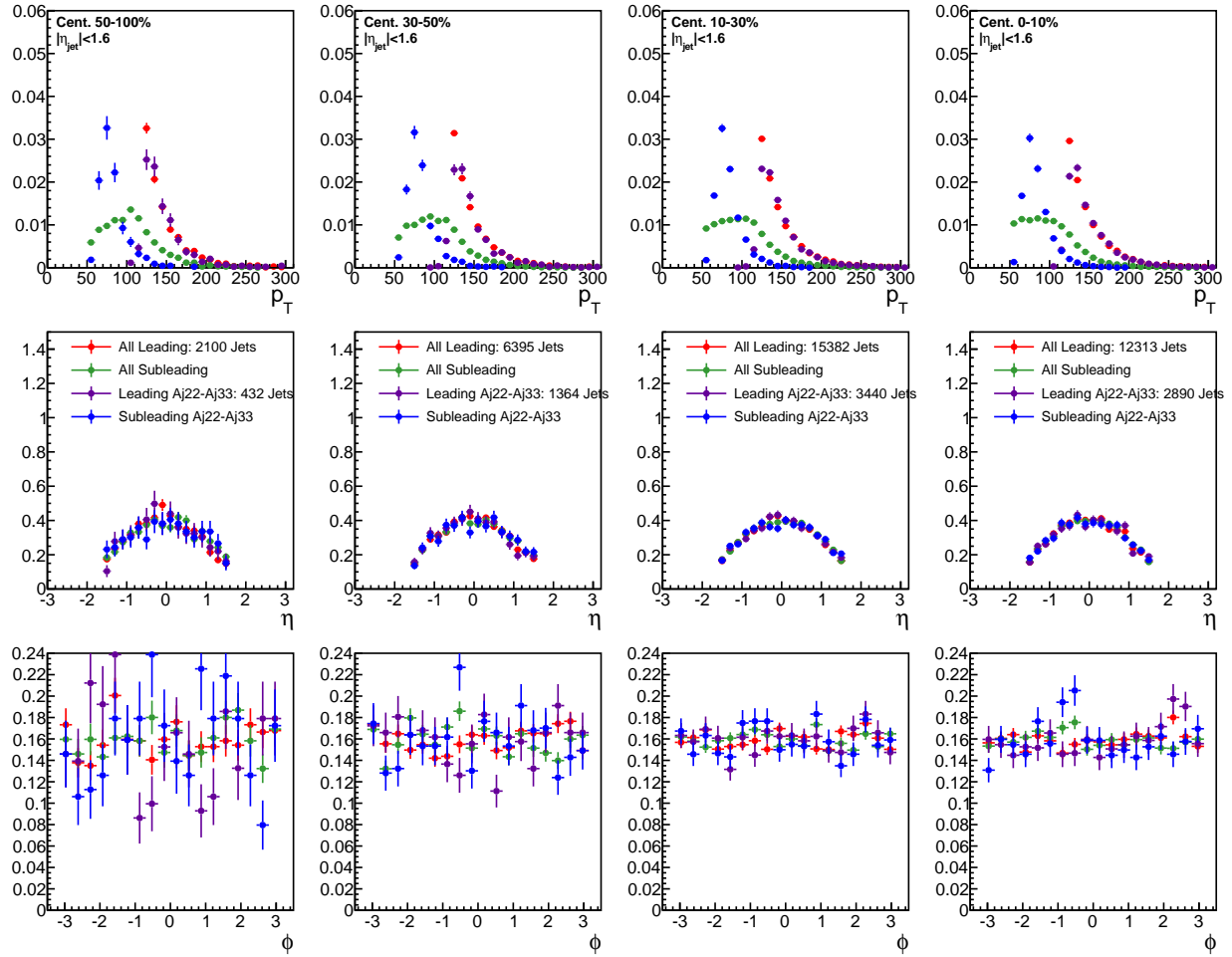


Figure 81. Jet  $p_T$ ,  $\eta$ , and  $\phi$  for all PbPb dijets and for PbPb dijets with  $0.22 < A_J < 0.33$ .

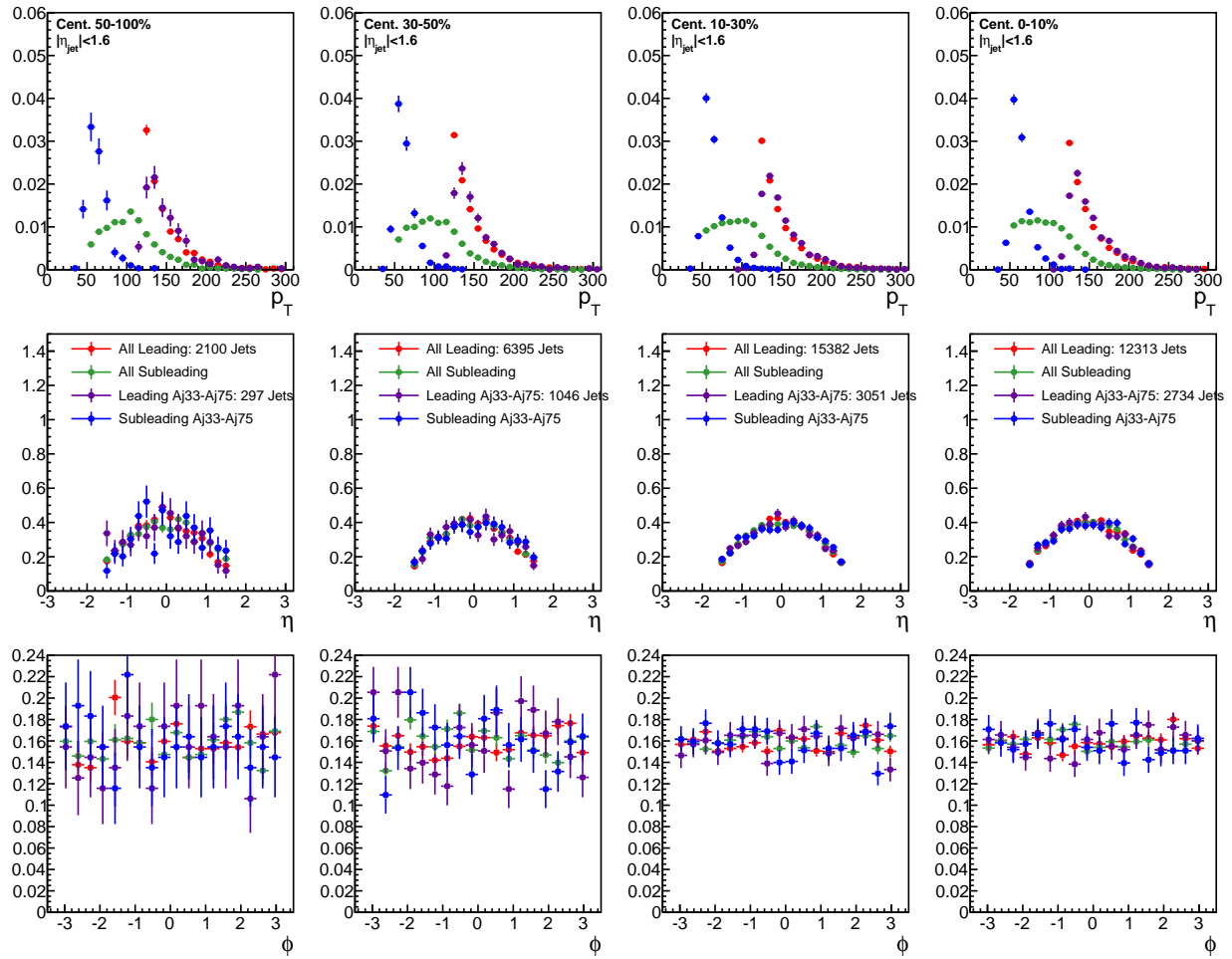


Figure 82. Jet  $p_T$ ,  $\eta$ , and  $\phi$  for all PbPb dijets and for PbPb dijets with  $A_J > 0.33$ .

1467 **B Background fitting details**

1468 Figures 83-86 show the two steps of fits involved in modeling the background distribution in  
 1469  $\Delta\phi$ , as discussed in section 9.3.

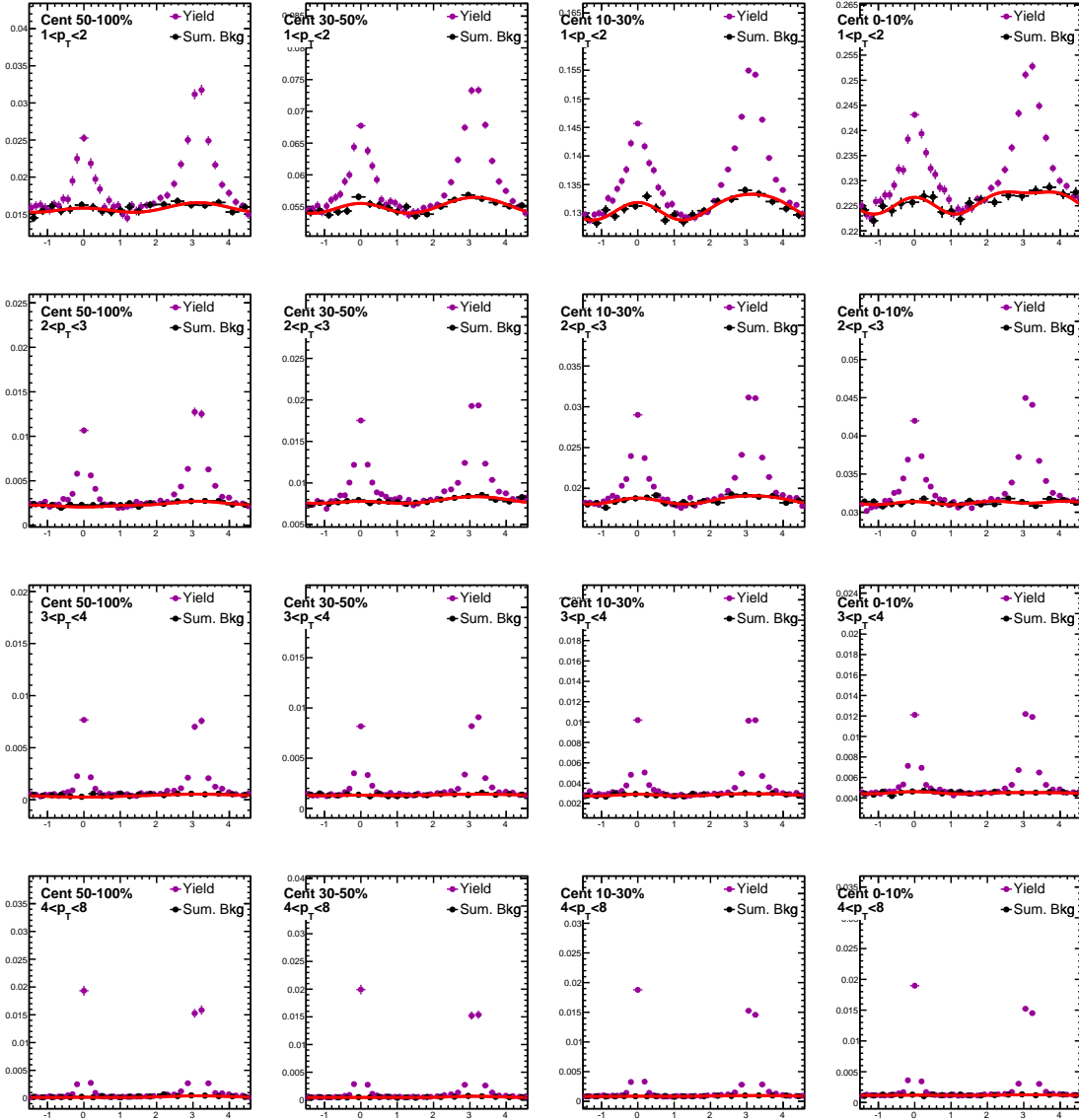


Figure 83. Dijet combined background  $\Delta\phi$  distributions, estimated by projection over the region  $1.5 < |\Delta\eta| < 3.0$ . Here the "near-side" region  $-\frac{\pi}{2} < \Delta\phi < \frac{\pi}{2}$  is taken from the leading jet correlation, while the "away-side"  $-\frac{\pi}{2} < \Delta\phi < \frac{\pi}{2}$  is taken from the subleading jet correlation. The resulting combined background distribution is fit with the function  $B^{dijet}(\Delta\phi) = B_0(1 + 2V_1\cos(\Delta\phi) + 2V_2\cos(2\Delta\phi) + 2V_3\cos(3\Delta\phi))$ .

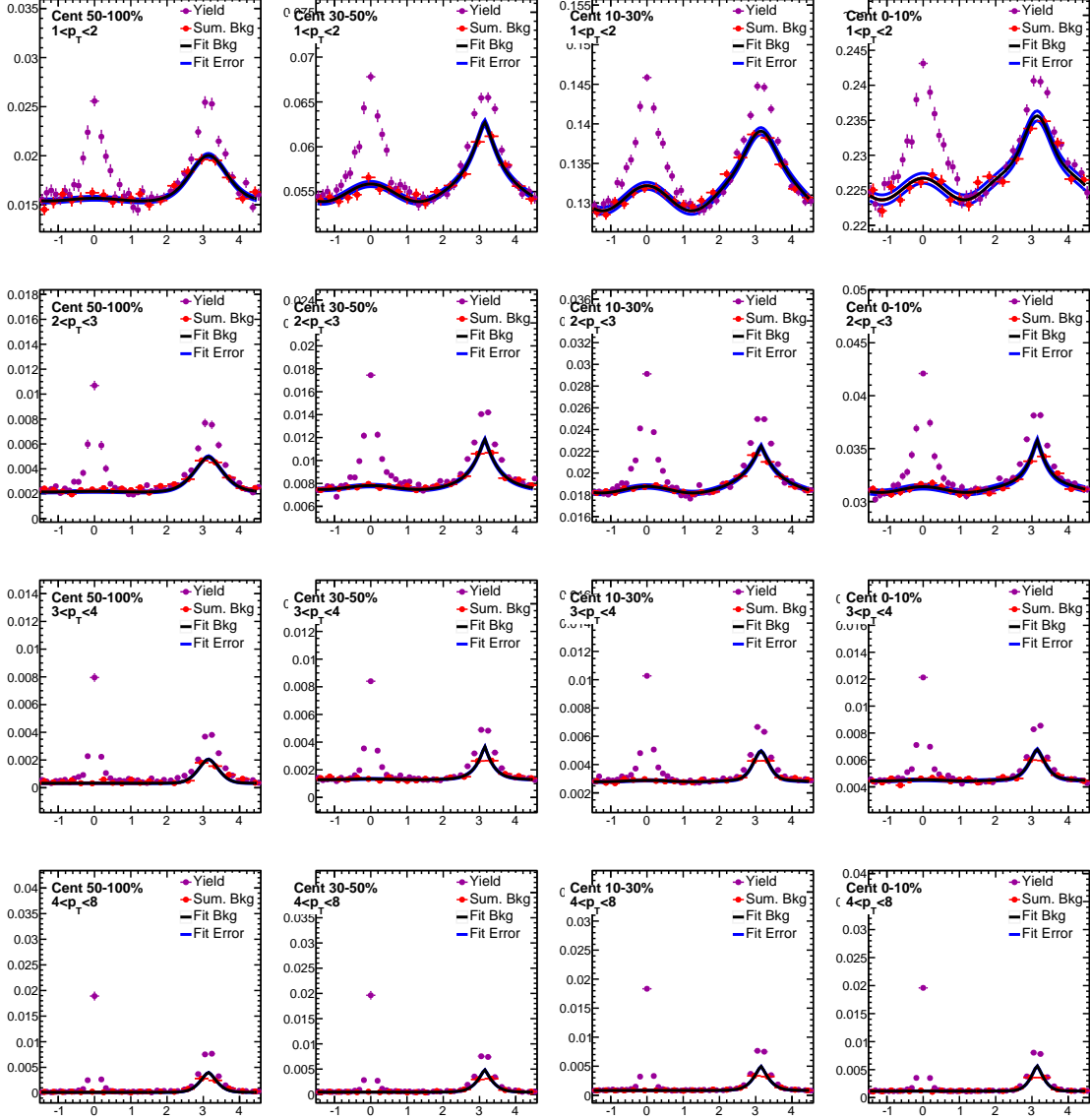


Figure 84. Background leading jet  $\Delta\phi$  distributions, estimated by projection over the region  $1.5 < |\Delta\eta| < 3.0$ , is fit as shown. The 2D background distribution is estimated by propagating the black fit line in  $\Delta\eta$ , with uncertainty assigned by varying fit parameters by the appropriate fit error as shown in the blue error band.

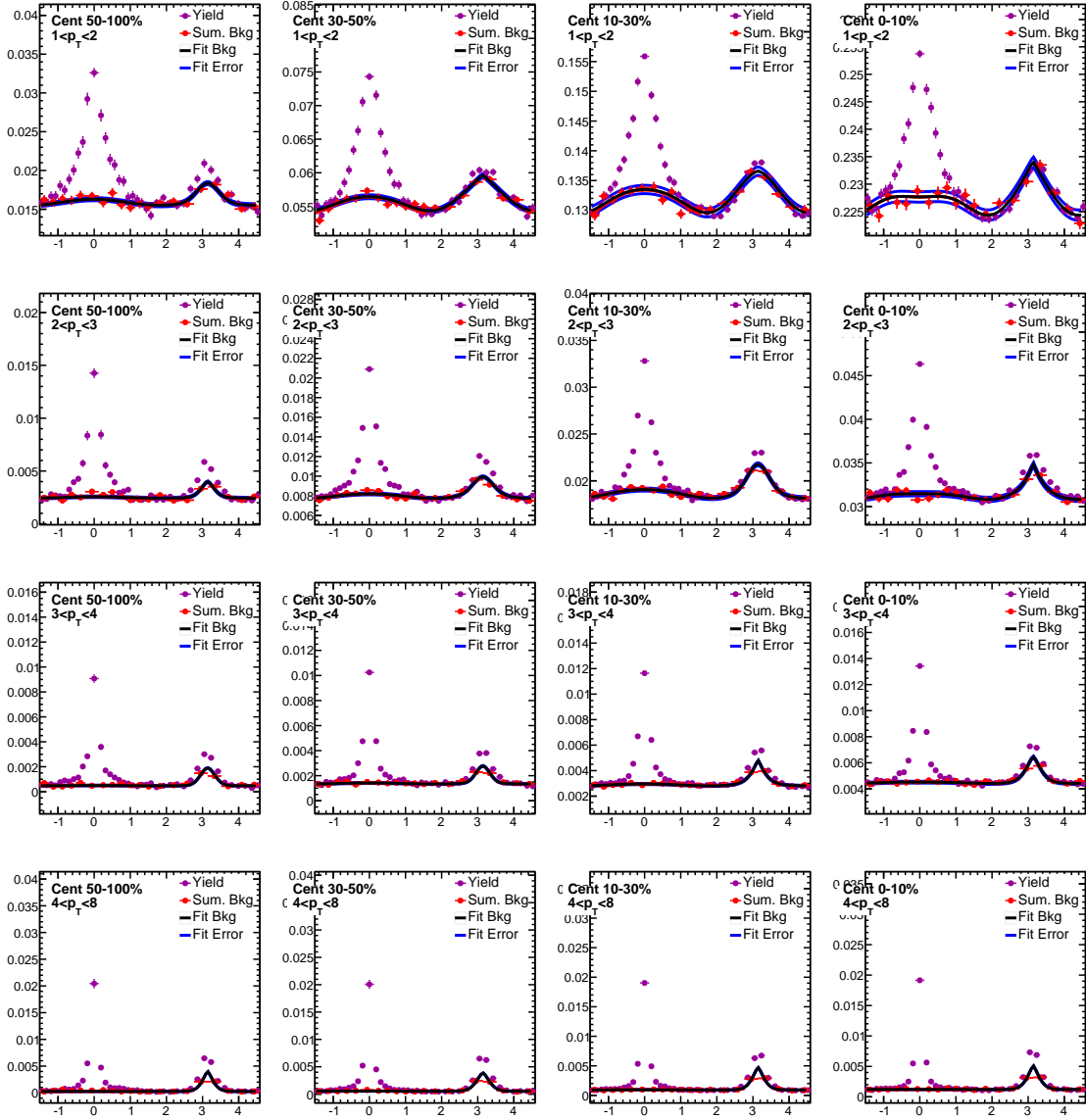


Figure 85. Background subleading jet  $\Delta\phi$  distributions, estimated by projection over the region  $1.5 < |\Delta\eta| < 3.0$ , is fit as shown. The 2D background distribution is estimated by propagating the black fit line in  $\Delta\eta$ , with uncertainty assigned by varying fit parameters by the appropriate fit error as shown in the blue error band.

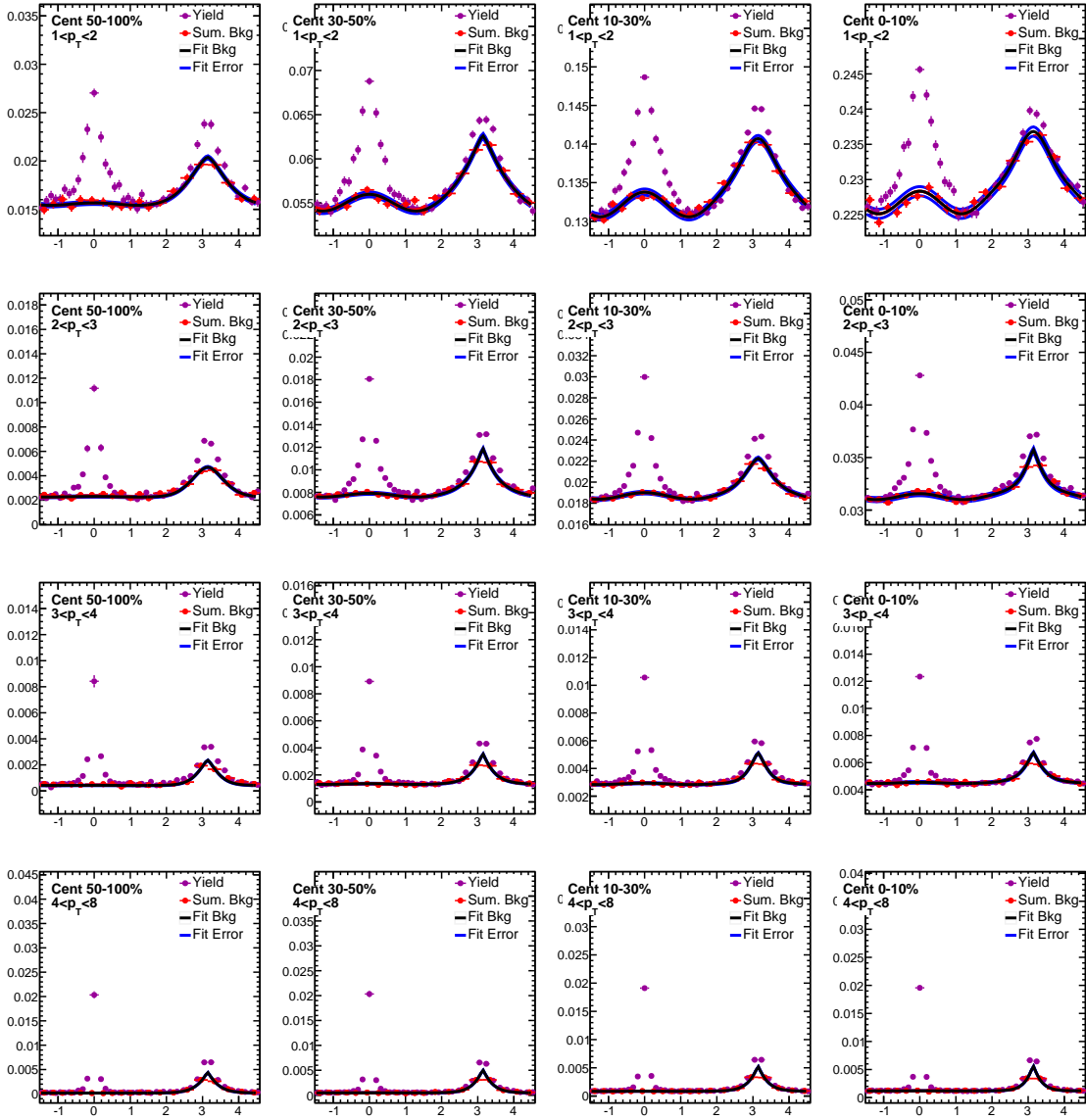


Figure 86. Background inclusive jet  $\Delta\phi$  distributions, estimated by projection over the region  $1.5 < |\Delta\eta| < 3.0$ , is fit as shown. The 2D background distribution is estimated by propagating the black fit line in  $\Delta\eta$ , with uncertainty assigned by varying fit parameters by the appropriate fit error as shown in the blue error band.

1470 **C Pair acceptance and event decomposition systematic uncertainties**

1471 Figure 87 illustrates the estimation of pair-acceptance uncertainty, determined by considering the  
 1472 sideband asymmetry in the  $\Delta\eta$  distributions of background subtracted yield.

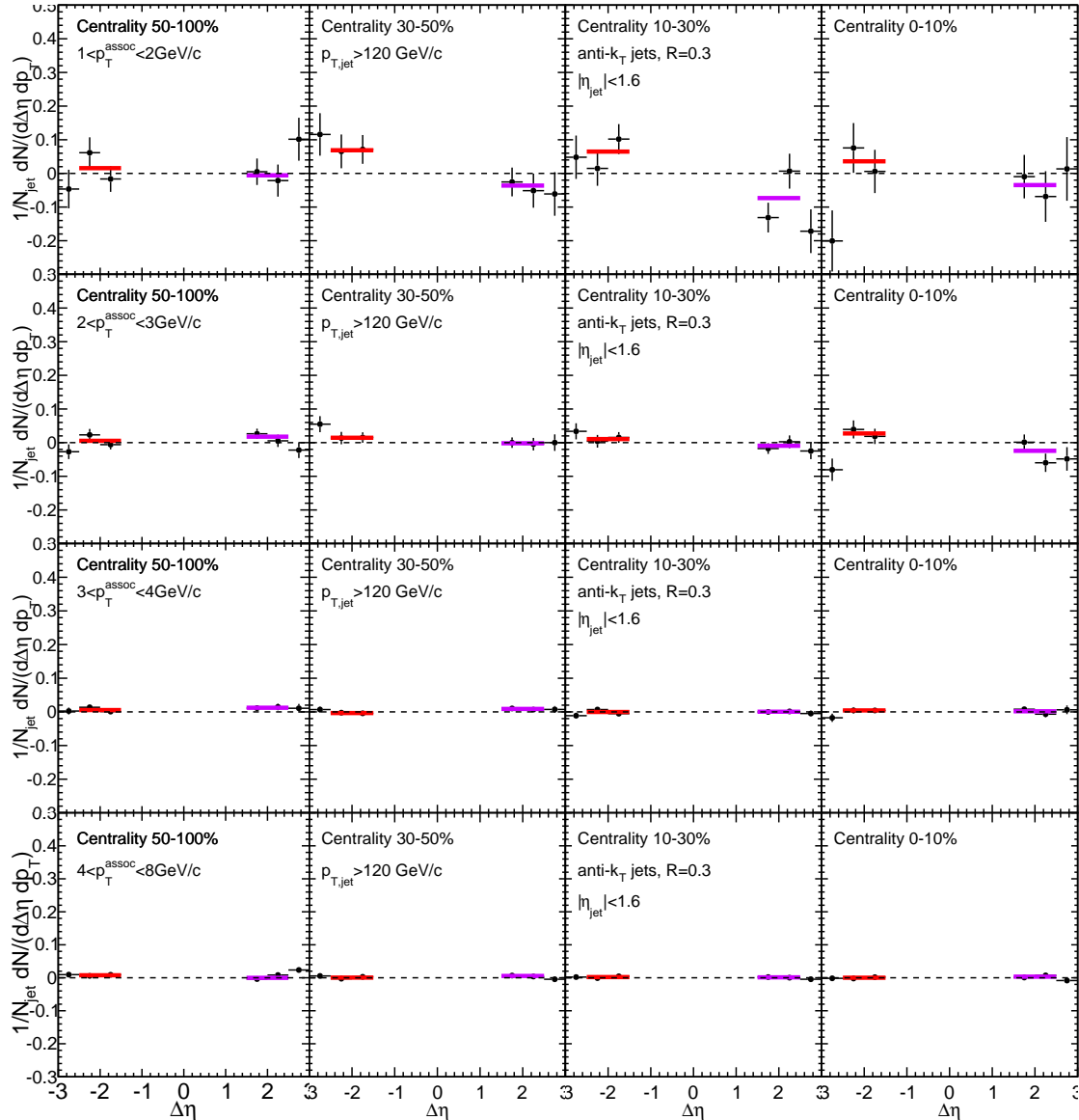


Figure 87. Background-subtracted inclusive jet  $\Delta\eta$  distribution is shown for sideband region  $1.5 < |\Delta\eta| < 3.0$  only. Each side is fit separately with a horizontal line, and the greater deviation from zero is assigned as systematic uncertainty arising from the pair-acceptance correction.

1473 Figure 88 illustrates the background-subtraction systematic uncertainty estimation: the average  
 1474 content of the two  $1.5 < \Delta\eta < 2.0$  bins is assigned as systematic uncertainty for each  $p_T$  and  
 1475 centrality bin.

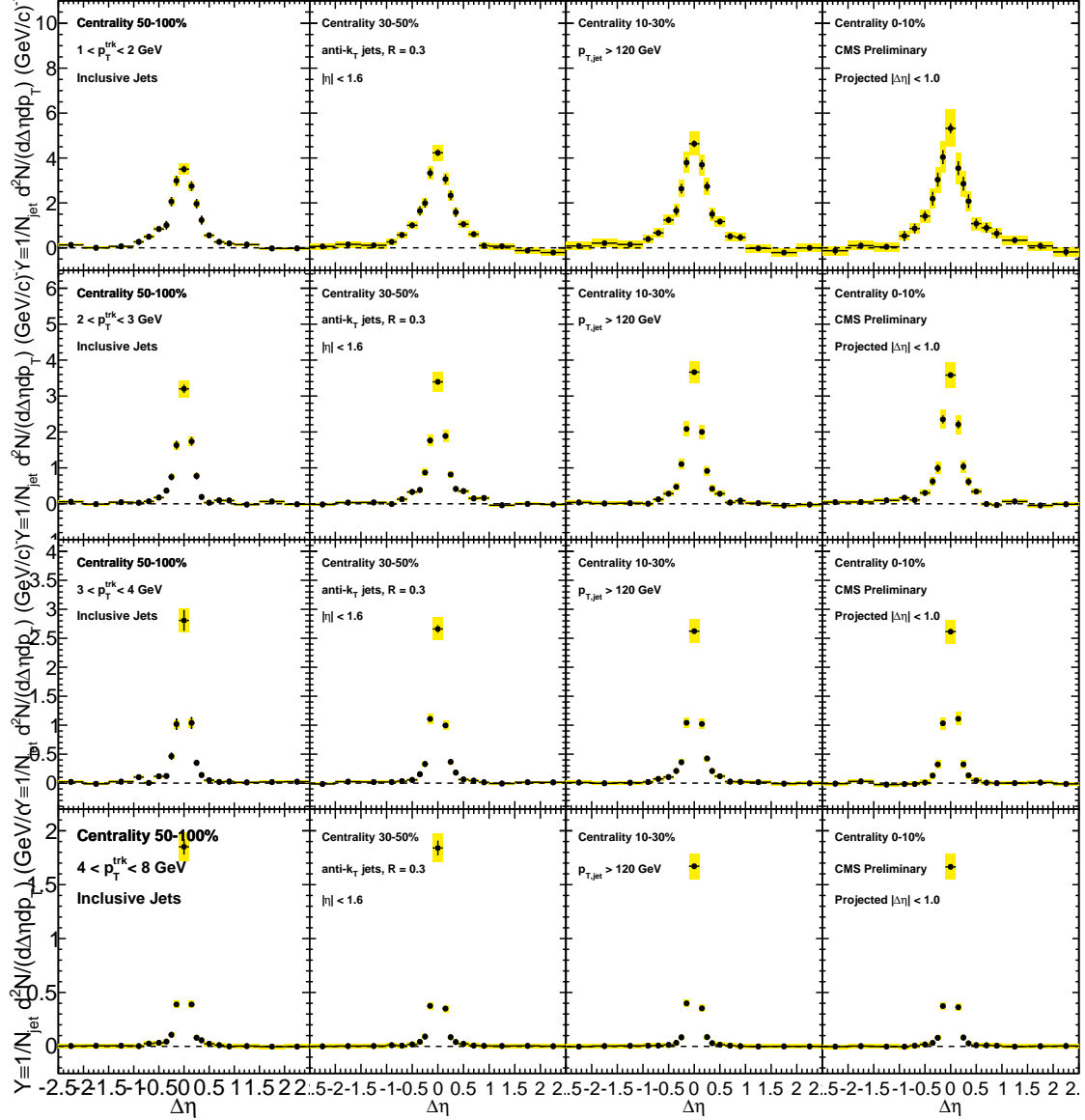


Figure 88. Inclusive jet correlated yield in  $\Delta\eta$ , shown to axis range  $|\Delta\eta| < 2.0$ . The deviation of the most peripheral points from zero is assigned as systematic uncertainty as discussed in the Systematic Uncertainty section above.

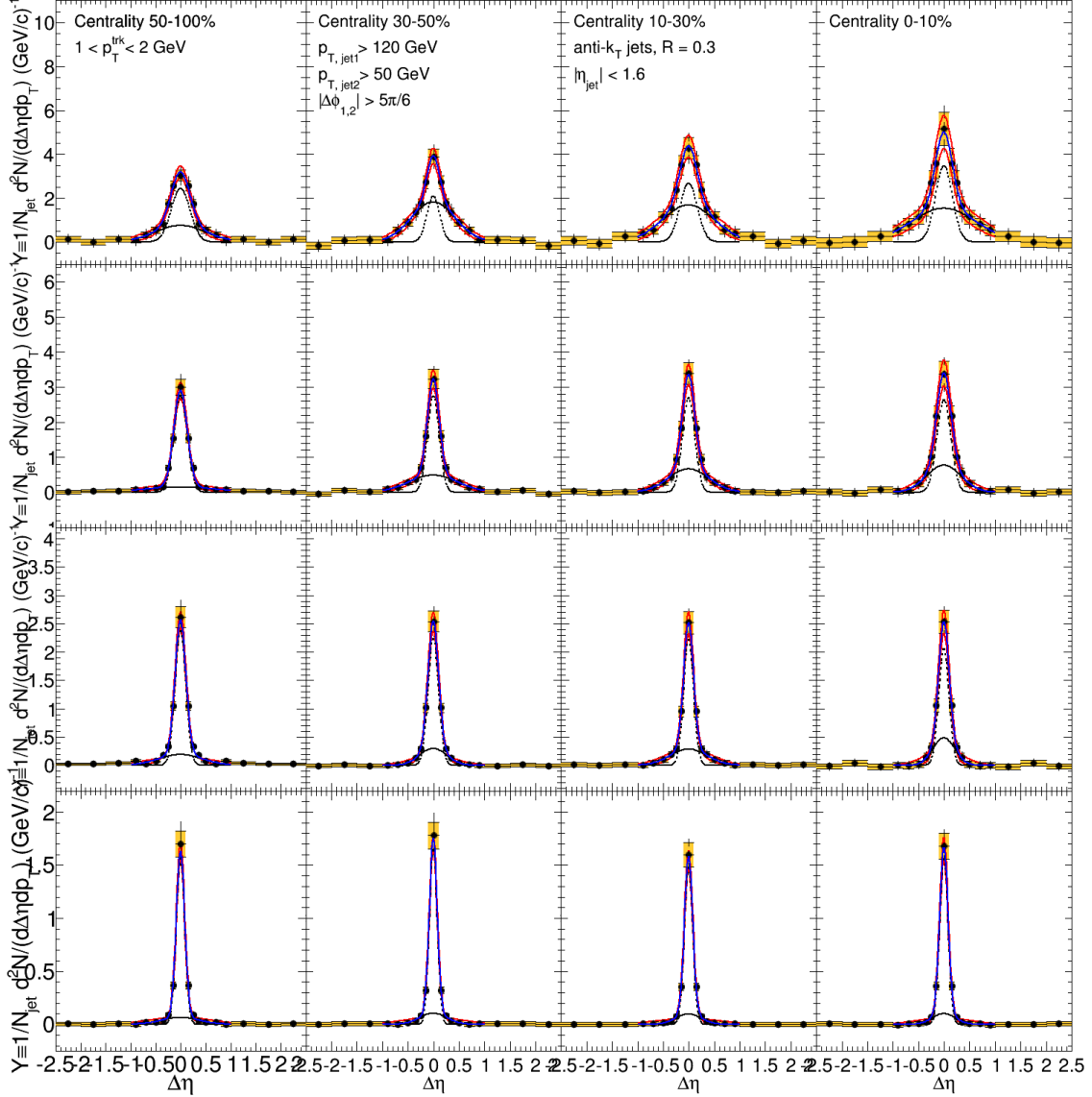


Figure 89. Illustration of the fits used to determine the distribution widths (shown here for leading jet PbPb  $\Delta\eta$  correlations). Correlations are fit to a double gaussian (shown in blue, with black dashed lines indicating constituent gaussians), and width is taken as the  $\Delta\eta$  value containing 67% of the total yield. Points are varied by their systematic errors and the fits are repeated (shown in red) to obtain the systematic error on the width.

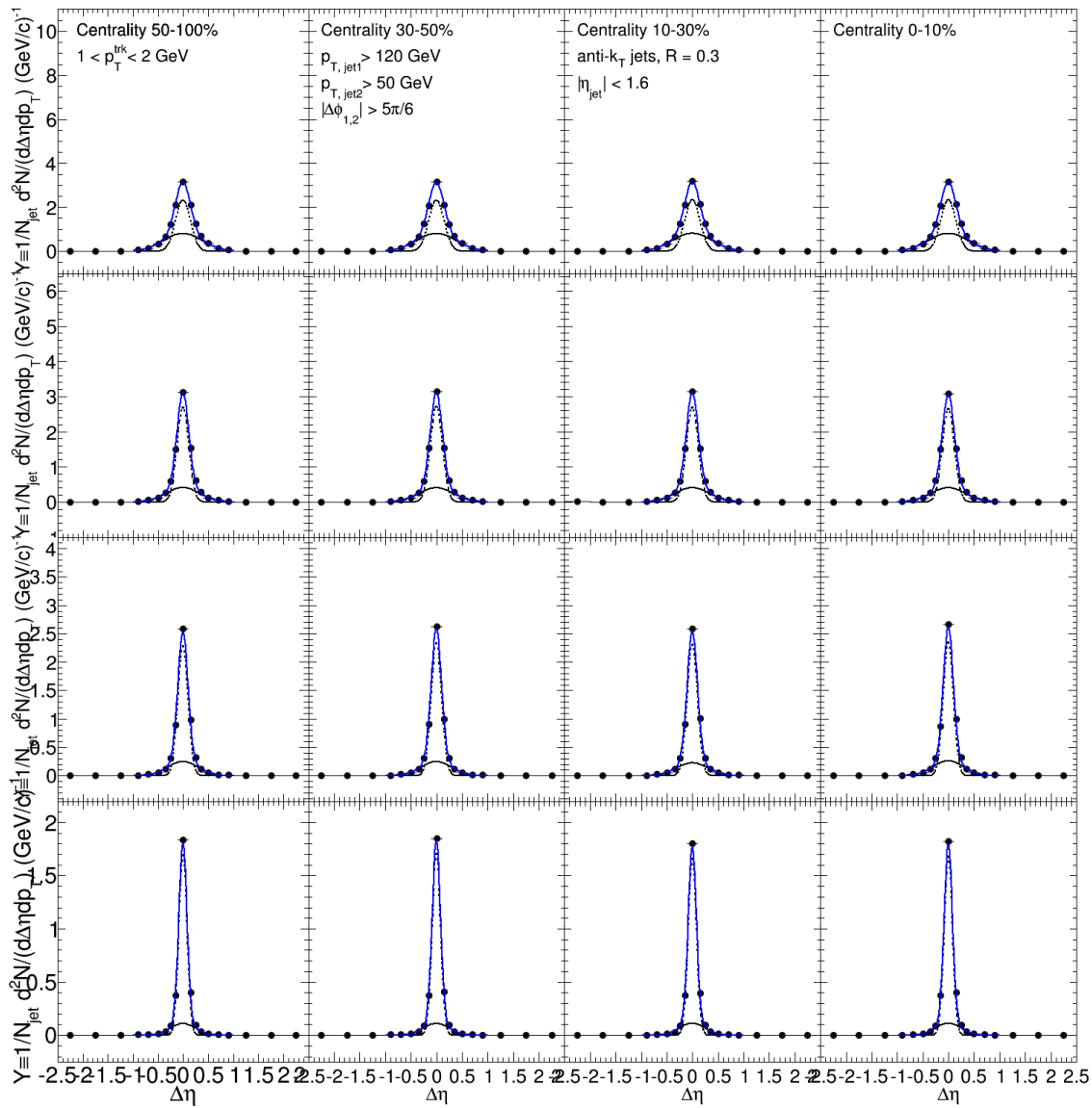


Figure 90. Illustration of the fits used to determine the distribution widths (shown here for leading jet pp  $\Delta\eta$  correlations). Correlations are fit to a double gaussian (shown in blue, with black dashed lines indicating constituent gaussians), and width is taken as the  $\Delta\eta$  value containing 67% of the total yield.

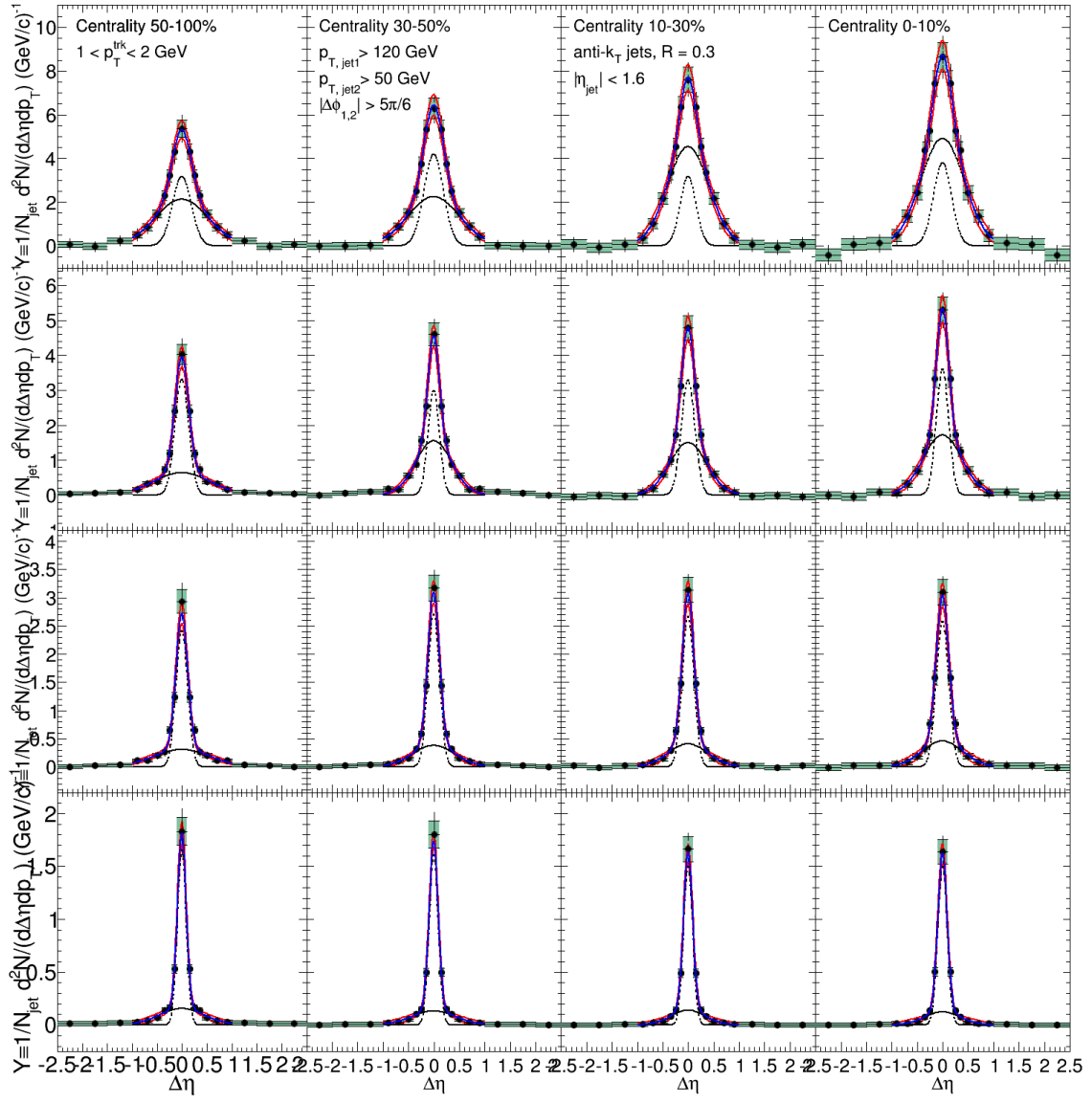


Figure 91. Illustration of the fits used to determine the distribution widths (shown here for sub-leading jet PbPb  $\Delta\eta$  correlations). Correlations are fit to a double gaussian (shown in blue, with black dashed lines indicating constituent gaussians), and width is taken as the  $\Delta\eta$  value containing 67% of the total yield. Points are varied by their systematic errors and the fits are repeated (shown in red) to obtain the systematic error on the width.

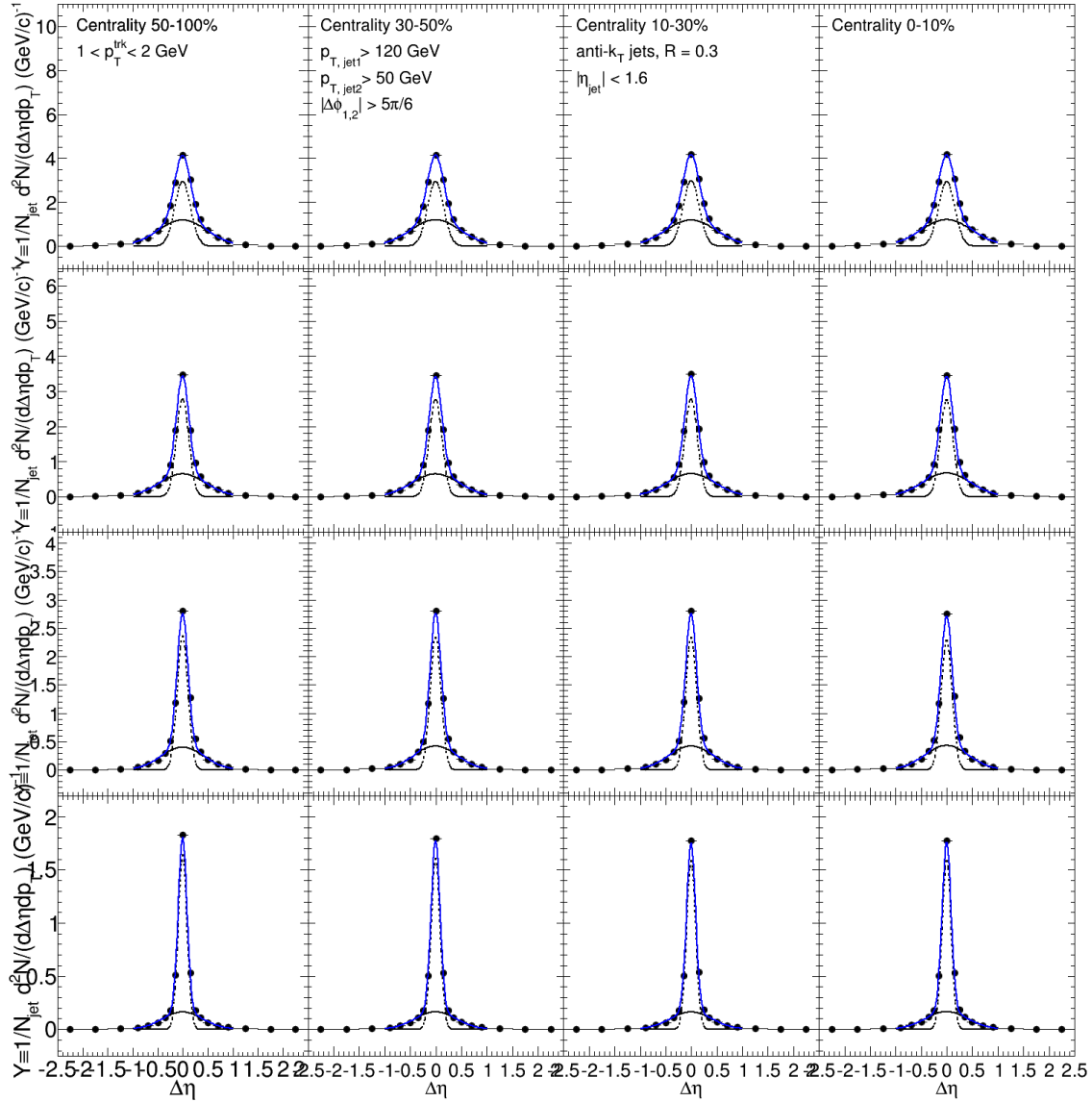


Figure 92. Illustration of the fits used to determine the distribution widths (shown here for sub-leading jet pp  $\Delta\eta$  correlations). Correlations are fit to a double gaussian (shown in blue, with black dashed lines indicating constituent gaussians), and width is taken as the  $\Delta\eta$  value containing 67% of the total yield.

**VITA**